FABRICATION AND CHARACTERIZATION OF SUB-MICRON AND NANOSCALE STRUCTURES IN COMMERCIAL POLYMERS

by

FATHIMA SHAIDA IBRAHIM

B.S., The Open University of Sri Lanka, 2003

AN ABSTRACT OF A DISSERTATION

submitted in partial fulfillment of the requirements for the degree

DOCTOR OF PHILOSOPHY

Department of Chemistry
College of Arts and Sciences

KANSAS STATE UNIVERSITY
Manhattan, Kansas

2010

Abstract

This dissertation describes the fabrication and characterization of nanoscale structures in commercially available polymers via multiphoton ablation and bottom-up self assembly techniques. High-resolution surface imaging techniques, such as atomic force microscopy (AFM) and chemical force microscopy (CFM) were used to characterize the physical features and chemical properties, respectively, of these nanoscale structures. Fabrication using both top-down and bottom-up methods affords flexibility in that top-down allows random, user-defined patterning whereas bottom-up self assembly produces truly nanoscale (1-100nm) uniform features. Multiphoton induced laser ablation, a top-down method, was used to produce random sub-micron scale features in films of poly(methylmethacrylate) (PMMA), polystyrene (PS), poly(butylmethacrylate) (PBMA) and poly[2-(3-thienyl)ethyloxy-4-butylsulfonate] (PTEBS). Features with 120-nm lateral resolution were obtained in a PMMA film which was concluded to be the best polymer for use with this method. It was also found that etching resolution was highest for polymers having high glass transition temperatures, low molecular weights and no visible absorption. Bottom-up self assembly of polystyrene-poly (methylmethacrylate) (PS-*b*-PMMA) diblock copolymer and UV/acetic acid treatment produced nanoscale cylindrical domains supported by a substrate. AFM imaging at the free surface showed metastable vertical PMMA domain orientation on gold substrates. In contrast, horizontal orientation was obtained on oxide-coated silicon regardless of surface roughness and annealing conditions. The horizontal domain orientation on silicon substrates was ideal to probe simultaneously the difference in surface charge and hydrophilicity of the two distinct nanoscale domains of UV/AcOH treated PS-*b*-PMMA films. CFM on UV/acetic acid etched PS-*b*-PMMA revealed the presence of –COO^- groups which were found to be more abundant inside the etched trenches than on the unetched PS matrix as shown by ferritin adsorption onto etched PS-*b*-PMMA. Lastly, the PS-*b*-PMMA was cast as a free-standing monolith at the end of a quartz micropipette. AFM revealed circular PMMA dots at the free surface, indicating alignment parallel to the long axis of capillary. Ion conductance within nanochannels indicated surface –charge governed ion transport at low KCl concentrations and flux of negatively-charged sulphorhodamine dye demonstrated the permselective nature of nanochannels.

FABRICATION AND CHARACTERIZATION OF SUB-MICRON AND NANOSCALE STRUCTURES IN COMMERCIAL POLYMERS

by

FATHIMA SHAIDA IBRAHIM

B.S., The Open University of Sri Lanka, 2003

A DISSERTATION

submitted in partial fulfillment of the requirements for the degree

DOCTOR OF PHILOSOPHY

Department of Chemistry
College of Arts and Sciences

KANSAS STATE UNIVERSITY
Manhattan, Kansas

2010

Approved by:

Major Professor
Dr. Takashi Ito

Copyright

FATHIMA SHAIDA IBRAHIM

2010

Abstract

This dissertation describes the fabrication and characterization of nanoscale structures in commercially available polymers via multiphoton ablation and bottom-up self assembly techniques. High-resolution surface imaging techniques, such as atomic force microscopy (AFM) and chemical force microscopy (CFM) were used to characterize the physical features and chemical properties, respectively, of these nanoscale structures. Fabrication using both top-down and bottom-up methods affords flexibility in that top-down allows random, user-defined patterning whereas bottom-up self assembly produces truly nanoscale (1-100nm) uniform features. Multiphoton induced laser ablation, a top-down method, was used to produce random sub-micron scale features in films of poly(methylmethacrylate) (PMMA), polystyrene (PS), poly(butylmethacrylate) (PBMA) and poly[2-(3-thienyl)ethyloxy-4-butylsulfonate] (PTEBS). Features with 120-nm lateral resolution were obtained in a PMMA film which was concluded to be the best polymer for use with this method. It was also found that etching resolution was highest for polymers having high glass transition temperatures, low molecular weights and no visible absorption. Bottom-up self assembly of polystyrene-poly (methylmethacrylate) (PS-*b*-PMMA) diblock copolymer and UV/acetic acid treatment produced nanoscale cylindrical domains supported by a substrate. AFM imaging at the free surface showed metastable vertical PMMA domain orientation on gold substrates. In contrast, horizontal orientation was obtained on oxide-coated silicon regardless of surface roughness and annealing conditions. The horizontal domain orientation on silicon substrates was ideal to probe simultaneously the difference in surface charge and hydrophilicity of the two distinct nanoscale domains of UV/AcOH treated PS-*b*-PMMA films. CFM on UV/acetic acid etched PS-*b*-PMMA revealed the presence of $-COO^-$ groups which were found to be more abundant inside the etched trenches than on the unetched PS matrix as shown by ferritin adsorption onto etched PS-*b*-PMMA. Lastly, the PS-*b*-PMMA was cast as a free-standing monolith at the end of a quartz micropipette. AFM revealed circular PMMA dots at the free surface, indicating alignment parallel to the long axis of capillary. Ion conductance within nanochannels indicated surface –charge governed ion transport at low KCl concentrations and flux of negatively-charged sulphorhodamine dye demonstrated the permselective nature of nanochannels.

Table of Contents

List of Figures ... ix
List of Tables ... xiv
Acknowledgements ... xv
Dedication ... xvi
Chapter 1 - Introduction ... 1
Objectives and Motivation ... 3
1.1 Top-down approach for the fabrication of sub-micron scale patterns in commercial homopolymers ... 4
1.2 Bottom-up approach for fabrication of nanoscale structures in commercial block copolymers ... 9
1.2.1 Block Copolymer (BCP) Self-Assembly ... 10
1.2.2 Properties of Block Copolymer thin films ... 11
1.2.3 Polystyrene-poly (methylmethacrylate)(PS-*b*-PMMA) diblock copolymer thin films 14
Chapter 2 - Review of Analytical Techniques used in the Characterization of Nanoscale Structures ... 18
Introduction ... 18
2.1 Contact Angle Goniometry ... 18
2.2 Atomic Force Microscopy ... 20
2.3 Chemical Force Microscopy ... 22
2.4 Conductance measurements ... 27
2.5 Fluorescence Emission Spectroscopy ... 30
Chapter 3 - Direct-Write Multiphoton Photolithography: A Systematic Study of the Etching Behaviors in Various Commercial Polymers ... 32
Introduction ... 32
3.1 Experimental ... 33
3.1.1 Chemicals and Materials ... 33
3.1.2 Preparation of Polymer Films ... 33
3.1.3 Direct-Write Multiphoton Photolithography ... 34

3.1.4 Pattern Transfer Using PDMS Soft Lithography 36
3.1.5 Atomic Force Microscopy Measurements 36
3.2 Results and Discussion 36
3.2.1 Pattern Formation via Direct-Write Multiphoton Photolithography 36
3.2.2 Power Dependence of the Etching Process 37
3.2.3 Comparison of Etching Behavior for Different Polymers 41
3.2.4 Edge Sharpness for Different Polymers 45
3.2.5 Pattern Transfer Using PDMS Soft Lithography 48
3.3 Summary and Conclusions 49
Chapter 4 - Bottom-up fabrication and characterization of nanoporous polystyrene-poly (methylmethacrylate) (PS-*b*-PMMA), diblock copolymer thin films 51
Introduction 51
4.1 Effects of substrate roughness on the orientation of cylindrical domains in thin films of a polystyrene-poly (methylmethacrylate) diblock copolymer 52
Introduction 52
4.1.1 Experimental 53
4.1.1.1. Chemicals and Materials 53
4.1.1.2. Substrate preparation 54
4.1.1.3. Preparation of PS-*b*-PMMA thin films 54
4.1.1.4. Characterization of substrates and PS-*b*-PMMA films 54
4.1.2 Results and Discussion 55
4.1.2.1. Surface roughness and cleanness of planar substrates 55
4.1.2.2. Effects of PS-*b*-PMMA film thickness on PMMA domain orientation 57
4.1.2.3. Effects of the annealing conditions on PMMA domain orientation in thin PS-b-PMMA films 60
4.1.3 Summary and Conclusions 62
4.2 Surface Chemical Properties of Nanoscale Domains on UV-Treated Polystyrene-Poly (methylmethacrylate) Diblock Copolymer Thin Films 63
Introduction 63
4.2.1 Experimental 64
4.2.1.1 Chemicals and Materials 64

4.2.1.2 Preparation of UV/AcOH-Treated PS-*b*-PMMA Films ... 65
4.2.1.3 Contact Angle Measurements ... 65
4.2.1.4 Chemical Force Microscopy Measurements ... 65
4.2.1.5. Observation of Ferritin Adsorbed on UV/AcOH-Treated PS-*b*-PMMA Films ... 66
4.2.2 Results and Discussion ... 67
4.2.2.1. Contact Angle Measurements ... 67
4.2.2.2 Chemical Force pH Titration ... 68
4.2.2.3 Friction Force Imaging of UV/AcOH-Treated PS-*b*-PMMA Surface Using Chemically Modified AFM Tips ... 72
4.2.2.4 Ferritin Adsorption onto UV/AcOH-Treated PS-*b*-PMMA Films Using TM-AFM 73
4.2.3 Summary and Conclusions ... 75
Chapter 5 - Bottom-up Fabrication and Characterization of a free-standing PS-*b*-PMMA monolith inside a quartz micropipette ... 77
Introduction ... 77
5.1 Experimental ... 79
5.1.1 Chemicals and Materials ... 79
5.1.2 Fabrication of PS-b-PMMA Monolith inside a quartz capillary ... 79
5.1.3 Characterization of capillary incorporated UV/acetic acid etched PS-*b*-PMMA monoliths ... 80
5.2 Results and Discussion ... 81
5.2.1 Fabrication of PS-*b*-PMMA Monolith ... 81
5.2.2 Characterization of UV/acetic acid etched PS-*b*-PMMA monolith ... 85
5.3 Summary and Conclusions ... 102
Chapter 6 - General Conclusions and Future Direction ... 103
References ... 106

List of Figures

Figure 1.1 Schematic of the nanoimprint lithography process (b) SEM micrograph of a perspective view of strips formed by nanoimprinting into a PMMA film, 70 nm wide, 200nm tall, surface roughness of <3 nm. Reprinted with permission from ref [15]. Copyright 1996, The American Association for the Advancement of Science. 6

Figure 1.2 (a) Topography and deflection mode AFM images of a 50 x 50 μm^2 etched area in a 160-nm thick PMMA film(top) line profile across the etched image (bottom). (b) Recessed disk microelectrode etched in a PMMA film. Reprinted with permission from ref [33]. Copyright 2006, American Institute of Physics (c) Polarization-dependent MPEFM images (20 μm x 20 μm) of a polymer/LC composite grating with a 5 μm spacing. Reprinted with permission from ref [43]. Copyright 2007, Wiley-VCH Verlag GmbH & Co. KGaA. 8

Figure 1.3 Chemical structure of PS-*b*-PMMA diblock copolymer. 12

Figure 1.4 Schematic of a PS-*b*-PMMA phase separated block copolymer film a) showing vertical PMMA domain orientation to an underlying substrate and after removal of the PMMA domains b) AFM image showing surface topography of a vertically oriented PS-*b*-PMMA film c) horizontal orientation of PMMA cylinders d) AFM image showing surface topography of horizontally oriented PMMA domains. 14

Figure 2.1 Graphical representation of contact angle between a liquid drop on a solid surface. γ_{SV} , $\gamma_{SL,}$ and γ_{LV} , the interfacial free energies of solid/vapor, solid/liquid and liquid/vapor interfaces. 19

Figure 2.2 Schematic diagram of the AFM showing the basic components. Reprinted with permission from ref [120]. Copyright 2010, Elsevier. 21

Figure 2.3 Chemically-functionalized AFM tip commonly employed in CFM, (R – COOH,-OH, $-NH_2$, $-CH_3$ etc). Reprinted with permission from ref [120]. Copyright 2010, Elsevier. 23

Figure 2.4 Schematic of a force-distance curve -(a) tip approaching surface (b) tip jumps into contact (c) tip indents into sample (d) tip breaks contact with the surface when the spring constant overcomes the adhesion force between tip and sample (e) tip moving away from the surface to its equilibrium position. Reprinted with permission from ref [120]. Copyright 2010, Elsevier. 24

Figure 2.5 Torsional deflection of the probe and cantilever during lateral scanning of the sample relative to the tip. 26

Figure 2.6 (a) Schematic of the electrochemical cell, b) Typical cyclic Voltammogram (*I-V* curve) obtained with an Ag/AgCl working electrode inside a micropipette filled with a 0.1M KCl solution vs. a reference Ag/AgCl electrode placed in the bulk KCl solution. 29

Figure 2.7 Schematic showing the electronic excitation and vibrational relaxation states of a molecule during fluorescence emission. 30

Figure 3.1 (a) Schematic of the sample scanning confocal microscope used for multiphoton photolithography (b) Chemical structures of commercial neat polymers used for multiphoton-induced etching. 35

Figure 3.2 (a) AFM topography image of patterns fabricated in a 120K PMMA thin film (~100 nm thick) using direct-write multiphoton photolithography. The average laser powers (in mW) used for polymer etching have been appended to the image. (b) Cross-sectional profile taken along the line shown in (a). 37

Figure 3.3 Laser power dependence of etch depth for two 15K PMMA films having different thicknesses (~120 nm, open circles, and ~450 nm, filled circles). Etch depth was measured from AFM cross-sectional profiles of 5 x 5 μm^2 square patterns fabricated at different laser powers. The dashed and solid lines show fits to the data using Eqn. 4. 39

Figure 3.4 Laser power dependence of etch depth for (a) 120K PMMA, (b) 120K PS, (c) PBMA and (d) PTEBS. Etch depth was measured from AFM cross-sectional profiles of 5 x 5 μm^2 square patterns fabricated at different laser powers. The solid lines show approximate fits to the data using Eq. 3-4 and the average *n* values given in Table 3.1. 43

Figure 3.5 UV-Vis spectra of (a) 15K PMMA (150 nm thick), (b) 15K PS (130 nm thick), (c) PBMA (300 nm thick) and (d) PTEBS (ca. 70 nm thick). 44

Figure 3.6 Cross-sectional profiles of gratings fabricated in (a) 15K PMMA, (b) 16K PS, (c) PBMA (d) PTEBS and (e) 10 x 10 μm^2 surface relief gratings fabricated in PMMA. 46

Figure 3.7 AFM topography images of patterns fabricated in (a) 15K PMMA and (b) PDMS. The latter was patterned via soft lithography using the 15K PMMA pattern. Cross-sectional profiles across the AFM images are also shown. 49

Figure 4.1 AFM images (500 x 500 nm^2) of the cleaned surfaces of (a) Au/Si, (b) Au/glass, (c) s-SiO_2/Si and (d) r-SiO_2/Si. A typical cross-sectional profile of each sample surface is also given. Copyright 2009 Elsevier. 56
Figure 4.2 AFM images (500 x 500 nm^2; Δz = 20 nm)) of PS-*b*-PMMA film surfaces having different thicknesses (t) on (a) Au/Si, (b) Au/glass, (c) s-SiO_2/Si and (d) r-SiO_2/Si. The ellipsometric thickness of each film is included in each image. Left: $t < L_0$; center: $t \approx L_0$; right: $t >> L_0$. All the PS-*b*-PMMA films were annealed at 160 °C for 60 hours in vacuum. Copyright 2009 Elsevier 58
Figure 4.3 AFM images (500 x 500 nm^2; Δz = 20 nm)) of the surface of PS-*b*-PMMA films on (a) Au/Si and (b) Au/glass annealed under different conditions. The ellipsometric thickness of each film, which was close to L_0, is included in each image. The PS-*b*-PMMA films were annealed in vacuum at 160 °C for 60 hours (left; the same images as those shown in Figure 4.2(a) and (b)), at 190 °C for 150 hours (center) and at 190 °C for 210 hours (right). Copyright 2009 Elsevier 61
Figure 4.4 Contact angle measured as a function of pH on UV/AcOH-treated PS-*b*-PMMA (filled circles) and PS homopolymer (open circles) films on an oxide-coated Si substrate (30 – 35 nm thick film before UV/AcOH treatment). The measurements were made in aqueous solutions containing 1.0 mM phosphate at room temperature. The plots and error bars indicate the average and standard deviation, respectively, measured on three separate substrates. 68
Figure 4.5 Typical AFM images (image size: 1 x 1 μm^2; total gray scale range: 5 nm; scan rate: 3.5 Hz), force-displacement curves and force histograms of adhesion forces obtained with a COOH-terminated gold tip on a UV/AcOH-treated PS-*b*-PMMA film at (a) pH 3.0, (b) 4.5, and (c) 10.3. Measured in aqueous solutions containing 1.0 mM phosphate at room temperature. 69
Figure 4.6 Typical pH dependence of adhesion force between a COOH-terminated gold tip and a UV/AcOH-treated PS-*b*-PMMA film. Measured in solutions containing 1 mM phosphate at room temperature. The plots and error bars indicate the average and standard deviation, respectively, of adhesion force from 128 force curves. 70
Figure 4.7 AFM image (image size: 1 x 1 μm^2 ; total grey scale range: 5 nm; scan rate: 3.5 Hz) and force histograms of adhesion forces obtained with a COOH-terminated gold tip on a

UV/AcOH-treated PS-*b*-PMMA film at pH 4.5. The histograms were obtained based on adhesion forces obtained on the positions indicated by the dots in the AFM image: PS ridges (red), etched PMMA trenches (blue) and domain boundaries (green). Measured in aqueous solutions containing 1.0 mM phosphate at room temperature. 71

Figure 4.8 Contact mode AFM topography and friction images (250 x 250 nm^2; scan rate: 3.5 Hz) of a UV/AcOH-treated PS-*b*-PMMA film obtained in *n*-dodecane (a) with a CH_3-terminated gold tip and (b) an OH-terminated gold tip. The brighter contrast indicates the higher region in the topography images (total gray scale range: 3 nm) and higher friction in the friction images (total gray scale range: 0.1 V). The applied force was 10 nN, and scan rate was 3.5 Hz. 73

Figure 4.9 (a) Typical TM-AFM topography image (500 x 500 nm^2, total gray scale range: 50 nm; scan rate: 2 Hz) of a UV/AcOH-treated PS-*b*-PMMA film upon deposition of ferritin molecules. A ferritin solution (1mg/ml) in a 1 mM phosphate buffer of pH 6.5 was cast on the film for 30 sec for the deposition of ferritin. After rinsing with water, the sample was dried and imaged using TM-AFM in air. (b) Schematic diagram of ferritin adsorption on the PS ridges. 75

Figure 5.1 (a) Schematic diagram of a quartz capillary pressed down vertically over a PS-*b*-PMMA film on a glass substrate and heated under vacuum at 230°C. The molten PS-*b*-PMMA wicks up the capillary to form a monolith at the narrow end. (b) Optical image of a 50 μm thick PS-*b*-PMMA monolith formed at the end of a quartz capillary (magnification 10x). 82

Figure 5.2 (a) Schematic diagram of a UV/acetic acid etched PS-*b*-PMMA nanoporous monolith at the end of a micropipette showing horizontally aligned channels (white regions) within a PS matrix (grey regions) (b) individual nanochannels showing –COO^- groups lining the inner channel wall. 85

Figure 5.3 Typical TM-AFM topography images in air (1000 x 1000 nm^2, total gray scale range: 30 nm (a)-(d) and 70 nm (e); scan rate: 2 Hz) of the surface of an unetched PS-*b*-PMMA monolith formed at the end of a 25µm channel drilled into a 1mm glass disc, (a) and (b) two different regions on the film (c) after UV/AcOH-etching of the PMMA domains of the film shown in (a) & (b). Figures (d) and (e) represent images taken on an unetched PS-*b*-PMMA

monolith cast on a different 1mm glass disc. The PMMA domains are seen as bright circular dots (a),(b),(d) & (e) (elevated) and as pitted regions after PMMA removal in (c). 87

Figure 5.4 (a) Schematic of the electrochemical cell used for the conductance measurements. (b) & (c) Typical cyclic voltammograms (scan rate 0.1 V/s) obtained for KCl-filled etched PS-*b*-PMMA monolith at different KCl concentrations (a) overlapped CVs for 10^{-5}, 5 x 10^{-5} and 10^{-4} M KCl (b) overlapped CVs for 10^{-3}, 10^{-2} and 10^{-1} M KCl measured against an Ag/AgCl reference electrode. 90

Figure 5.5 Typical log plot of conductance of a KCl filled quartz capillary (tip I.D- 75 µm) as a function of KCl concentration before (red circles) and after (black circles) incorporating the PS-*b*-PMMA monolith.. 91

Figure 5.6 Typical log plot of conductance vs. electrolyte concentration of a quartz capillary with a PS-*b*-PMMA monolith. The electrolyte used was KCl (black), LiCl (grey), tetramethyl ammonium chloride (green) and tetrabutyl ammonium chloride (blue). Conductance plot of KCl filled quartz capillary (tip I.D- 75 µm) with no monolith (red).................................... 95

Figure 5.7 Typical transport plots for sulphorhodamine B through a UV/acetic acid etched nanoporous PS-*b*-PMMA monolith as a function of time. The feed solution concentration of the dye was 100 µM dissolved in water (black) 1mM KCl (red) 10mM KCl (blue) and 100mM KCl (green), (a) & (b) represent transport data obtained from two different PS-*b*-PMMA monoliths. 100

List of Tables

Table 2.1 Common surface characterization techniques and their lateral resolutions................. 27

Table 3.1 Glass Transition Temperatures, n Values, and Edge Sharpness for the Polymers Examined. 42

Table 4.1 Surface Root-Mean-Square Roughness (R), Grain Diameter on the Surface (d_g) and Water Contact Angle (θ^{water}) of the Substrate Surfaces Used in this Study.......................... 57

Table 5.1 Height of water column and calculated water contact angle (θ^{water}) for plasma-treated and PS-coated cylindrical quartz capillaries. Values reported for the height are the average and standard deviation of at least three trials. 84

Table 5.2 Summary of the surface mobilities of cations within different PS-*b*-PMMA monoliths. The surface mobility reported is the average and standard deviation of surface mobilities calculated from the respective conductance plots of the cations at 10^{-5}, 5 x 10^{-5} and 10^{-4} M electrolyte concentration. 96

Table 5.3 Ratios of surface mobility of a cation to the surface mobility of tetrabutyl ammonium cation for different PS-*b*-PMMA monoliths. 97

Table 5.4 Diffusion Coefficient of sulphorhodamine B dye calculated using Eq-13 and the transport plots shown in figure 5.6 (a) –Monolith 1 and 5.6 (b)-Monolith 2. 101

Acknowledgements

I greatly appreciate the constant support and guidance of my supervisor, Dr.Takashi Ito, throughout my research career at KSU. I thank him for accepting me as his research student and teaching me all of the invaluable research skills. I cannot thank him enough for leading me in the right path to success.

I am glad to have had great people who created a friendly work atmosphere and with whom I have shared many memorable moments in and out of lab: Neluni Perera, my ex-roommate and best friend, whose support and friendship never ceased, Dr. Iwona Grabowska for her assistance with the AFM instrument, Dr. Helene Maire for sharing her research skills in polymer substrate preparation, Dr. Yongxin Li for sharing his research skills and being very helpful in the lab, Ms.Shinobu Ito for her assistance with the fabrication of free-standing monoliths and for the preliminary work she did on them, and Mr. Bipin Pandey, Mr. Feng Li and Mr. Khanh Hoa Tran Ba for being helpful and friendly lab mates. I would also like to thank Dr. Tom Everett and Dr. Jeff Lange for helping me with the confocal set up during my first project, for the many times they had to stop their work to help me find the "laser beam". I am also very grateful to Dr.Daniel.A Higgins for his ideas and suggestions for the work on multiphoton lithography. I would like to thank Jim Hodgson for making the quartz micropipettes, Ron Jackson, for making the electrochemical cells both of which were important to the work reported in chapter 5 and Tobe Eggers for his technical support with the computer systems.

I am very grateful to the members of my advisory committee: Dr. Daniel.A. Higgins, Dr. Kenneth J. Klabunde and Dr. Philine Wangemann for their suggestions on my Ph.D proposal and their valuable time and I also thank the chairperson Dr. Bruce Law for conducting the exam.

Financial support of this work from Terry C. Johnson Center for Basic Cancer Research for my summer stipend, US Department of Energy, ACS Petroleum Research and continued support from Kansas State University is greatly appreciated. I thank the PLU committee for recognizing me for the classroom (2007) and research awards (2009). I am very grateful to Ms. Earline Dikeman and Brenda Luther for ensuring a fulfilling teaching experience.

Last but not the least, am ever so grateful to my family and friends who encouraged and stood by me through good and difficult times and my husband for being very patient with me.

Dedication

This work is dedicated to my mum, dad, my husband and the rest of my family.

Chapter 1 - Introduction

The current trend in industry and fundamental research is towards miniaturization of components and devices, hence the constant quest by researchers for materials and methods that can team up for the fabrication of nanostructures typically in the range of 1-100 nm. It is in this size regime that atoms and molecules interact and assemble into structures that possess unique characteristics all dependent on the nanoscale size of the structures. Thus it is hardly surprising that nanostructured materials are extremely attractive, among other applications, as templates for the synthesis of other composite nanostructures. This is so because molecular interactions, processes and chemical and physical phenomena can be finely controlled, at the nanoscale, and directed to form the desired geometries of nano materials, such as nanoparticles and nanowires. The unique nano-dimension coupled with features such as large interior surface/volume ratio, high porosity with monodisperse pores, highly ordered structures, versatile, rich and tunable surface composition underline their important uses in various applications such as size and affinity based separations, catalysis, filtration, chemical sensor arrays, templates for synthesis of nanomaterials, bioseparations and electronic devices. Opportunities for novel uses are constantly being sought as research in nanotechnology continues to unravel new methods and materials that can be patterned into nanoscale structures.

Almost all routes to nanoscale structures have employed one of two types of patterning methods to create them, the top down and the bottom up approach. Various lithographic techniques encompass the top-down approach to nanometer-sized patterns and the bottom up method relies on the self assembly of macromolecules to create supramolecular assemblies of nanometer scale structures. Nanopatterns produced via the bottom up approach have often been used, among other applications, as templates for top-down nanostructuring. This process often involves the use of a self assembled polymer with nanoscale patterns that is used as a template to transfer patterns onto other materials via a top-down fabrication technique. Alternatively, UV light is irradiated on a patterned photomask placed over a self-assembled block copolymer film. The exposed regions cross-link while the unexposed regions are rinsed away leading to spatially controlled nanostructures that can be patterned into nanochannels. In addition, high-resolution nanoscale patterns, including nanoporous monoliths and patterned nanoparticles have been

produced by the integration of top-down and self assembly methods.[1, 2] For instance, hierarchical control of self-assembled nanopatterns with long-range order and tunable orientation can be produced within top down defined submicron patterns.[1] These are a few of the examples that demonstrate the versatility of the top-down and bottom-up approaches to precisely control the fabrication of structures from submicron to nanoscale dimensions.

Nanoscale structures have been fabricated in various materials depending on the type of application under consideration. For instance, electronic devices employ light sensitive (DNQ)-based and other photoresist materials consisting of a polymer and a photoacid generator for conventional photolithographic patterning of circuits.[3] The materials used for top-down lithographic techniques largely depended on the wavelength of the radiation source and required dopants and additives to optimize absorption of a particular wavelength. The next generation of top down methods using laser ablation lithography employed doped and neat homopolymers for ablation studies.[4] However, the majority of such studies employed doped polymers to enhance ablation rates when the laser illumination was outside the polymer's absorption spectrum. Studies involving laser ablation with neat polymers, such as poly (methylmethacrylate) (PMMA), typically focused on either ablation mechanisms or types of radiation source and materials that can be ablated. In the bottom-up approach to nanoscale structures, two major classes of materials are employed: forming nanoscale structures in inorganic materials, such as silica, using organic surfactant templates and the self-assembly of phase-separated block copolymers (BCPs). The latter is by large the best studied and documented class of materials. The wide use of polymers to fabricate nanostructures is justified in that it is easier to process polymeric materials, they are flexible and do not crack under stress and more importantly their natural length scale is limited to molecular dimensions so their morphologies in the bulk lie precisely at the nanometer length scale. Furthermore, neat polymers with inherent chromophores absorb light from UV to IR wavelengths and the ablation properties are reported for a few of them. These make them attractive for top-down laser ablation patterning. On the other hand, self-assembling BCPs possess a very narrow distribution of pore sizes and unique chemical functionalities that can be functionalized with various chemical moieties to tune chemical interactions at the nanopore interface. More importantly BCPs are very flexible in that they can be cast in any form, including thin film and monolithic conformations, to create large matrices with nanoscale pores/channels. Highly ordered nanoscale structures fabricated in polymers, via

top down and bottom up approaches, are continuing to replace conventional nanoporous media based on sol gels and entangled polymers/fibers in various applications.

Objectives and Motivation

This thesis describes the fabrication and more importantly the characterization of nanoscale patterns formed in commercially available homopolymers and polystyrene-poly(methylmethacrylate) (PS-*b*-PMMA) block copolymer via a top-down direct write laser ablation technique and the bottom-up self assembly, respectively. Practical applications, such as templating, catalysis and separation, require nanoscale structures formed in thin films with long range ordering of domains and in the case of BCPs vertical orientation of the microphase-separated domains to an underlying substrate. In addition to controlling the physical aspects of the nanoscale structures, characterizing their surface chemical properties, at the nanoscale resolution, is of equal importance in applications relying on interfacial phenomena. Research to date has largely focused on the physical aspects of the nanoscale structures and how well these can be adapted for a specific application. Currently, conventional materials such as polydisperse entangled polymers used in chromatographic columns and as filtration membranes are being replaced by well ordered nanoporous materials with uniform pore sizes. In view of the promising potential of ordered nanopatterned polymers, the overall objective of this project was to employ two different routes, top-down and bottom-up, to the fabrication of nanoscale structures in commercially available polymers, focusing on their characterization. The nanoscale structures were fabricated in thin films supported by substrates and finally in a free-standing conformation. Specific objectives of the project included the systematic study of commercial polymers best suited for nanoscale patterning via a top down approach, investigation of the optimum conditions required to orient nanoscale domains (PMMA), both vertically and horizontally, in thin films of PS-*b*-PMMA via the bottom-up self assembly and in-depth characterization of the surface chemical properties of UV modified PS-*b*-PMMA thin films and free-standing monoliths.

Control over nanodomain orientation in thin films of PS-*b*-PMMA was important in this work for subsequent chemical characterization of the films after UV/acetic acid etching of the minor phase (PMMA). Although vertical domain orientation of the nanoscale PMMA cylinders

is the preferred structure from a practical point of view, the horizontal domain orientation is crucial for characterization of the surface chemical properties of the etched domains as well as the unetched PS matrix, as will be described in the second section of chapter 4. Building upon this framework, a free standing nanoporous PS-*b*-PMMA monolith was fabricated inside a quartz capillary and characterized based on the transport properties of ions and molecules inside the nanochannels. The incorporation of a free-standing PS-*b*-PMMA monolith inside a capillary has never before been reported, as the majority of work on nanofabrication of patterns, including applications, was demonstrated on thin films supported by substrates. The work described in this thesis was largely motivated by the increasing importance nano-patterned materials are gaining for various applications like templates for synthesis of other nanomaterials (nanodots, nanowires etc), as separation membranes, catalyst supports and micro- nano- fluidic channels. The fabrication and characterization of the free-standing PS-*b*-PMMA monoliths was accomplished with a view to adapting such a system for potential chromatographic separation columns.

1.1 Top-down approach for the fabrication of sub-micron scale patterns in commercial homopolymers

A top-down approach for the fabrication of sub-micron to nanoscale structures involves reduction in size of larger structures to nanoscale patterns without any atomic level control. The most common top-down approach involves lithographic patterning techniques such as optical lithography including UV, deep UV and extreme UV, and X-rays.[5] Some of the unconventional lithographic techniques employ high energy particles such as electron and ion beams [6, 7] and electrically neutral metastable atoms[8, 9] to form high resolution patterns in appropriate resist films and planar substrates.[10] Pattern formation using scanning probes,[11, 12] soft[13] and nanoimprint lithography[14-16] have been shown to produce high resolution features that cannot be realized with conventional optical lithography which is largely limited by diffraction of light. The latter techniques, collectively known as micromachining, are a class of top-down fabrication routes for producing features in the 1-100 nm regime, in at least one of its dimensions.[10, 17]

Conventional optical projection lithography generally employs visible or UV light to expose a photoresist coated substrate by projecting an image of a pattern, through a photomask,

onto the photoresist film.[5, 10] The radiation alters the physical or chemical properties of the exposed areas of the photoresist, such as its solubility, so that the exposed areas become more soluble than the unexposed areas. In the development stage the soluble areas can be removed yielding a pattern of the photomask on the film. The spatial resolution obtained by this method is frequently limited by the chemical development step, the quality of the photomask employed and by diffraction of light from the mask. The resolution is governed by ($R = k\lambda/NA$) where λ is the wavelength of light used, NA ($n\sin\theta$) the numerical aperture and k a process dependent parameter between 0.4-1).[10] Therefore, high resolution of structures formed in the resist can be achieved by shorter wavelengths. Over the years feature sizes produced by optical lithography have shrunk to <250 nm with progressively shorter wavelengths. However, this required optimization of suitable photoresist, light source, optical lens system to deal with shorter wavelengths in the UV, deep UV and EUV (extreme ultra violet ~10nm) regions of the spectrum. For instance, DNQ-based photoresists can handle UV wavelengths of 365nm or 436nm but are not suitable for use at wavelengths ca.250 nm (deep-UV). Extensive research has been done in photoresist technology for use with UV, deep UV and much shorter wavelength sources for optical projection lithography.[5] Smaller features in the sub-micron and nanoscale regime can be formed using X-ray or electron beam lithographic techniques. In fact, sub-50 nm resolution features have been obtained using electron beam [7, 18] and x-ray lithography.[19, 20] However these techniques require specialized photoresists that are sensitive to each radiation source, optimized mask structures and sophisticated instrumentation. In contrast to optical lithography, two-photon induced photopolymerization in a liquid resin is capable of producing 3D structures at sub-diffraction limit resolution.[21-26] Two-photon induced photopolymerization involves irradiating a liquid resin with a high power pulsed laser source. Since the two-photon absorption rate depends quadratically on the incident light intensity, excitation is confined to a sub-micron focal volume. This means photopolymerization within the resin occurs only at this focal volume. Scanning this focal volume through the resin according to a predetermined pattern causes the resin to harden in the scanned regions. The unreacted liquid resin is removed to produce a 3D structure of the scanned region. Two-photon induced in-situ polymerization has been widely used to make arbitrary 3D structures with high spatial resolution, down to 120 nm in one study.[22] Photonic crystals [27] and micro devices [28, 29] have been fabricated using this technique. However, commercial positive-tone resists used for multiphoton-induced lithography

[24, 25] can be gradually exposed if used in the presence of light and subsequently may detach from substrates when immersed under liquids.[30]

Imprint lithography [16] and micromoulding in capillaries [31] have been used to fabricate nano- and micro- structures, respectively, in polymeric materials. Using imprint lithography, a minimum feature size of 25nm and a period of 70 nm have been fabricated in > 100 nm thick PMMA films.[15] This study employed a SiO_2 mold, with lateral feature sizes of 25nm formed by electron beam lithography. The patterned SiO_2 mold was pressed into a PMMA resist which creates a thickness contrast pattern in the resist. The resist in the compressed regions was removed via anisotropic etching to form the final features (see figure 1.1 (a) and (b)).

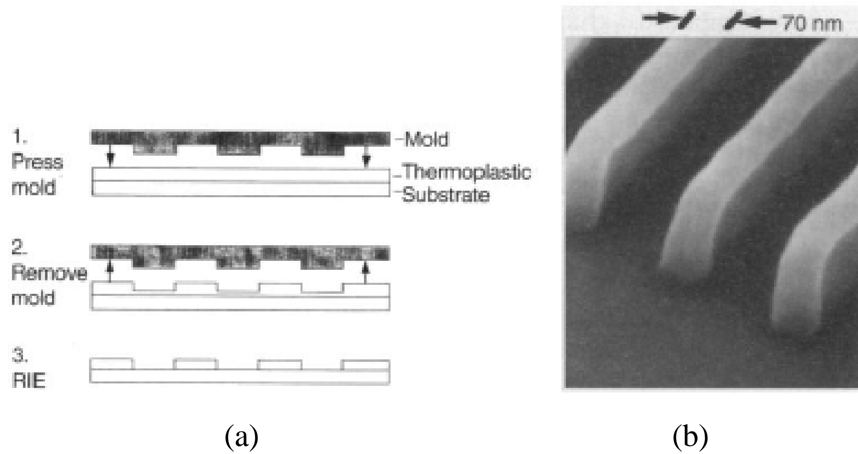

(a) (b)

Figure 1.1 Schematic of the nanoimprint lithography process (b) SEM micrograph of a perspective view of strips formed by nanoimprinting into a PMMA film, 70 nm wide, 200nm tall, surface roughness of <3 nm. Reprinted with permission from ref [15]. Copyright 1996, The American Association for the Advancement of Science.

The aforementioned methods depend on a secondary development step to realize the final patterns. Some of them even require additives in the resin to enhance multiphoton absorption and chemical development procedures to remove the unexposed regions. This can alter the resolution of patterns formed leading to feature broadening, or modify the surface chemical properties of the features.

Laser ablation is yet another technique employed to pattern materials on the micro scale dimension.[4, 32-34] Laser ablation of polymers dates way back to 1982 when it was first reported.[35, 36] It is the removal of material from the polymer surface using a high energy radiation source. Early studies typically focused on ablation rates and investigation of ablation products rather than fabricating nanoscale structures in polymer films.[37-42] Polymers based on both commercial pure polymers and those specially designed to maximize ablation rates and doped polymers were used in numerous laser ablation studies at shorter wavelengths.[37] Commercial polymers extensively studied include polyimide (PI), poly-methyl methacrylate (PMMA), polyethylenterephthalate (PET) and Teflon (PTFE) and were typically ablated at wavelengths < 350 nm.[37] Polymers whose ablation properties were less well studied include, but not limited to, polyethylene glycol, polyethylene, polycarbonates and conducting polymers such as poly-thiophenes, polypyrroles and poly-aniline.[37] Current studies are largely motivated by the range of materials that can be ablated at high efficiencies in order to pattern them on a micron and sub-micron scale for various functional devices. This also led to the use of various laser sources emitting from pulsed UV, visible to near-IR for use with commercial neat and doped polymers for ablation studies. In the vast majority of such studies, especially those performed with laser wavelengths outside the polymer absorption spectrum, dyes were added to the films to enhance absorption of the laser light and to assist ablation.[37, 40]

Ablative multiphoton etching using a tightly focused near-IR light from a mode-locked Ti:sapphire laser source at 870 nm was used by Higgins and Ito *et al* to fabricate sub micrometer-sized arbitrary patterns in thin films of neat poly-methyl methacrylate (PMMA) without the use of a photomask (see figure 1.1(a)).[33, 43] This method employed computer software which controlled scanning of the sample across the laser beam according to predetermined patterns fed into the computer. The non-linear nature of the multiphoton etching which resulted in high lateral resolution features in the PMMA film was demonstrated in these studies. This method was adopted by Higgins and Ito *et al* to fabricate functional devices in PMMA films, such as microdisk electrodes[33] and electrically switchable liquid-crystal based diffractive optics[43] (See figure 1.2). The distinct advantage of the ablative multiphoton direct-write method over previously reported methods is that it allows for resolution on the order of 120nm to be achieved without the use of any additives to assist ablation or subsequent chemical development steps to realize the final features.[33, 43] Although laser-based lithography had been

demonstrated previously in PMMA films, the structures produced were tens of micrometers in size and required thermal annealing to smooth out rough edges.[44] The direct-write technique is suitable for fabricating chemical sensor arrays, optical devices and micro- /nanofluidics devices,[45] since desired patterns can be generated, fed to the computer and "written" directly onto the polymer material without the use of photomasks or chemical developers. Films etched in this manner were shown to be stable under aqueous solution.[33] The use of this technique to etch submicron scale features, with high resolution, on commercial homopolymers is described in detail in chapter 3.

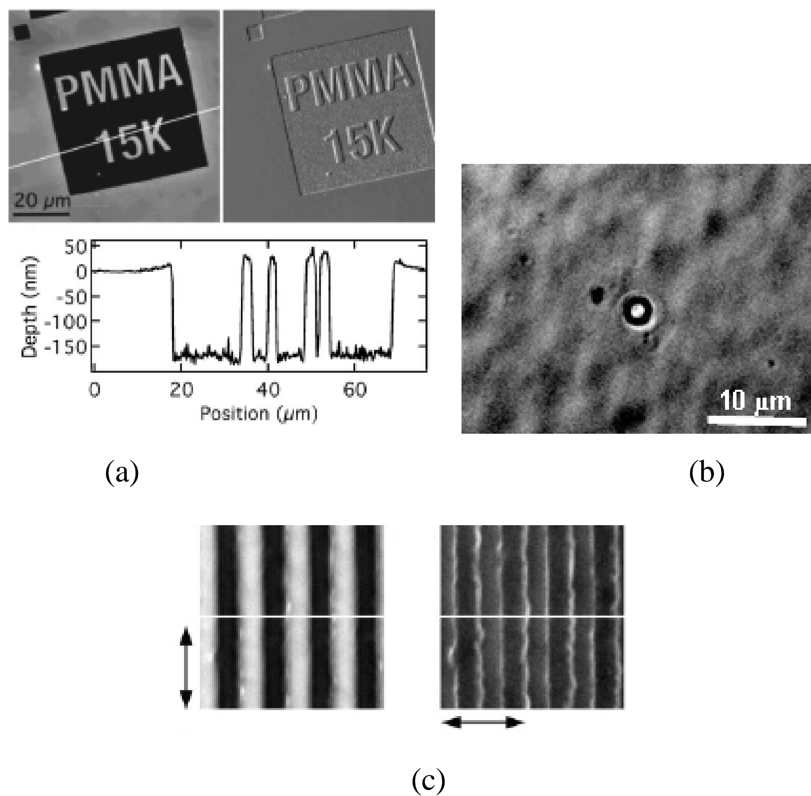

Figure 1.2 (a) Topography and deflection mode AFM images of a 50 x 50 μm^2 etched area in a 160-nm thick PMMA film(top) line profile across the etched image (bottom). (b) Recessed disk microelectrode etched in a PMMA film. Reprinted with permission from ref [33]. Copyright 2006, American Institute of Physics (c) Polarization-dependent MPEFM images (20 μm x 20 μm) of a polymer/LC composite grating with a 5 μm spacing. Reprinted with permission from ref [43]. Copyright 2007, Wiley-VCH Verlag GmbH & Co. KGaA.

1.2 Bottom-up approach for fabrication of nanoscale structures in commercial block copolymers

Bottom-up fabrication refers to building up or self assembly of a material from its constituents such as atoms or molecules, such as when polymers are formed from monomeric units or when polypeptides fold into functional proteins. Self-assembly is considered a radically different approach to fabrication of nanostructures that almost always falls within the dimensions defined by nanotechnology, which is 1-100 nm. Because the final structure obtained via self assembly is close to thermodynamic equilibrium and in its state of lowest free energy, they tend to reject defects.[46] Examples of structures fabricated via self assembly include self assembled monolayers (SAMs),[47] mesoporous materials with aggregates of surfactant as templates,[48-50] phase separated block copolymers (BCPs)[51-53] and aggregated meso-scale objects.[54] These examples illustrate the capability of self-assembly as a strategy for fabrication of nanoscale structures.

Among the systems that can self assemble into nanostructures, surfactant-templated mesoporous materials and the self assembly of phase separated block copolymers (BCPs) have gained enormous interest among researchers. As such, a brief description will be devoted to the surfactant-templated route to form nanostructures followed by a thorough discussion on the self assembly of block copolymers that form nanoscale domains. The latter method is the foundation of the work described herein.

Surfactant-templated mesoporous structures rely on the self assembly of surfactant molecules at a solid-liquid interface which can form nanoscale tubular structures. The so formed tubular templates can be used for the templated polymerization/calcination of silica [48, 49, 55] or aluminosilicates[50] between the ordered surfactant micelles. The long range ordering of the surfactant molecules leads to arrays of channels with nano dimensions in the silica film. Furthermore, the porous structure can be formed in a wide range of morphologies though with a larger distribution of pore sizes. Mesoporous inorganic materials formed using this methodology find potential applications in catalysis,[56] separation,[57] chemical/biological sensor arrays,[58] templates for nanowire synthesis[59] and optoelectronic devices.[60] However, BCP precursors by far are easier to process and require fewer steps for the fabrication of well ordered nanostructures.

1.2.1 Block Copolymer (BCP) Self-Assembly

BCPs are a class of materials that phase separate, due to the chemical incompatibility of the monomeric segments, into nanodomains within the bulk segment. Generating porous membranes from block copolymers goes back in time to the 1980s when it was first demonstrated by Lee *at al*. in 1988 using a triblock copolymer.[61] They showed the formation of a lamellar morphology of poly (4-vinylphenyl-dimethyl-2-propoxysilane)-b-polyisoprene-b-poly (4-vinylphenyl-dimethyl-2-propoxysilane) (PPS-PI-PPS) triblock copolymer film. The porous structure was generated after degrading the minor PI component via ozonolysis/methanol. They employed the same tri block copolymer to form porous structures with different morphologies as verified by SEM and TEM imaging.[62] The presence of residual functional groups was indicated by these authors with a potential for functionalizing these groups. The pioneering work done by Lee *at al* fuelled research in the area of block copolymer precursors for the generation of nanoporous structures.[63-68] The potential to use nanoporous films derived from block copolymers as lithographic templates was first demonstrated by Mansky *et al* when they succeeded in orienting the cylindrical domains perpendicular to the underlying substrate.[65] This orientation is crucial for templating applications. Thin films of polystyrene-polybutadiene (PS-PBD) with vertically oriented PBD domains were prepared and the PBD component degraded via ozonolysis to generate a well-ordered porous template. Ever since then researchers began harnessing the patterns produced by the self-assembly of block copolymer systems as lithographic templates.[69-72] Driven by this promising application and possible new ones, a vast amount of research has been devoted to studying the self assembly of block copolymers in terms of its chemistry and thermodynamics. In view of this, it is not surprising that BCPs fall into the category of nanomaterials that are well-explored and documented.[1, 2, 73-75] The majority of such work was driven by the potential applications of block copolymer templates as chemical sensors,[76] heterogeneous catalysis,[77] separation membranes,[78-80] and lithographic templates for the synthesis of nanomaterials of desired size and shapes.[81-83] The rest of this section will describe what makes BCP precursors unique, yet simple and well-suited to generate nanoscale porous structures. Following the general description of BCP systems, background research on the well-studied polystyrene-poly (methylmethacrylate)(PS-*b*-PMMA) diblock copolymer system will be described in terms of its fabrication, characterization of physical aspects and

applications. This will serve to justify the extensive investigation of the PS-PMMA system for the bottom-up fabrication of nanoscale domains in thin films and free-standing monolith with characterization of UV treated nanoporous PS-*b*-PMMA being the core focus.

1.2.2 Properties of Block Copolymer thin films

Block copolymers are polymers with two or more chemically distinct polymer fragments connected together in a long chain (figure 1.3). Owing to chemical and physical incompatibility these polymer segments are often immiscible and thus phase separate into domains rich in one phase within the bulk rich in the other phase. The resulting morphology depends largely on the relative volume fraction of each component. For instance, if the volume fraction of the minor segment is 0.3, it can phase separate into cylindrical domains within the major segment (see figure 1.4) in thin films. Some of the more commonly seen morphologies for diblock copolymers are vertical cylinders (figure 1.4(a) & (b)), lamellae (figure 1.4 (c) & (d)) and spheres. Triblock copolymers, with three chemically distinct polymer fragments, introduce additional building blocks hence more complex morphologies. The uniform domain size of BCPs is basically determined by the total molecular weight of the polymer and is continuously tunable from a few to several hundred nanometers by simply using polymers with different molecular weights. The uniform domain size is a signature of block copolymer materials. The phase separation behavior of BCPs is different in bulk/melt state from that in thin films of the polymer. Thin films of BCPs can be easily fabricated by spin casting from solutions of the polymer onto different substrates, commonly gold or silicon substrates. The thickness of such films can be easily controlled by the spin speed and/or polymer solution concentration. The orientation of nanodomains (parallel or perpendicular to an underlying substrate) in thin films is largely governed by the wetting properties of each chemically distinct segment of the BCP at the polymer/substrate and polymer/free surface interfaces. Interfaces have the strongest influence when the thickness of the BCP film is comparable to the microdomain spacing (ca.10-50 nm thick). Preferential wetting of one fragment in a BCP at an interface leads to horizontal domain orientation, such as when PMMA is cast on a silicon wafer in a PS-PMMA block copolymer preferential wetting of PMMA results in horizontal domain alignment at the polymer-free surface interface (figure

1.4(c)). This is because PMMA is more hydrophilic than PS hence preferentially wets the oxidized silicon surface. Films much thinner than the domain spacing often exhibit very little or no microdomains since all polymeric material is used to wet the interfaces. The microdomain orientation governed by the interfaces is thus not typically desirable for templating and most other applications. Various methods have been employed to control the orientation of the microdomains in thin films of BCP so that domains orient themselves perpendicular to an underlying substrate. Indeed the arrangement of microdomains in this manner makes more sense for nanolithographic and separation applications as opposed to horizontal orientation of domains. One of the common approaches adopted is the chemical tailoring of substrates, via self-assembled monolayers or random copolymer brush layers, to neutralize the surface in order to balance the affinities of both BCP fragments at the BCP-substrate interface.[84-86] In the absence of preferential wetting, domains orient vertically to the underlying substrate. Vertical orientation control is also achieved via non-chemical means such as optimizing film thickness[87] so that interfacial effects are minimal, control of solvent-evaporation conditions,[88] addition of homopolymers,[89] use of rough substrates[90] and electric field application during annealing.[91] The methods to control domain orientation to suit a particular practical application are numerous and a discipline in its own right.

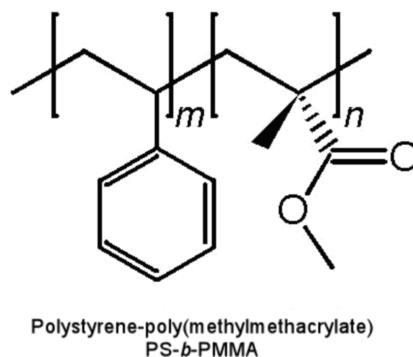

Figure 1.3 Chemical structure of PS-*b*-PMMA diblock copolymer.

Microphase separation into domains of the minor segment within the matrix of the major segment and its subsequent orientation although thermodynamically favored, is not a spontaneous process that occurs at room temperature. To overcome the kinetic barrier and to

form cylindrical domains, BCP films are usually annealed at high temperatures, above the glass transition temperature of the BCP, under an inert atmosphere. In order for self-assembled BCPs to find uses in functional devices or as lithographic templates, the minor phase that forms the microdomains has to be removed from the major phase that forms the matrix. This elimination results in an array of nanopores with uniform dimensions of a few to tens of nanometers. This is the functional form of the self-assembled BCP that finds uses in various applications. Removal of the minor phase is usually executed via chemical etching, UV irradiation or thermal treatment depending on the BCP system under study. The choice of the matrix or the major phase that is left over after removal of the minor component is crucial since it has to be mechanically stable to support the resulting porous structure. A weak matrix may collapse when the nanopores are formed. The majority of BCP systems require a wet chemical etching process to degrade the minor phase usually via hydrolysis.[92-96] Regardless of the method used for removing the minor phase, the surface chemistry of the nanoporous walls is distinctly modified after the etching process. The type of functional groups lining the inner walls of the nanoporous domains depends on the BCP system and the etching process. In polystyrene-polydimethylacrylamide-polylactide (PS-PDMA-PLA) triblock copolymer the PLA cylinders were selectively etched followed by hydrolysis of the PDMA brush lining the nanopores.[93] The hydrolysis introduced carboxylic groups on the pore surface which were then functionalized with different chemical groups to yield functionalized nanoporous materials.[93] The unique functionalities introduced during the etching process is crucial for applications that rely on chemical interactions with the pore surface such as specific/non specific adsorption in affinity based separations, interfacial chemical processes for catalysis, and selective transport of ions. The ability to functionalize the inner pore surface is a unique feature of block copolymer nanoporous materials which their inorganic counterparts (e.g. zeolites) donot possess inherently.

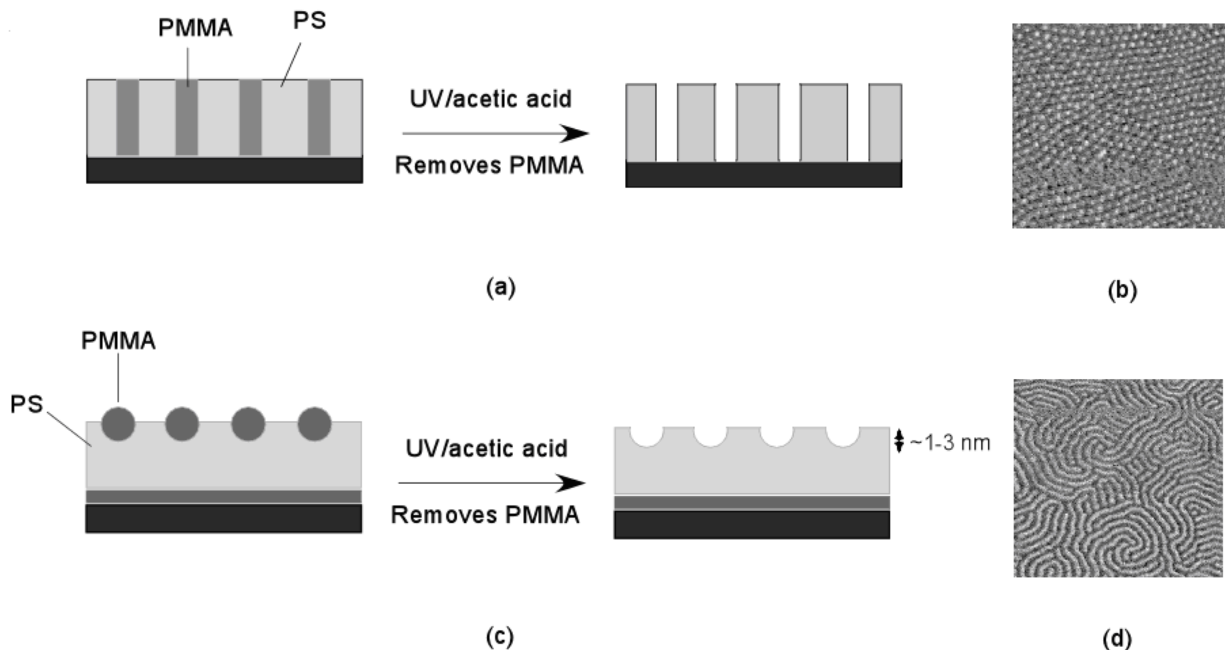

Figure 1.4 Schematic of a PS-*b*-PMMA phase separated block copolymer film a) showing vertical PMMA domain orientation to an underlying substrate and after removal of the PMMA domains b) AFM image showing surface topography of a vertically oriented PS-*b*-PMMA film c) horizontal orientation of PMMA cylinders d) AFM image showing surface topography of horizontally oriented PMMA domains.

1.2.3 Polystyrene-poly (methylmethacrylate)(PS-b-PMMA) diblock copolymer thin films

Background

Among block copolymer systems, PS-*b*-PMMA has been widely used to fabricate nanostructured materials[78, 79, 81-83, 97-99] because these materials can be fabricated using well-established procedures for selectively etching the PMMA domains.[71] The self-assembly of cylinder forming PS-*b*-PMMA, where the PMMA domains were oriented perpendicular to an underlying substrate, was first demonstrated by Thurn-Albrecht *et al* in 2000.[71] In these systems, PMMA usually forms the minor phase if its volume fraction is 0.3 compared to PS. They

demonstrated that nanopores were easily formed via exposure of the PS-*b*-PMMA thin films to UV radiation at 254 nm and subsequent acetic acid treatment to rinse away the degraded PMMA debris. This treatment transformed the PS-*b*-PMMA BCP into a nanoporous template with arrays of vertically aligned void cylinders. PS-PMMA is the only block copolymer system that requires UV radiation to form the nanoporous structure. Furthermore, degradation of PMMA and crosslinking of the PS occur in a single exposure step making the resulting PS matrix mechanically and chemically stable. Most other BCPs require heat treatment coupled with hydrolysis with strong acids or bases to generate the nanoporous system. Other cylinder forming block copolymer systems, such as polystyrene-polylactide (PS-PLA), polystyrene-polydimethylacrylamide-polylactide (PS-PDMA-PLA) and polystyrene-polyimide-polylactide (PS-PI-PLA) where the polylactide (PLA) forms the etchable domain, require hydrolysis for domain etching. The resulting PS matrix was not however cross-linked in these studies as in the case of UV/acetic acid etched PS-*b*-PMMA block copolymer films. Not cross-linking the PS matrix might make the nanoporous structure thermally unstable at elevated temperatures.[100] In addition to demonstrating the vertical alignment of cylinder forming PS-*b*-PMMA, Thurn-Albrecht *et al* also showed the use of vertically-aligned PS-*b*-PMMA as a nanoporous template for the fabrication of cobalt nanowires.[97] The nanowires grown within the templates had dimensions of the void cylindrical domains in the template: length of 500 nm and diameter of 14 nm.[97] Kim *et al*. from the same group also showed that silicon dioxide pillars, having a height of 6 nm and a diameter of 20 nm could be grown inside thin nanoporous PS-*b*-PMMA templates.[101] Guarini *et al*. demonstrated the deposition of gold nanodot arrays onto a nanoporous PS-*b*-PMMA block copolymer template.[87] Truly nanoscale materials (1-100nm) were synthesized using PS-PMMA block copolymer technology. These pioneering studies with PS-*b*-PMMA system spurred interest in research to explore new potential for nanoporous PS-*b*-PMMA block copolymer thin films other than its use as nanolithographic templates. Motivated by the effectiveness of the PS-*b*-PMMA nanoporous system current research has largely focused on two areas: a) demonstrations of the utility and versatility of nanoporous PS-*b*-PMMA b) optimizing orientation and domain sizes of the nanoscale cylinders in thin films. Optimization studies encompassed the influence of film thickness and PS-*b*-PMMA molecular weight on domain orientation and pore size distribution, respectively. Independent studies conducted by Xu *et al* [102]and Guarini *et al* [103] shed light on the optimum conditions of film thickness and molecular

weight that resulted in nicely ordered PMMA nanodomains in thin films of PS-*b*-PMMA. They also demonstrated that thicker films and larger molecular weights required the use of an electric field for long range vertical domain alignment. Another study conducted by Jeong *et al*. involved the use of a PMMA homopolymer to tune the pore sizes to values much lower than that dictated by the molecular weight of the pure PS-*b*-PMMA films.[104] Progress was also shown in the direction of reducing the number of steps involved in generating the nanoscale structures in PS-*b*-PMMA films. Xu *et al* described a procedure whereby vertically oriented PS-*b*-PMMA films were treated with acetic acid/water mixture without first exposing it to UV radiation according previous protocol.[105] Pores are generated within the PS matrix via selective dissolution of the PMMA domains drawn to the surface. Via TEM imaging they showed that the pores extended deep into the film. Another study reported by Asakawa *et al*. employed dry etching techniques, such as reactive ion etching, to etch out the minor PMMA domains to generate the nanoporous structure.[106] Given the numerous alternative strategies developed for generating nanoscale structures from the same precursor PS-*b*-PMMA block copolymer, it is to be expected that characterization largely focused on how well the domains were oriented or to assess the extent of removal of the minor phase. There is a scarcity of research devoted to the in-depth chemical characterization of the surface of the PS matrix after removal of the PMMA domains. Indeed, UV exposed PS-*b*-PMMA nanoporous films are chemically different from non exposed films because UV irradiation chemically modifies the surface resulting in a high surface free energy. This is largely due to the introduction of oxygen containing groups upon UV irradiation. Chemical characterization was done using macroscopic techniques such as IR or XPS that identified chemical groups introduced post etching.[93, 107] Even less is known about the chemical groups introduced in PS-*b*-PMMA systems after UV/Argon irradiation. The surface chemical properties of the inner walls of the cylindrical nanopores formed in UV treated PS-*b*-PMMA thin films was characterized via cyclic voltammetry (CV) and IR in previous projects conducted by the *Ito* group.[76, 79, 108] In these studies, the cylindrical PMMA domains in a thin PS-*b*-PMMA film were aligned vertically to an underlying gold electrode under optimized annealing conditions,[109] and etched via the well-established UV/AcOH treatment.[110] CV on a polymer-coated electrode measures redox-active molecules that penetrate through the nanopores to an underlying electrode.[111, 112]. The presence of -COOH groups lining the pore walls was shown, which could not be detected using infrared spectroscopy,[82, 108] through pH-dependent CV

measurements of charged and uncharged redox molecules.[108] In addition, the control of the charge[76] and protein adsorptivity[79] of the nanopore surface via 1-ethyl-3-(3-dimethylaminopropyl)carbodiimide-mediated amidation of the surface -COOH groups was also demonstrated. However, CV cannot be used to assess the surface chemistry of the unetched PS matrix since characterization was limited to probing the functional groups inside the cylindrical pores. Nevertheless, the surface properties of both the domains may need to be controlled for efficient templating and chemical separation applications using the PS-*b*-PMMA system. Therefore, investigating the surface chemical properties, on the nanoscale resolution, of the etched domains and the remaining PS matrix was one of the prime objectives of this project.

Chapter 2 - Review of Analytical Techniques used in the Characterization of Nanoscale Structures

Introduction

In this chapter, the main analytical techniques used for characterization of the structures produced in polymer films are discussed. A general description of the technique, along with its theoretical concepts, is given followed by their relevance to the work described in this thesis. Surface imaging using Atomic Force Microscopy (AFM) was extensively used throughout the research for topographic studies of the nanoscale structures produced by both top down (via multiphoton lithography) and bottom up (via self assembly of block copolymers) approaches. The top down fabrication of nano structures relied entirely upon AFM for in depth characterization of the structures formed in the polymers. While AFM using unmodified tips gave contrast in images due to purely topographic effects, AFM involving chemically modified tips, termed Chemical Force Microscopy (CFM), shed light on the surface chemical composition of ultra violet (UV)/acetic acid etched PS-*b*-PMMA films. Contact angle goniometry was another complementary analytical tool used for rapid characterization of surface chemical properties after various modifications to underlying substrates and polymer films. Finally, to characterize the transport properties of PS-*b*-PMMA monolithic structures, techniques based on cyclic voltammetry and fluorescence spectroscopy were used to measure ionic conductance and flux respectively.

2.1 Contact Angle Goniometry

Contact angle goniometry is a technique that allows the measurement of the angle formed by a drop of liquid at the point where the solid, liquid and vapor phases intersect (Figure 2.1). According to Young's equation, which defines the balance of forces caused by a drop of liquid on a solid surface, the contact angle (θ) is a function of the interfacial energies of the three phases[113] :

$$\cos\theta = (\gamma_{SV} - \gamma_{SL}) / \gamma_{LV} \qquad \text{Eq. 2-1}$$

where γ_{SV}, γ_{SL}, and γ_{LV} are the interfacial free energies between the solid and the vapor, the solid and the liquid, and the liquid and vapor, respectively. Contact angle measurements analyze the outermost 0.5 nm of a material[114]. This means that information about the interfacial surface free energy of a solid/liquid interface, hence its wetting properties, can be assessed by measuring the contact angle formed by a liquid in contact with the solid surface.

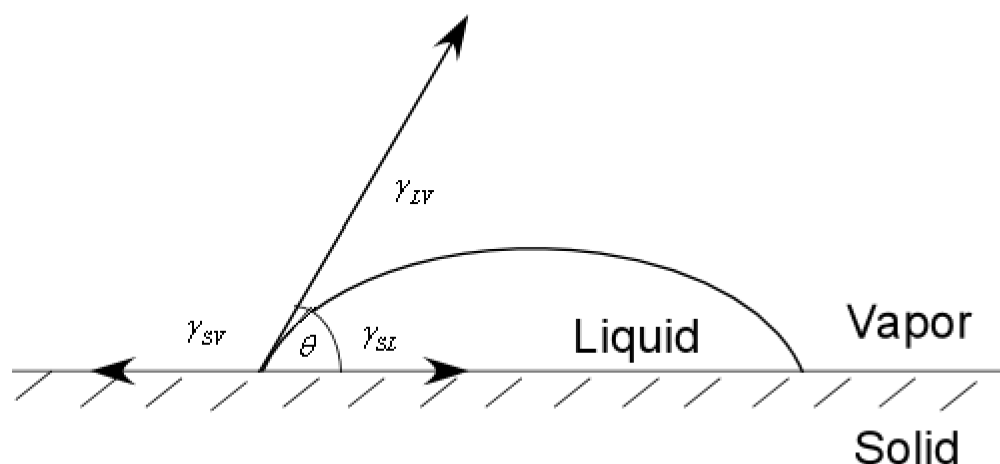

Figure 2.1 Graphical representation of contact angle between a liquid drop on a solid surface. γ_{SV}, γ_{SL}, and γ_{LV} , the interfacial free energies of solid/vapor, solid/liquid and liquid/vapor interfaces.

The wetting property of a solid is determined by a balance of the adhesion and cohesion forces which determine the interfacial surface energies[113, 115]. For instance, the molecules within the liquid bulk are attracted equally from all directions, but those at the liquid/vapor interface experience unequal forces and are pulled toward the center of the liquid. The net attractive force between the liquid molecules, known as the cohesive force, causes the liquid drop to maintain the smallest possible exposed area because it is thermodynamically more stable. If adhesive forces between the molecules of the liquid and solid overcome the cohesive forces, the liquid drop spreads out on the solid to assume a thermodynamically stable state with lower energy. In

this case according to Eq.2-1 , γ_{SL} solid/liquid is very small compared to the interfacial energies between solid/vapor and liquid/vapor and θ is small. On the other hand if cohesive forces are large compared to the adhesive force molecules of the liquid tend to keep to themselves and assume the shape of a sphere with large θ values. A highly polar surface possesses a large surface free energy which can overcome the cohesive forces of a liquid and cause it to spread out. In contrast low surface energy substrates cannot overcome this force and display poor wetting properties. In general if $\theta < 90^o$ the surface is sufficiently polar or hydrophilic and is wet by the probing liquid and if $\theta > 90^o$ the surface is hydrophobic (low surface energy) and the liquid does not wet the surface.

The contact angles of PS-*b*-PMMA films were measured before and after UV/acetic acid treatment, which was necessary to form the nanoporous structures, to assess the change in the surface energy of the PS-*b*-PMMA film after the treatment. The UV treatment introduces oxygen containing groups which make the otherwise hydrophobic surface very polar. The change in the measured contact angle, θ from a larger value (80°) to $< 50^o$ indicated the presence of polar groups on the nanoporous PS-*b*-PMMA film.

2.2 Atomic Force Microscopy

Atomic Force Microscopy (AFM) is a high-resolution surface imaging technique whereby a very sharp probe precisely maps the topography of a surface during raster scanning of the surface. The probe is brought into very close proximity to the surface (within ca. 1 nm) by microscopic movements of a piezoelectric actuator under an applied voltage. This close proximity invokes a multitude of interactive forces between the tip apex and the sample surface, ranging from adhesion, electrostatic, van der waals, capillary and repulsive forces depending on the tip-sample distance[116]. It is these nanoscale interaction forces that are measured by the atomic "force" microscopy as deflections of the cantilever bearing the probe, with a sensitivity on the order of 10^{-12} N[117-119].

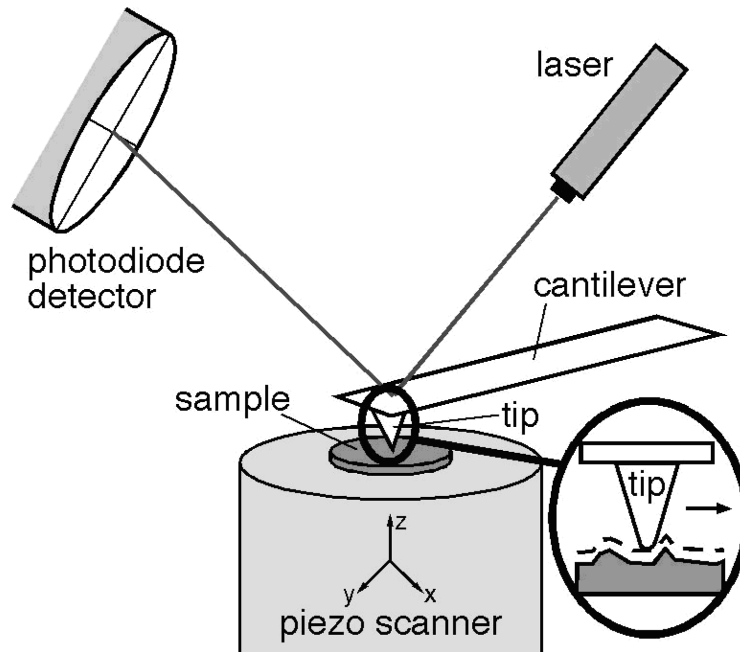

Figure 2.2 Schematic diagram of the AFM showing the basic components. Reprinted with permission from ref [120]. Copyright 2010, Elsevier.

Figure 2.2 shows a typical AFM setup with the force measuring deflection system and the detector[120]. The set up consists of three essential components: a) a sharp tip, typically made from Si or silicon nitride having a pyramidal shape (radius of curvature ~10-100 nm), mounted on the end of a flexible force sensing microcantilever, b) a force transducer, which is the cantilever with a laser beam bouncing off the backside of the cantilever onto a multiple segment photodiode called the position sensitive diode, c) A piezoelectric scanner precisely positions the tip and scans the sample relative to the tip in the x, *y, z* directions. By scanning the probe over the surface (or the sample under the probe) the forces of interaction between the tip and the sample are measured as deflections in the cantilever which are translated into motions of the laser beam over the position sensitive diode. In constant force mode, which measures the local height of the sample, the feedback loop holds the force on the cantilever constant by adjusting the vertical extension of the piezo during the scan. Three dimensional topographical maps of the surface are thus constructed from the piezo's vertical adjustment as a function of the horizontal tip position. In constant height mode, the tip surface distance is held constant during scanning and the interaction force is measured as deflections in the cantilever according to Hooke's law $-\Delta z =$

$\Delta F/$ k where Δz is the deflection in the cantilever caused by the interaction force ΔF and k is the spring constant of the cantilever.

In contact-mode AFM the probe is in mechanical contact with the sample surface throughout the scanning. The interactive forces generally present in contact mode are adhesion force dominated by van der waals forces, capillary force and electrostatic repulsion force. As described above the interaction force is held constant by adjusting the tip to sample distance by the feedback electronics[121]. In tapping-mode AFM a stiff cantilever is oscillated very close to the sample at its resonance frequency. Detection is based on measuring changes in the amplitude of the cantilever when the tip intermittently taps the surface due to attractive forces. The feedback adjusts the vertical height of the piezo scanner to maintain a constant oscillation amplitude of the cantilever. The changes in the vertical piezo extension are plotted as a function of the x, y position of the tip on the sample to generate the topographic image.

Tapping mode AFM was used in this work for imaging the surface topography of nanostructures made from self assembly of the PS-*b*-PMMA diblock copolymer to study the PMMA domain alignment. The PMMA domains were imaged at high lateral resolution which allowed the determination of the domain size from topography images. The micrometer scale structures formed in commercial polymers via the top down lithography method were imaged using contact-mode AFM over a much larger scanning area (100 µm).

2.3 Chemical Force Microscopy

Chemical Force Microscopy (CFM) is an offshoot of AFM that utilizes AFM tips modified with very specific tip functionality to probe surface chemical heterogeneities on surfaces under near native conditions. The operating principles are very similar to that described in the preceding section on AFM. Chemical discrimination, using chemically modified AFM tips such as shown in figure 2.3[120], is based on the differences in magnitude of interactive forces that operate between functional groups immobilized on the tip and those on the surface. Therefore, it is possible via chemical modification with specific functional groups to enhance a specific intermolecular interaction (H-bonding, van der vaals, electrostatic, hydrophobic) and suppress interfering interactions, leading to selectively probing surface functional groups of interest at

micro- to nanoscale regions[120]. The unique advantage of using CFM for mapping surface chemical heterogeneities, as opposed to macroscopic surface techniques such as XPS, contact angle goniometry and Tof SIMS, is its sub-nm spatial resolution. In principle a resolution of ~10 nm can be achieved with very sharp AFM probes[122]. CFM is typically employed in the force-distance spectroscopy mode to measure adhesion forces between tip and sample and in the lateral force microscopy mode to measure frictional forces, while simultaneously tracing the surface topography.

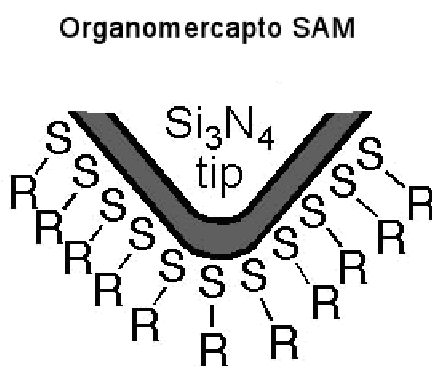

Figure 2.3 Chemically-functionalized AFM tip commonly employed in CFM, (R – COOH,-OH, -NH_2, -CH_3 etc). Reprinted with permission from ref [120]. Copyright 2010, Elsevier.

2.3.1 Force-distance spectroscopy

Force-distance spectroscopy is a procedure used with the typical AFM set-up to measure the adhesion force between a chemically modified tip (in the context of CFM) and the surface when the tip is brought into contact and then pulled away from the surface. The adhesion force is measured as a deflection of the cantilever when the tip is pulled away from the surface. This mode can be used to measure long range attractive or repulsive forces between probe and sample. Figure 2.3[120] shows a typical force-distance curve which plots the vertical displacement of the cantilever as a function of the separation distance between the tip and sample.

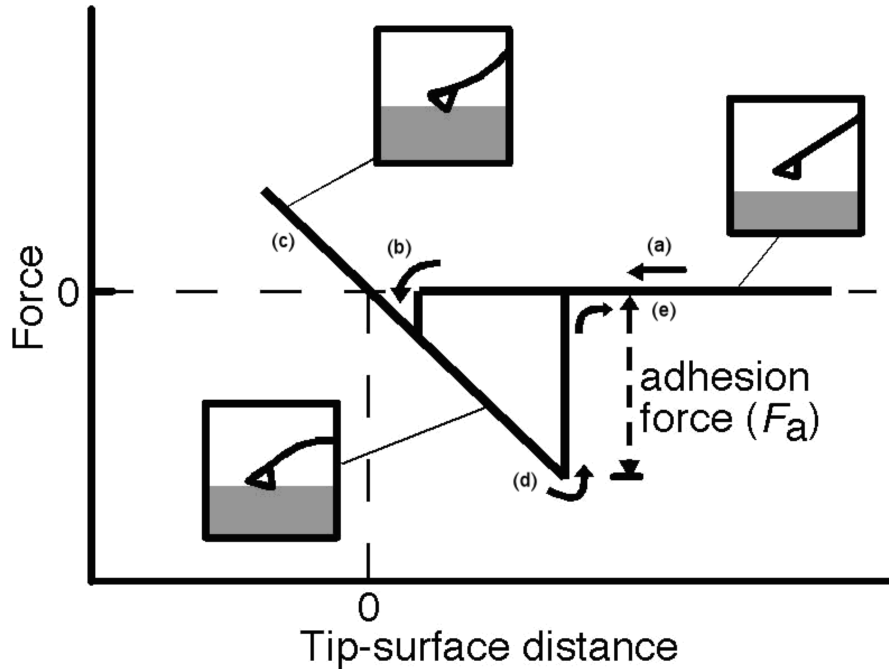

Figure 2.4 Schematic of a force-distance curve -(a) tip approaching surface (b) tip jumps into contact (c) tip indents into sample (d) tip breaks contact with the surface when the spring constant overcomes the adhesion force between tip and sample (e) tip moving away from the surface to its equilibrium position. Reprinted with permission from ref [120]. Copyright 2010, Elsevier.

The cantilever deflection (Δz) *at* the point of breaking contact with the surface is converted into the adhesion force (F_a) by multiplying with the spring constant of the cantilever (k) , since $F_a = k\,\Delta z$. The adhesion force is commonly referred to as the "pull-off" force since it is the amount of work that has to be done to "pull" the tip away from the surface. The force of adhesion (F_a) is related to the work of adhesion W_{ad} needed to rupture the tip and sample contact, by[123]:

$$F_a = (3/2)\pi R W_{ad} \qquad \text{Eq. 2-2}$$

where R is the radius of curvature of the tip. The work of adhesion W_{ad} is related to the surface free energies of the functional groups exposed on the contacting surfaces and the medium in

which the tip-sample resides. Hence, the work needed for separating the sample and tip is expressed as the balance of interfacial free energies of the tip-liquid (γ_{tl}) sample-liquid (γ_{sl}) and tip-sample interfaces (γ_{st}) given by:

$$W_{ad} = \gamma_{sl} + \gamma_{tl} - \gamma_{st} \qquad \text{Eq. 2-3}$$

Contact mechanics theories such as the JKR (adhesive contact) and Hertzian (elastic contact) predict that the adhesion force is a function of the tip-sample contact area. This has important implications in interpreting adhesion forces between tip and sample for corrugated surfaces, such as the etched PS-*b*-PMMA films made in this work. These surfaces contain µm- to nm-scale corrugations and are chemically heterogeneous, and thus any change in tip-surface force in CFM can be attributed to changes in tip-surface contact area and/or chemical interactions. This will be discussed in chapter 4 section 4.2. Equation 2-3 suggests that by carefully choosing the tip functionality, in other words by controlling the surface free energy, and the imaging medium one can selectively enhance the magnitude of a particular intermolecular interaction while suppressing the others. This becomes particularly important for high contrast friction imaging of chemically distinct domains[124, 125].

CFM in the force-distance spectroscopy mode was used in this research to measure the adhesion force between a –COOH terminated tip and the surface of a UV/acetic acid etched PS-*b*-PMMA film to determine the identity of the functional groups present on the surface. Details of the measurement and data analysis are discussed in detail in the relevant chapter.

2.3.2 Lateral Force Microscopy

Lateral Force Microscopy, (LFM) is yet another technique based on AFM to perform chemically sensitive imaging by measuring lateral forces or more commonly friction forces between the tip and sample. This is done by measuring the torsional deflection of the cantilever when the substrate is scanned perpendicular to the long axis of the cantilever (see figure 2.5). This manner of scanning increases the sensitivity of the friction force measurements. The friction force at the tip and sample is related to the lateral twist of the cantilever around its long axis and the torsional spring constant. LFM is always operated in the contact-mode and more destructive than measuring adhesion forces due to the large shear forces between tip and sample during

scanning. In spite of this, LFM is ideal for chemically-selective mapping due to its high lateral resolution of 10-30 nm[122]. The magnitude of friction force, and thus the contrast of friction images, can be tailored by the chemical functionalization of an AFM tip on the basis of hydrophobic, hydrogen bonding and electrostatic interactions between terminal functional groups on tip and substrate.

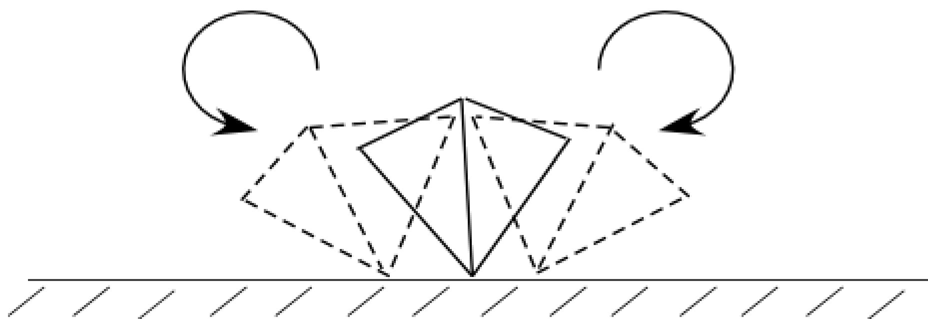

Figure 2.5 Torsional deflection of the probe and cantilever during lateral scanning of the sample relative to the tip.

The 20-nm domains of the UV/acetic acid etched PS-*b*-PMMA films was imaged in the friction force mode, in an apolar medium, using chemically modified tips with different surface energies to enhance chemical contrast between the PS and PMMA domains.

Whether in the force-distance spectroscopy mode or friction force mode, CFM has the unique advantage of high spatial resolution, limited only by the range of operating forces or by the sharpness of the probe tip, compared to the lateral resolutions of other surface characterization techniques[122] listed in table 2.1. This justifies our extensive use of AFM and related techniques outlined above, for topography and chemically sensitive imaging of the nanoscale structures formed in the polymers.

Table 2.1 Common surface characterization techniques and their lateral resolutions.

Technique	Time of flight Secondary Ion Mass Spectrometry	X-ray Photoelectron Spectroscopy	MALDI - Mass Spectrometry	Raman Micro-Spectroscopy	Reflection IR	Chemical Force Microscopy
Lateral Resolution	80 nm - 1 um	2 um - 25 um	30 um - 50 um	0.5 um - 1 um	30 um -50 um	10 nm - 50 nm

2.4 Conductance measurements

Ionic conduction between two electrodes placed in an electrolytic solution, such as KCl, is measured by determining the resistance (*R*) to current flow in solution or its reciprocal, the conductance (*L*). The conductance *L* of a section of an electrolyte immersed in an electric field is a function of the cross-sectional area, *A* of the section and is inversely proportional to the length (*l*) of the section given by[126]:

$$Conductance(L) = \kappa A / l \qquad \text{Eq.2-4}$$

where κ is the conductivity in S cm^{-1} and *L* is the conductance in units of Siemens (S). The term *A/l* is the cell constant and is used to convert measured conductance values to conductivity of the electrolyte solution. The conductivity, κ is an intrinsic property of an electrolyte and represents the movements of both the cations and anions present in solution. The conductivity of an electrolyte is proportional to the bulk ionic concentration, the magnitude of the cationic and anionic charges and the limiting velocities of the ions in an electric field of unit strength (termed the “mobility” with units of cm^2/Vs).

Conductance is related to the resistance in the solution between two electrodes by:

$$Conductance(L) = \frac{1}{R} \qquad \text{Eq.2-5}$$

The resistance (R) for a segment of electrolyte in an electric field is directly proportional to its length, l along the electric field and inversely proportional to its cross-section area, A perpendicular to the field given by:

$$R = \rho \frac{l}{A} \qquad \text{Eq.2-6}$$

and κ(conductivity) = $1/\rho$ so that Eq.2-6 can be re-written to show the relationship between the resistance R and conductivity of a segment of an electrolyte as:

$$R = \frac{l}{\kappa A} \qquad \text{Eq.2-7}$$

The interrelationships between resistance, conductance and conductivity of an electrolyte suggest that these parameters can be ascertained by a simple measurement of the current (I) through an external circuit when a voltage (V) is applied across the electrodes immersed in an electrolyte, since according to Ohm's law $R = V / I$. This was one of the characterization tools used in the work done in chapter 5, where the conductance of KCl, at different concentrations, inside the nanoporous PS-*b*-PMMA monolith was measured from *I*-*V* curves such as the one shown in figure 2.6(b) using the set up in figure 2.6(a). The slope of the *I*-*V* curve gives the reciprocal of the resistance which is the conductance, L.

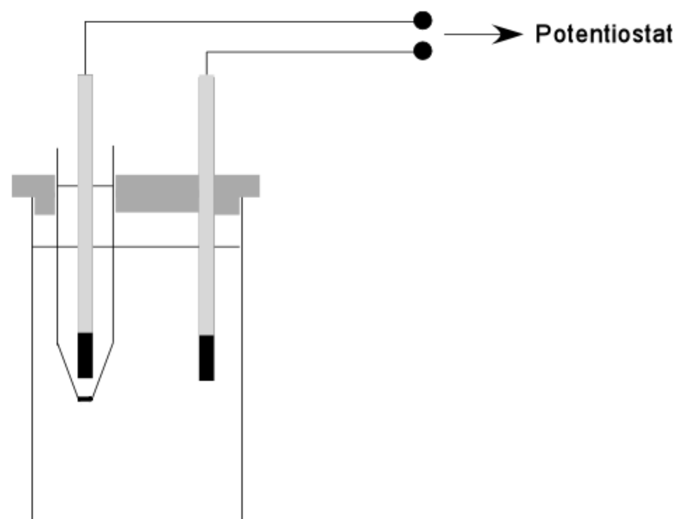

(a)

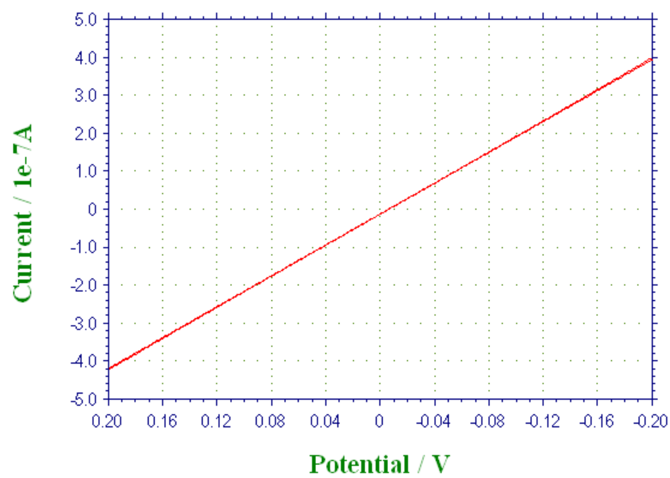

(b)

Figure 2.6 (a) Schematic of the electrochemical cell, b) Typical cyclic Voltammogram (*I-V* curve) obtained with an Ag/AgCl working electrode inside a micropipette filled with a 0.1M KCl solution vs. a reference Ag/AgCl electrode placed in the bulk KCl solution.

2.5 Fluorescence Emission Spectroscopy

Fluorescence based detection methods are extremely sensitive and have detection limits as low as 10^{-17} M[127]. The flux through the PS-*b*-PMMA nanoporous monoliths described in chapter 5 is very low and at any given instance the maximum concentration of the diffusing molecules in the receiving cell is < 2 nM. Therefore, given its extreme sensitivity fluorescence spectroscopy was an ideal detection method for measuring the concentration of the diffusing dye molecules in this work.

Fluorescence is a two-photon process where the excitation photon, at a shorter wavelength, excites a ground-state electron in the fluorescent molecule to a higher energy state as shown in figure 2.7. The excited electron relaxes rapidly before coming back to the ground state with reemission of light. The energy of the absorbed photon is higher than that of the emitted photon due to vibrational relaxation before coming back to the ground state. Hence the emitted light is at a longer wavelength than the excitation light which is characteristic of fluorescence. It is this very feature that makes fluorescence a very sensitive method for detection because one can use light of a particular wavelength and detect fluorescence emission at a longer wavelength without any interference from the source light. Furthermore, detection of the emission beam is performed at right angles to the excitation beam hence the background from the source is further cut down.

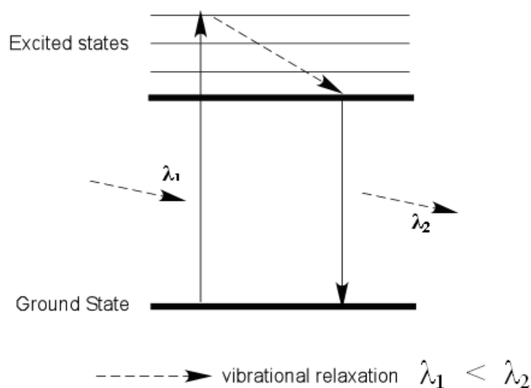

Figure 2.7 Schematic showing the electronic excitation and vibrational relaxation states of a molecule during fluorescence emission.

The fluorescence signal (P_F) is related to the concentration, C of the molecules by[128]:

$$P_F \approx KP_o(2.303\varepsilon(\lambda)\,b\,C) \qquad \text{Eq.2-8}$$

where K is a constant dependent on the fluorescence quantum yield, $\varepsilon(\lambda)$ molar absorptivity at the excitation wavelength, P_o power of the incident light and *b* is the path length. P_F is a linear function of concentration *only* at low concentrations. The above relationship does not hold true at higher concentrations due to reabsorption of the emitted fluorescence by the molecules. The concentration of the molecules in the receiving cell was < 2nM in the flux experiment described in chapter 5.

Chapter 3 - Direct-Write Multiphoton Photolithography: A Systematic Study of the Etching Behaviors in Various Commercial Polymers

Shaida Ibrahim, Daniel A. Higgins and Takashi Ito

Reproduced with permission from

Langmuir, **2007**, *23*, 12406-12412. Copyright 2007 American Chemical Society

Introduction

This chapter describes a top-down approach to fabricate sub-micron scale patterns via ablative multiphoton etching of commercial polymer films. A systematic study of the power dependence and spatial resolution of ablative multiphoton photolithography in several commercial organic polymers having different chemical structures and molecular weights is described (see figure 3.1(b)). These measurements provide important new data on the etching mechanism. They also provide a clear demonstration of the general applicability of the method to a variety of polymers and allow for identification of the polymers best suited for use with this technique. Finally, as a further demonstration of its potential applications, the transfer of sub micrometer-scale surface features onto polydimethylsiloxane (PDMS) via soft lithography is described.[34, 129]

One method for improving the resolution of optical photolithography involves the use of multiphoton excitation to trigger photochemical or photophysical processes in resist films.[23] The resolution afforded by this method is governed in part by the diffraction of light. Under such conditions, resolution on the order of $0.61\lambda / (NA \bullet n^{1/2})$ is expected, where λ is the wavelength of light employed, NA is the numerical aperture of the objective lens and n is the order of the non-linearity. However, the lateral resolution obtained in many studies far exceeds that predicted by the diffraction of light alone.[33, 130-132] Resolution beyond the diffraction limit is often attributed to strong thresholding in the multiphoton-driven chemical and physical mechanisms involved, although careful chemical development[130] of the exposed resist or the use of additives such as

radical quenchers[131] is sometimes employed. As in previous demonstrations of polymer film ablation,[4] etching is believed to be initiated by multiphoton excitation of chromophores intrinsic to the polymer. Electronic excitation of the polymer results in its depolymerization and evaporation from the substrate surface via either photochemical or photothermal processes.[4]

The top-down approach adopted in this work can be used to fabricate arbitrary patterns with sub-micron scale resolution in polymer thin films without the use of a photomask, dye dopants or chemical development steps.

3.1 Experimental

3.1.1 Chemicals and Materials

Poly(methylmethacrylate) (PMMA), poly(ethylene oxide) (PEO) and poly(butylmethacrylate) (PBMA) were all purchased from Aldrich. Polystyrene (PS) was obtained from Polymer Source. Sodium poly[2-(3-thienyl)ethyloxy-4-butylsulfonate] (PTEBS) was purchased from American Dye Source. The molecular weights and glass transition temperatures of all polymers employed are summarized in Table 1. Chlorobenzene was obtained from Mallinkrodt Chemical. All chemicals were used as received. Glass coverslips (1” x 1”; 200 µm thick) were purchased from Fisher, and used after cleaning in a Harrick plasma cleaner for 5 min.

3.1.2 Preparation of Polymer Films

PMMA, PS and PBMA films were prepared by spin-coating (2000 rpm) chlorobenzene solutions (1-8 wt%) of these polymers onto glass coverslips. The polymer concentration was selected in each case to give films of a particular thickness. The films were subsequently annealed at 120 °C in a vacuum oven for ~12 h. PEO films were prepared by spin-coating (2000 rpm) from aqueous solution (0.5 wt%). PTEBS films were prepared by casting a 1 wt% aqueous solution of the polymer onto glass coverslips. They were subsequently dried at room temperature under vacuum for ~2 days. The thickness of all films was measured using a J. A. Woollam alpha-SE spectroscopic ellipsometer. AFM images of the etched samples yielded very similar film thicknesses. Polymer films for UV-Vis measurements were prepared on quartz substrates as described above for glass substrates. The thickness of the PTEBS film is likely inaccurate because the film was not uniform (prepared by casting an aqueous PTEBS solution

and dried). UV-Vis spectra of the films were measured on a Hewlett-Packard HP 8453 UV-vis spectrometer, using a quartz substrate as a blank.

3.1.3 Direct-Write Multiphoton Photolithography

Experimental Setup

A polymer-coated coverslip was loaded onto a piezoelectric sample scanning stage, with closed-loop x-y feedback control, mounted on an inverted epi-illumination microscope (Figure 3.1(a)).[133] The light source used for etching was a mode-locked Ti:sapphire laser outputting 170 fs pulses of light centered at 870 nm and having a repetition rate of 76 MHz. Light from the laser was first passed through polarization optics to control the incident power, and then through an electronic shutter to control irradiation of the sample. The light was then reflected by a dichroic beam splitter into the back aperture of a 1.3 numerical aperture (*NA*), 100x oil-immersion objective. The objective produced a diffraction limited focused spot of light having ~570 nm $1/e^2$ diameter in the polymer film to obtain the intensities necessary for etching. Etching was accomplished by raster scanning the polymer film over the focused laser spot (pixel size: 100 nm; pixel time: 40 ms; scan rate: 2.5 μm/s). Irradiation of the sample was controlled by a pattern fed into the microscope control software (written in house- by *Dr.Daniel A.Higgins*) via opening and closing of the electronic shutter, allowing for arbitrary patterns to be fabricated in the polymer film. Incident laser powers given below are estimates of the power at the objective focus, and were measured outside the microscope, just prior to the dichroic beam splitter. Estimated values of the laser power required for the etching are lower than those used in the previous studies by the Higgins *et al* group[33, 43]because of differences in the irradiation time at each pixel and a recent reconfiguration of the microscope and replacement of the original dichroic beam splitter.

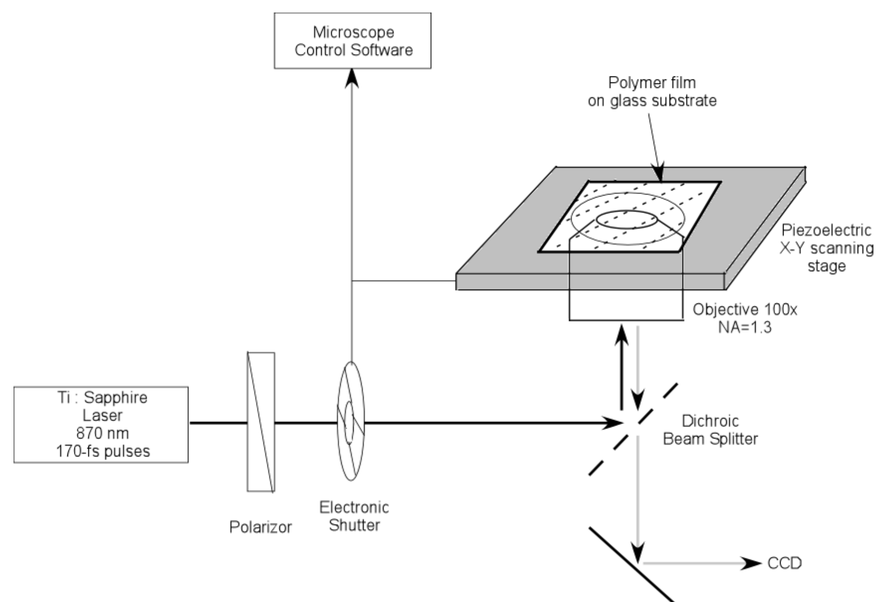

(a)

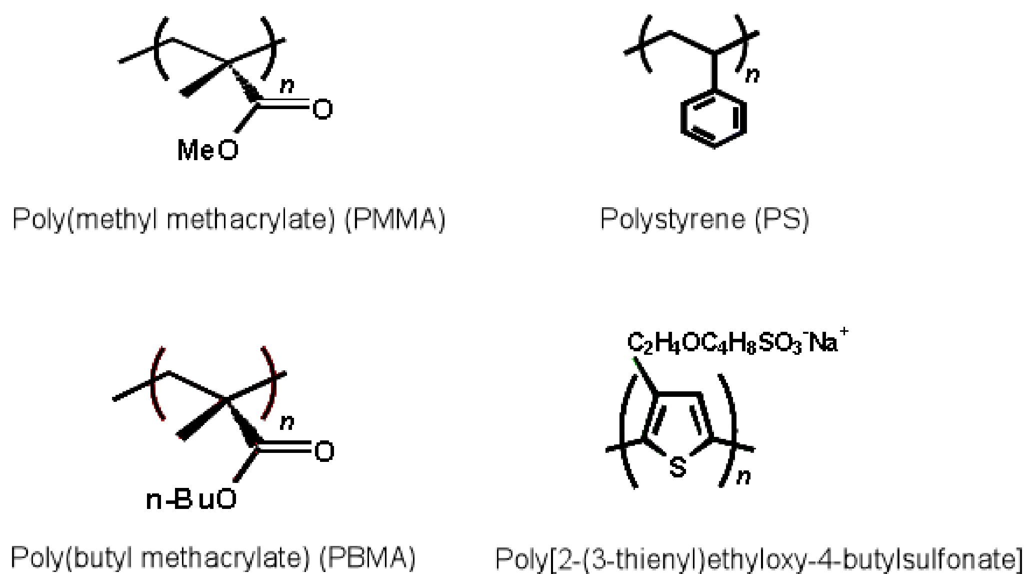

(b)

Figure 3.1 (a) Schematic of the sample scanning confocal microscope used for multiphoton photolithography (b) Chemical structures of commercial neat polymers used for multiphoton-induced etching.

3.1.4 Pattern Transfer Using PDMS Soft Lithography

A drop of uncured PDMS (Sylgard 184, Dow Corning) was sandwiched between a glass coverslip covered with a patterned PMMA thin film (the mold) and a glass slide coated with a trichloro(3,3,4,4,5,5,6,6,7,7,8,8,8-tridecafluorooctyl)silane (Fluka) self-assembled monolayer. The PDMS was subsequently cured at 60 °C for 2 hours. The glass coverslip was then gently removed from the cured PDMS.

3.1.5 Atomic Force Microscopy Measurements

Detailed characterization of the etched samples was performed using contact-mode atomic force microscopy (AFM) in air. A Digital Instruments Multimode AFM with Nanoscope IIIa electronics was employed. Contact-mode pyramidal AFM tips were purchased from Veeco.

3.2 Results and Discussion

3.2.1 Pattern Formation via Direct-Write Multiphoton Photolithography

Figure 3.2(a) shows a typical AFM image of patterns fabricated in a ~100 nm thick 120K PMMA film using direct-write multiphoton photolithography. These patterns were fabricated by simply irradiating the sample with focused laser light at 870 nm. Neither dye additives nor chemical development procedures were employed, demonstrating that this method provides a simple means to fabricate sub micrometer-scale features in thin polymer films. Furthermore, arbitrary patterns can be prepared by this method. As a demonstration of this attribute, a text pattern (designating polymer type and film thickness) was written with sub micrometer resolution in the upper left corner of Figure 3.2(a). This figure also shows two additional types of patterns. On the right, several 5 x 5 μm^2 squares were etched into the film at different incident laser powers. These patterns provide valuable information on the power dependence of the etching process. At the bottom left, a number of gratings (10 x 10 μm^2) were fabricated as a means to assess the etching resolution.

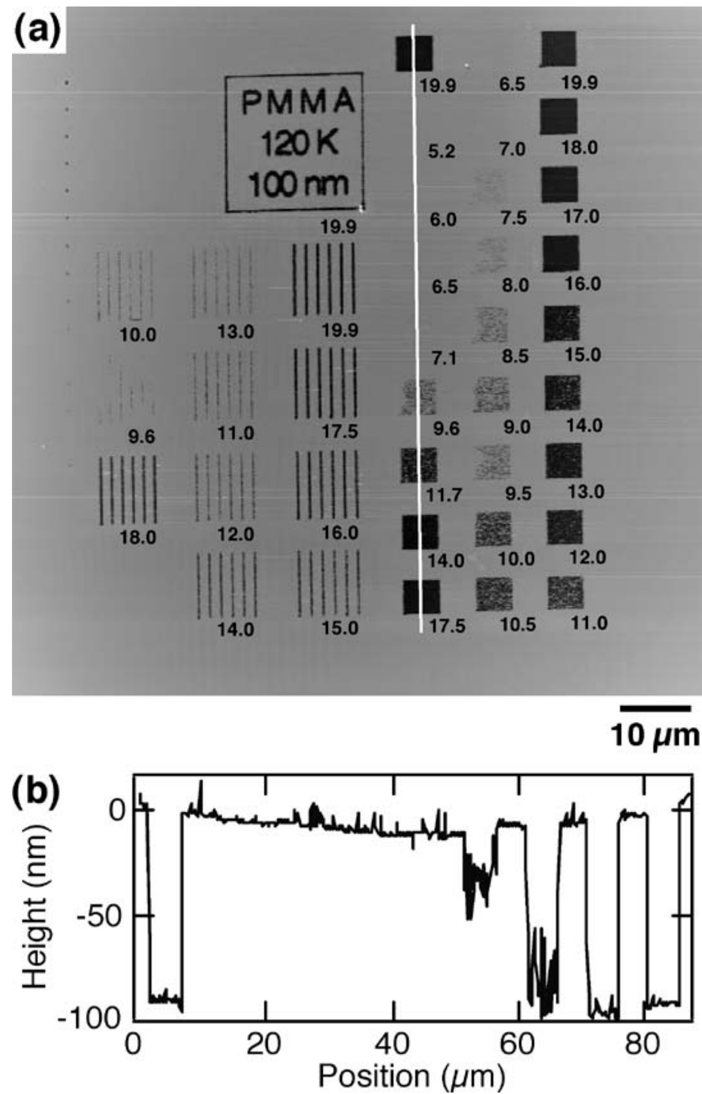

Figure 3.2 (a) AFM topography image of patterns fabricated in a 120K PMMA thin film (~100 nm thick) using direct-write multiphoton photolithography. The average laser powers (in mW) used for polymer etching have been appended to the image. (b) Cross-sectional profile taken along the line shown in (a).

3.2.2 Power Dependence of the Etching Process

The 5 x 5 μm^2 square patterns in Figure 3.2(a) show that etching of the 120K PMMA film occurred at 7.5 mW or higher laser powers, with an irradiation time of 40 ms/pixel. Figure 3.2(b) shows a line profile (AFM topography) taken along the line shown in Figure 3.2(a). This figure shows that no apparent etching occurred at 7.1 mW (or lower powers), for which etching

is difficult to induce and quantitative etch depths are difficult to obtain. In contrast, significant etching occurred at 9.6 mW and higher incident powers. The surfaces of the etched regions produced at 9.6 and 11.7 mW were much rougher than those obtained at 14.0, 17.5 and 19.9 mW. The greater roughness found at intermediate powers is a result of strong “thresholding” in the etching process and small variations (~5%) in the laser output. Incomplete removal of the polymer debris formed during etching may also contribute. At powers of 14.0 mW and higher, the bottom surfaces of the etched regions are much smoother, indicating that the polymer film was almost completely removed. Indeed, the depth of the etched patterns at these higher powers is similar to the film thickness obtained by spectroscopic ellipsometry.

The abrupt power-dependent change in etching behavior is clear evidence for the nonlinear (multiphoton) nature of the etching process.[33, 43] Figure 3.3 plots etch depth vs. incident laser power for two PMMA films having thicknesses of 130 nm and 460 nm. Both films were prepared from 15K PMMA. Etching started at very similar powers in both, and also saturated (reflecting complete removal of the film) at similar powers. Such a result would be expected if the etching process involved multiphoton absorption by the UV chromophores of the polymer (i.e. the methacrylate groups in the case of PMMA). The involvement of multiphoton processes is also supported by the fact that etching was not observed with the laser operating in continuous wave mode, indicating that very high peak intensities are required.[33] In addition, the diameters of holes etched in the polymer films by single-point irradiation were smaller than the diameter of the diffraction-limited Gaussian beam profile at the microscope focus.[33] Finally, as has been previously shown, PMMA can be decomposed by UV irradiation,[4, 134, 135] suggesting it can also be decomposed via multiphoton absorption. Support for this conclusion is also provided by previous demonstrations of PMMA ablation using near-IR lasers.[41, 42]

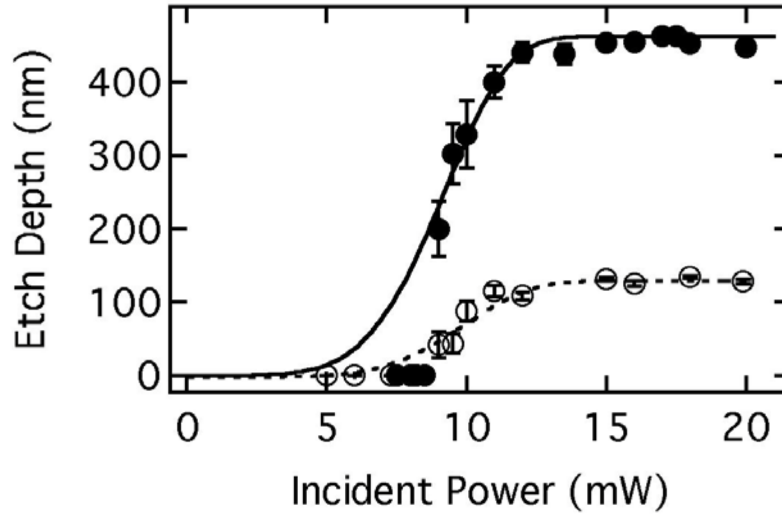

Figure 3.3 Laser power dependence of etch depth for two 15K PMMA films having different thicknesses (~120 nm, open circles, and ~450 nm, filled circles). Etch depth was measured from AFM cross-sectional profiles of 5 x 5 μm² square patterns fabricated at different laser powers. The dashed and solid lines show fits to the data using Eqn. 4.

More quantitative information on the nonlinear nature of etching can also be obtained from the power dependent etching data shown in Figure 3.3. Multiphoton etching can be modeled as a simple kinetic process. In this model, etching is assumed to occur by multiphoton-induced depolymerization[4] of the polymer:

$$Polymer + nPhotons \rightarrow mFragments \qquad \text{Eq.3-1}$$

Assuming the kinetics are first order in the polymer concentration, C_{poly}, in the irradiation volume and *n*th order in the photon flux *P* (which is directly proportional to the incident power), the rate of polymer decomposition may then be written as:

$$\frac{d(C_{poly})}{dt} = -kC_{poly}P^{n} \qquad \text{Eq.3-2}$$

where k is the rate constant for polymer decomposition and t is time. Rearranging and integrating this expression yields the concentration of polymer remaining after etching for time τ at a given P:

$$C_{poly}(\tau, P) = C_{poly}(0)\exp(-k\,\tau\,P^{n}) \qquad \text{Eq.3-3}$$

Here, $C_{\text{poly}}(0)$ is the initial polymer concentration before etching. The irradiation time τ is a multiple of the pixel time and depends on the number of times a given sample region is scanned through the focal volume of the microscope. Upon relating polymer concentration in the irradiation volume to film etch depth, $D_{\text{poly}}(\tau,P)$, the following equation is obtained:

$$D_{poly}(\tau, P) = D_{poly}(0)\left[1 - \exp(-k\,\tau\,P^{n})\right] \qquad \text{Eq.3-4}$$

where $D_{\text{poly}}(0)$ is the unetched film thickness.

Fitting of the data shown in Figure 3.3 to Eq.3-4 yields $k\tau = 4\text{x}10^{-6}$ and $n = 5\pm1$ for the thin film. Similarly, for the thicker film, $k\tau = 7\text{x}10^{-6}$ and $n = 5\pm1$. For nonlinear systems, the value of n is the primary factor governing the *slope* of the etch depth vs. incident power plot in the transition region (i.e., powers above threshold but below saturation). Processes exhibiting greater nonlinearity yield much steeper slopes (i.e. larger n values). Likewise, the value of $k\tau$ is the primary factor in determining the “threshold” for etching for highly nonlinear processes. Etching processes that occur at a greater rate exhibit a lower power threshold. Unfortunately, while the n values determined by fitting the experimental data yield reasonable error bars, the $k\tau$ values are much more sensitive to errors in the measurement of etch depth. Errors in the $k\tau$ values obtained are usually similar to the value itself. Because of its relationship to the etching threshold, slight variations in the microscope focus (i.e. $< 10\%$ variations in the spot radius) lead to substantial variations in the value of $k\tau$ obtained. The same focal variations yield far less significant variations in the value of n. Therefore, the discussion below is limited to the order n of etching in each film.

The n values determined from the data in Figure 3.3 (i.e., $n = 5$ in both cases) suggest the etching process is highly nonlinear, involving absorption of as many as five photons by the

polymer. The actual order of the process is expected to be somewhat lower, but still within the error bars obtained from these data. PMMA absorbs light of wavelengths shorter than 240 nm (its absorption maximum is at 213 nm; see Figure 3.5(a)). Therefore, it is expected that etching could occur by absorption of as few as four photons at 870 nm. The larger value obtained for n by fitting the data may be partly due to the difficulties in measuring small etch depths at low incident powers. The large error bars (reflecting standard deviations of the etch depth measured at each power) obtained in the transition region also contribute. Large errors in the transition region result from greater roughness of the etched areas (see Figure 3.2(b)). At the highest laser powers, the error bars become very small due to the complete removal of the polymer films (vide supra).

3.2.3 Comparison of Etching Behavior for Different Polymers

In addition to being initiated by multiphoton absorption, the etching process is also believed to involve thermal vaporization of the polymer fragments created.[4] Systematic studies of etching in a series of polymers having different chemical structures, glass transition temperatures, and molecular weights provide the means to further explore the nonlinear origins of etching and the impacts of thermal phenomena.

Figure 3.4 shows the relationship between etch depth and incident laser power for films of (a) 120K PMMA, (b) 120K PS, (c) PBMA and (d) PTEBS. As with PMMA (Figures 3.3 and 3.4 a), an abrupt power-dependent transition in etching was observed for both PS and PBMA (Figures 3.4 (b) and (c)). Difficulties in etching and in measuring the etch depths at relatively low powers (i.e. < 8 mW in the case of PS and < 7 mW in PBMA) prevented the recording of etch depth values at these powers. The regions etched at intermediate powers were also found to be rough for these two polymers. Again, such roughness may be due to variations in the efficiency of the etching process, or to incomplete vaporization of the polymer fragments created.

At high powers, the bottom of each etched area was found to be smooth (vide supra). These results suggest that 120K PS and PBMA films are also etched via a multiphoton process. Considering these polymers absorb light of wavelengths shorter than 280 nm and 240 nm (absorption maxima are 262 nm and 216 nm, respectively; see Figure 3.5), their etching processes likely involve three and four photon absorption, respectively, at 870 nm.[33] Fits to the

data shown in Figures 3.4 (b), (c) yielded values of $n = 3 \pm 1$ and 4 ± 1, in support of this hypothesis. PEO films were also etched in a similar manner, although quantitative data on the etching process could not be obtained because of difficulties encountered in preparing uniform films.

In stark contrast to the abrupt etching transitions observed for PMMA, PS and PBMA, PTEBS films could be etched even at very low laser powers (Figure 3.4(d)). The etch depths for PTEBS also increased much more gradually with increasing laser power. Furthermore, the surface of the etched area was relatively smooth at all the laser powers examined, as indicated by the relatively small error bars shown (barely visible). PTEBS absorbs visible light of wavelengths shorter than 600 nm (its absorption maximum is at 434 nm; see Figure 3.5), and thus etching by 870 nm laser light might occur via absorption of as few as two photons. The smoother etched regions observed for PTEBS are likely due to the weaker power dependence of etching expected for a second order process, compared to the higher order processes involved in etching the other polymers. Less "thresholding" occurs in lower order processes and hence, etching is expected to be much less sensitive to variations in the laser output and to variations in the polymer film properties.

Table 3.1 Glass Transition Temperatures, *n* Values, and Edge Sharpness for the Polymers Examined.

polymer	MW[a]	T_g (°C)[a]	$n^{b,c}$	edge sharpness[b,d]
15 K PMMA	15 000	82	7 ± 3	0.57 ± 0.04
120 K PMMA	120 000	99	6 ± 2	0.52 ± 0.07
350 K PMMA	350 000	122	7 ± 1	0.43 ± 0.03
16 K PS	15 500	102	5 ± 3	0.43 ± 0.01
120 K PS	119 600	102	3 ± 1	0.45 ± 0.03
433 K PS	432 600	102	3 ± 1	0.42 ± 0.04
PBMA	337 000	15	4 ± 1	0.32 ± 0.03
PTEBS	269 000	e	2 ± 1	0.17 ± 0.06

[a] Provided by the manufacturers. [b] "Average ± standard deviation" of data obtained from at least three separate films. [c] Values obtained by fitting etch depth vs incident power using eq 4. [d] Measured from the cross-sectional profiles of gratings (Figure 4). [e] No T_g or melting point was observed up to 500 °C, according to the manufacturer.

Reproduced with permission from *Langmuir*, **2007**, *23*, 12406-12412. Copyright 2007 American Chemical Society

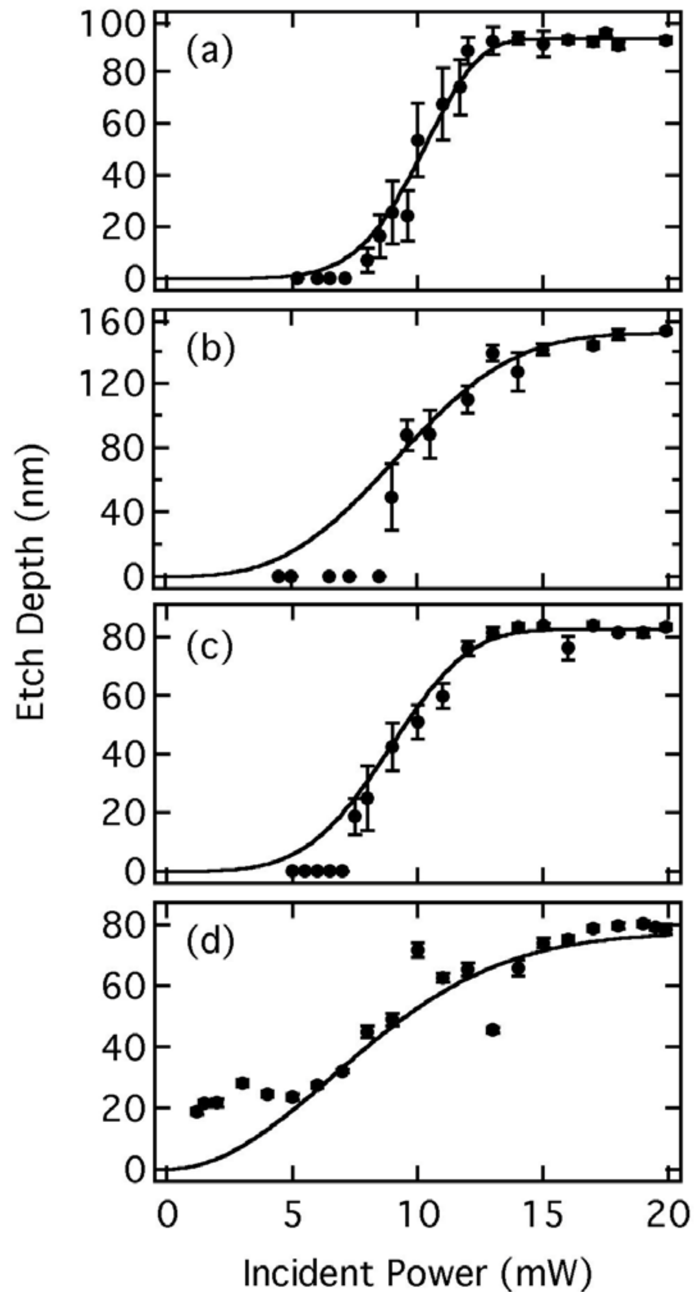

Figure 3.4 Laser power dependence of etch depth for (a) 120K PMMA, (b) 120K PS, (c) PBMA and (d) PTEBS. Etch depth was measured from AFM cross-sectional profiles of 5 x 5 μm^2 square patterns fabricated at different laser powers. The solid lines show approximate fits to the data using Eq. 3-4 and the average *n* values given in Table 3.1.

UV-Vis spectra taken by *Dr. Takashi Ito*

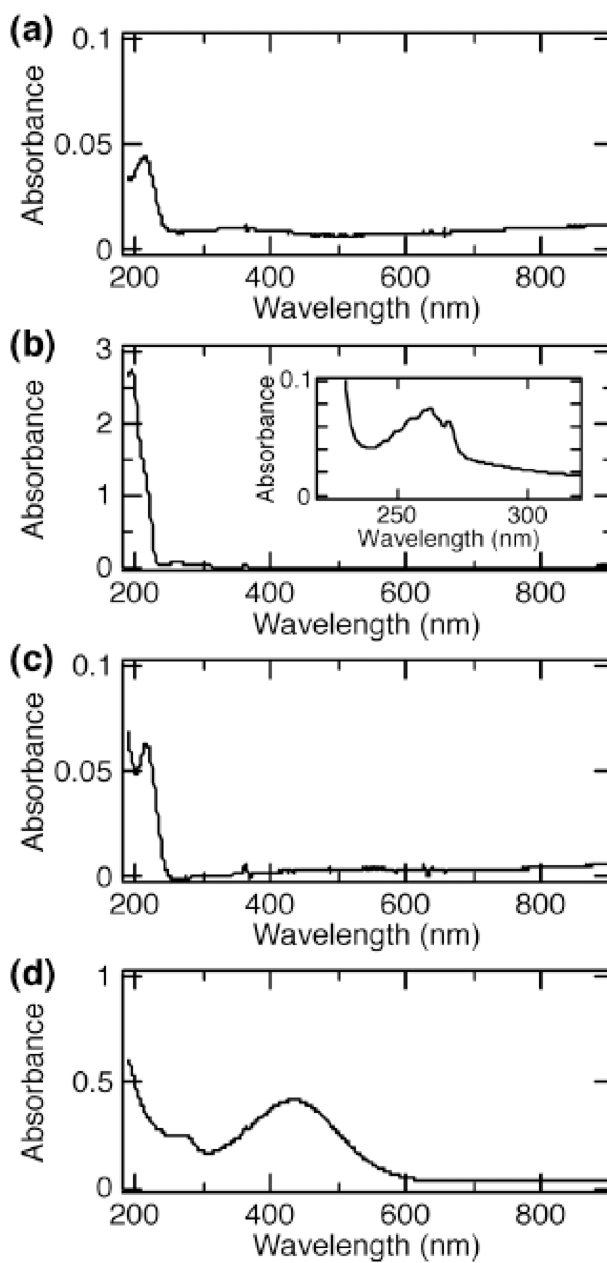

Figure 3.5 UV-Vis spectra of (a) 15K PMMA (150 nm thick), (b) 15K PS (130 nm thick), (c) PBMA (300 nm thick) and (d) PTEBS (ca. 70 nm thick).

The order of the nonlinear processes (i.e. the number of photons simultaneously absorbed by individual chromophores) involved in etching all polymer films examined are summarized in Table 3.1. The values of n obtained decrease in the order PMMA ≥ PBMA > PS > PTEBS, and appear to be independent of polymer molecular weight, film thickness and glass transition temperature (T_g). Taken with the discussion presented above, these results prove the etching process is triggered by multiphoton absorption. They are consistent with depolymerization of the polymer and subsequent thermal evaporation of the fragments.[4] The energy for thermal evaporation is also transferred to the polymer via multiphoton absorption. The involvement of depolymerization and thermal evaporation processes in polymer etching suggests that the etching mechanisms may be similar to those of UV laser ablation.[4] Although there is still significant debate as to the real mechanisms by which laser ablation occurs, it is clear that both photochemical and photothermal processes are involved.[4] The extent to which each participates is likely to depend on the wavelength of the incident light and the order of the nonlinear optical processes involved.[38] Detailed analysis of the evaporated fragments[38, 40] in the present experiments would provide valuable additional information on the multiphoton etching mechanisms involved.

3.2.4 Edge Sharpness for Different Polymers

The edge sharpness of the etched patterns produced by multiphoton photolithography is important because it defines the smallest feature sizes that can be fabricated using the technique. This has important implications for the suitability of polymers for high resolution device fabrication. As has been previously demonstrated by Higgins and ito *et al* [33, 43] and by others,[23] multiphoton methods can be used to fabricate sub micrometer-resolution patterns in polymer films. Here, surface relief gratings were fabricated in a series of polymer films to explore this issue.

Figure 3.6 shows representative cross-sectional profiles of gratings formed in films of (a) 15K PMMA, (b) 16K PS, (c) PBMA and (d) PTEBS. These gratings were fabricated using laser powers at which the polymers were completely removed (ca. 16 mW) from the substrate surface (see figure 3.6(e)). It is clear that the sharpest patterns could be formed in 15K PMMA. In contrast, all other polymers exhibit significant "rounding" of the edges of etched regions.

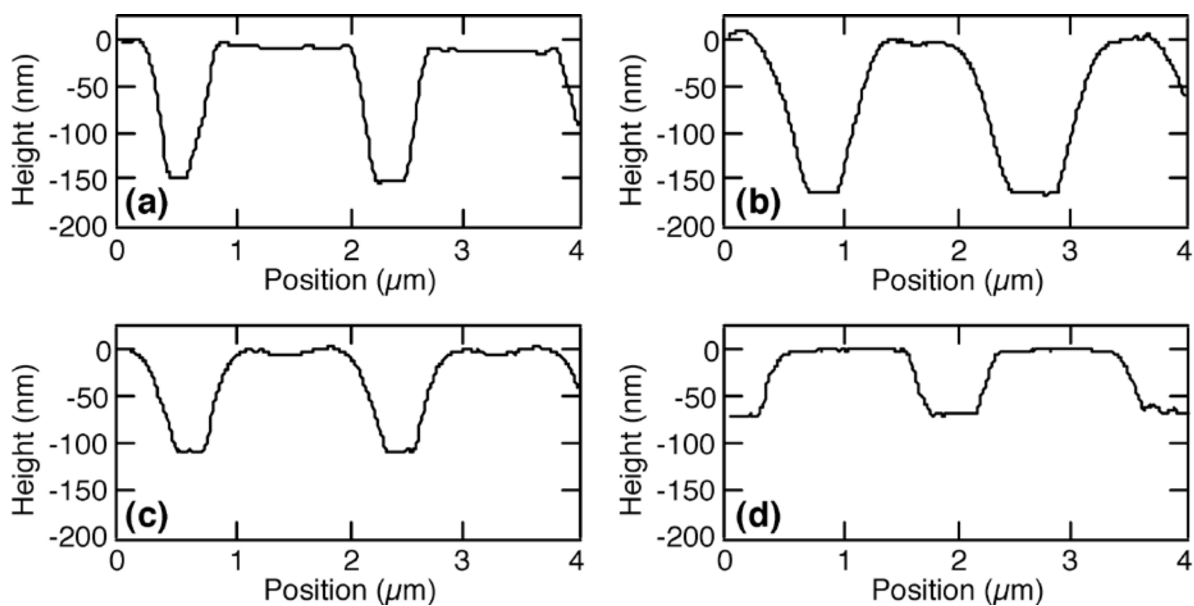

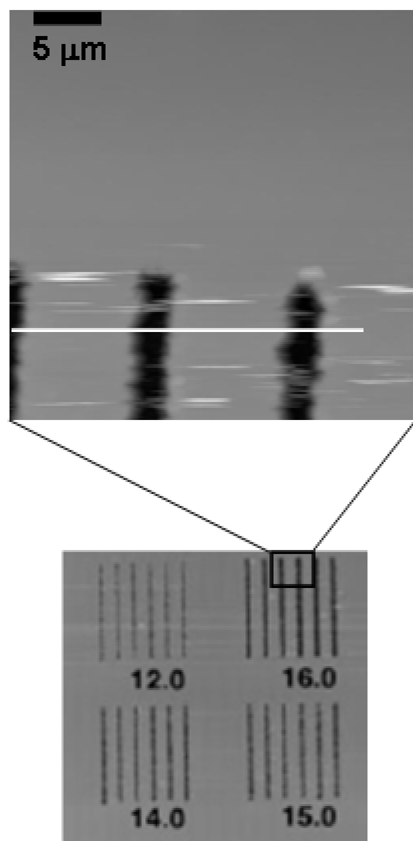

Figure 3.6 Cross-sectional profiles of gratings fabricated in (a) 15K PMMA, (b) 16K PS, (c) PBMA (d) PTEBS and (e) 10 x 10 μm^2 surface relief gratings fabricated in PMMA.

Edge sharpness, and hence, etching resolution in each film was assessed by determining the slope of the edge region. In determining edge sharpness, the depths of trenches etched into each sample were divided by the lateral distances from fully etched to unetched polymer. Edge sharpness was found to be independent of film thickness. Data obtained from PMMA films yielded values of 0.57 ± 0.04, 0.63 ± 0.12, and 0.56 ± 0.13 for films having thicknesses of 120-140 nm, 360-nm and 480-nm, respectively. Note that the edge sharpness values are likely reduced somewhat by convolution with the AFM tip. The maximum sharpness that would be observed for an infinitely sharp edge would be 1.0, for the contact mode tips employed. Table 3.1 summarizes the edge sharpness values obtained for all the different polymer films employed. These data prove that the etching resolution is highest for 15K PMMA. This result is consistent with etching of PMMA by a high order nonlinear optical process, and with efficient thermal evaporation of the fragments, which are likely small, due to its low molecular weight. The data obtained for 350K PMMA provides evidence in support of this conclusion. The 350K PMMA films were etched with markedly lower resolution than the lower molecular weight PMMA films. This is very likely caused by deposition of insufficient thermal energy into the high molecular weight PMMA films to properly evaporate larger fragments, especially at the edges of etched regions.

Although etching of PBMA is expected to occur by a similarly high order nonlinear process, PBMA was observed to yield relatively lower resolution etching. This observation can again be explained by the involvement of thermal processes (vide supra). Specifically, it is likely that sufficient energy is deposited into the polymer so that even unetched regions are heated above T_g. In this case, polymer flow from unetched into etched regions is the likely cause of reduced resolution. Further evidence for the importance of thermal processes in PBMA etching is also found in the appearance of raised “ridges” near the edges of etched regions. The presence of these ridges is consistent with heating (and melting) of the PBMA outside the irradiated region, due to its very low T_g.

While PS possesses some of the highest T_g values it is also observed to yield relatively lower resolution etching than PMMA. In this case, the resolution is likely limited by the involvement of a somewhat lower order nonlinear optical process. The PTEBS data provides support for this latter conclusion. In fact, PTEBS yields the lowest etching resolution of all of

the polymers investigated. Low resolution arises in this case because PTEBS is etched via a two-photon process. Hence, dramatically reduced "thresholding" occurs in these films. Reduced resolution is not expected to stem from thermal effects in this case as neither melting nor glass transitions have been detected for these materials for temperatures as high as 500°C.

As a result of the above discussion, it may be concluded that 15K PMMA is best suited (of the polymers studied) for use in multiphoton photolithography, from the perspective of etching resolution alone.

3.2.5 Pattern Transfer Using PDMS Soft Lithography

Experiment done by *Dr.Takashi Ito*

Possible applications of the direct-write multiphoton photolithography methods described herein abound. They include patterning of polymer films for use in the etching of semiconductors, creation of liquid-crystal-based diffractive optics[43] and in production of electrochemical microdisk sensing devices.[33] Here, transfer of sub micrometer-scale patterns produced by multiphoton etching into elastomeric polydimethylsiloxane (PDMS) materials is demonstrated. Transfer of such patterns may find uses in the production of embossed elastomeric stamps for microcontact printing[136, 137] or for fabrication of micro- and nanofluidic devices.[45] Previously, micron-scale patterns fabricated in dye-doped PMMA films via laser ablation using green light were transferred into elastomeric PDMS stamps for use in microcontact printing.[34]

Figure 3.7 shows AFM images of (a) a mold fabricated in a 15K PMMA film (~150 nm thick) using multiphoton photolithography and (b) the same pattern transferred from the mold onto a PDMS surface. The particular pattern transferred here has a height of 50 nm, although patterns with larger and smaller topographic features can also readily be transferred. As shown in the cross-sectional profiles, the depressed area of the mold corresponds exactly to the protruding area in the PDMS surface. However, there is a slight reduction in the pattern resolution upon transfer to PDMS, as demonstrated by the slight rounding of the edges apparent in these data. Considering that this lithographic technique can be used to fabricate sub micrometer patterns in polymer films having thicknesses of less than 50 nm, this method would

clearly be useful for fabrication of nanofluidic devices or for making very thin slits for use in the entropic trapping of DNA molecules.[138]

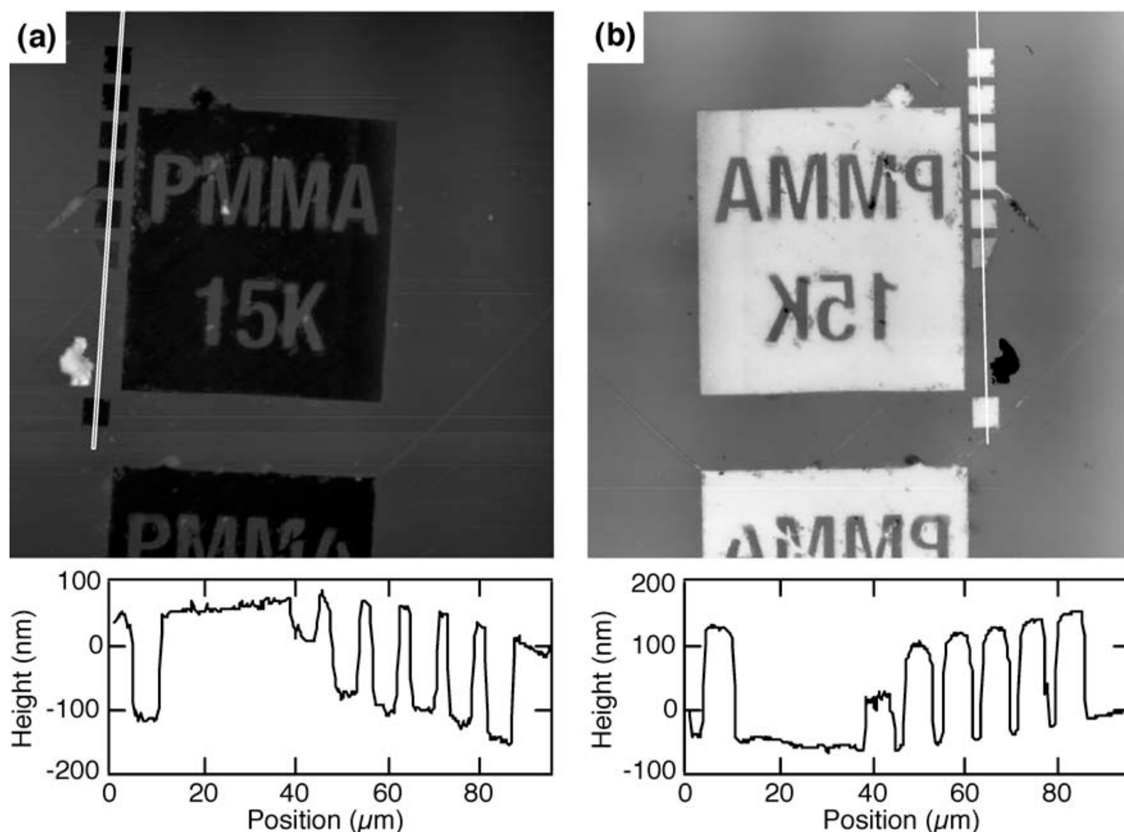

Figure 3.7 AFM topography images of patterns fabricated in (a) 15K PMMA and (b) PDMS. The latter was patterned via soft lithography using the 15K PMMA pattern. Cross-sectional profiles across the AFM images are also shown.

3.3 Summary and Conclusions

Systematic studies of the etching process in direct-write multiphoton induced photolithography have been described in this chapter. These studies were performed for polymers having different chemical structures, different molecular weights and different glass transition temperatures. Studies were also performed for films of different thicknesses. The results prove that multiphoton absorption triggers etching, which then likely proceeds via depolymerization and thermal evaporation of the resulting polymer fragments.[4] It was

conclusively shown that the multiphoton etching process enables the preparation of sub micrometer-scale patterns in thin polymer films. High resolution results from the strong "thresholding" of the etching process for UV-absorbing polymers. Evaporation of the debris makes it possible to obtain patterns without the use of chemical development steps. However, thermal effects (i.e. polymer melting) can also reduce the etching resolution for polymers having low glass transition temperatures. Based on all factors explored and for the polymers investigated, it was concluded that 15K PMMA is best suited for etching by the multiphoton method employed. Pattern transfer via soft lithography was also demonstrated as a means to prepare sub micrometer-scale structures on PDMS from patterns lithographically fabricated in a 15K PMMA film. The direct-write multiphoton etching technique described herein provides a simple means for fabricating chemical sensor arrays, optical devices, and micro- and nanofluidic devices.[45]

Chapter 4 - Bottom-up fabrication and characterization of nanoporous polystyrene-poly (methylmethacrylate) (PS-*b*-PMMA), diblock copolymer thin films

Introduction

This chapter is divided into two sections, the first of which describes the fabrication of thin films of polystyrene-poly (methylmethacrylate) (PS-*b*-PMMA) on silicon substrates having different surface roughness in order to study the effects of roughness and block affinity on the orientation of the cylindrical PMMA domains. These studies were conducted to optimize the conditions, such as film thickness and annealing, for the formation of either the vertical or the horizontal orientation of the PMMA domains in thin films of PS-*b*-PMMA on gold and silicon substrates. The films studied in the first section were not etched via UV/acetic acid treatment. The second section describes in detail the surface chemical characterization of UV/acetic acid etched nanoporous films of *horizontally* aligned PS-*b*-PMMA on silicon substrates, to identify the functional groups formed as a result of UV modification.

4.1 Effects of substrate roughness on the orientation of cylindrical domains in thin films of a polystyrene-poly (methylmethacrylate) diblock copolymer

Helene C. Maire, Shaida Ibrahim, Yongxin Li and Takashi Ito

Reproduced in part with permission from *Polymer*, **2009**, *50*, 2273-2280. Copyright 2009 Elsevier

Introduction

Block copolymers (BCPs)[2, 73-75] containing self-organized nanoscale domains have recently been employed to fabricate masks for lithography,[69] templates for metal or silica nanowire synthesis,[97, 101] templates for nanoparticle deposition,[81, 82] and filtration membranes for viruses.[78, 99] These applications require that the nanoporous templates consist of well ordered vertical orientation of cylindrical domains of the minor component. Indeed, a few applications such as templates for nanoparticle deposition require long range horizontal orientation of domains. Furthermore, characterization of the surface chemical properties of the nanoscale domains of the etched and unetched phases, using scanning force techniques, require that the minor phase is oriented horizontally to the surface. In view of this, optimizing the conditions required for obtaining the desired domain alignment is imperative. Whereas the thickness and domain diameter of PS-*b*-PMMA films can be controlled by the usual parameters of spin speed/solution concentration and molecular weight respectively, [2, 73-75] it is often challenging to control domain alignment. In a BCP film supported by a substrate, the orientation of cylindrical domains is strongly affected by interactions at the BCP–substrate interface and at the free surface of the BCP film. Preferential wetting of one fragment at an interface leads to horizontal domain orientation. To align cylindrical domains vertically to an underlying substrate, the substrate surface has often been chemically tailored to balance the affinities of the BCP fragments.[139, 140] For example, such neutralized surfaces for PS-*b*-PMMA were obtained on hydrogen-terminated Si,[141] on substrates modified with organosilane self-assembled monolayers,[85] and on substrates covalently modified with a brush layer of a PS-PMMA random copolymer having an appropriate volume fraction.[86, 139] In addition to controlling the surface affinity of the underlying substrates,

several approaches have been simultaneously employed to improve the vertical alignment of cylindrical PMMA domains in a PS-*b*-PMMA film, including optimization of film thickness,[87, 142] addition of PMMA homopolymers,[89] control of solvent-evaporation conditions,[88] and electric field application during annealing.[91, 97, 110]

Recently, Sivaniah and coworkers experimentally demonstrated that the roughness of a substrate surface induced the vertical alignment of lamellar PMMA domains in thin films of symmetric PS-*b*-PMMA.[90, 143, 144] The domain orientation was influenced by the lateral periodicity and vertical amplitude of the surface corrugations of an underlying substrate as well as the periodicity of the BCP domains (L_0). The roughness-induced vertical alignment of BCP domains was theoretically explained using a model based on the distortion of aligned domain structures by the rough surface.[145-147] The roughness-induced domain alignment provides a simple means for preparing thin PS-*b*-PMMA films containing vertically-aligned PMMA domains, because it does not require the chemical neutralization of the substrate surface.[90, 143]

In this work, thin films of asymmetric PS-*b*-PMMA with controlled thicknesses (20 ~ 200 nm) were prepared on gold and oxide-coated Si substrates having different surface roughness. The orientation of cylindrical domains at the free surface of PS-*b*-PMMA films having different thicknesses and annealed under different conditions was assessed using atomic force microscopy (AFM). The vertical orientation of cylindrical PMMA domains could be obtained on gold substrates covered with nanoscale grains under controlled annealing conditions. In contrast, the cylindrical domains were oriented horizontally on oxide-coated Si substrates regardless of substrate roughness and the annealing conditions examined.

4.1.1 Experimental

4.1.1.1. Chemicals and Materials

PS-*b*-PMMA (average molecular weights of PS and PMMA: 39,800 and 17,000, respectively; polydispersity: 1.06) was purchased from Polymer Source and used as received. Toluene (Fischer Chemical) and HF (Acros Organics) were used without further purification. Planar Si (100) wafers (p-type) were purchased from University Wafer (South Boston, MA). Gold-coated Si wafers (Au/Si), which were prepared via sputtering 10-nm Ti followed by 200-

nm Au onto Si (100) wafers, were purchased from LGA Thin Films (Foster City, CA). Gold-coated glass slides (Au/glass), which were prepared by electron-beam deposition of 100-nm Au onto aluminosilicate glass microscope slides with a thin Ti adhesion layer, were purchased from Platypus Technologies (Madison, WI).

4.1.1.2. Substrate preparation

All Si and Au substrates (ca. 1 x 1 cm^2) were sonicated in ethanol and then cleaned using a Novascan PSD-UVT UV-Ozone system in air for 30 min. Roughened oxide-coated Si substrates were prepared by immersing the cleaned Si substrates in a 2% w/w ammonium fluoride solution[148] for 20 mins, with sonication for the first 10 mins. The roughened Si substrates were re-oxidized in a UV-Ozone system for 30 min in air.

4.1.1.3. Preparation of PS-b-PMMA thin films

A thin film of PS-*b*-PMMA was prepared on a substrate via spin-coating (2000 rpm, 30 s) from its toluene solution. The thickness of a polymer film was controlled by varying the concentration of the toluene solution in the range from 0.5 to 3% (wt/wt). The polymer-coated substrates were annealed in an Isotemp vacuum oven Model 280a at 170 or 190 ^{o}C in vacuum (0.3 Torr) for 60 ~ 210 hours to allow the formation of cylindrical PMMA domains in the film.

4.1.1.4. Characterization of substrates and PS-b-PMMA films

Water contact angles (θ^{water}) were measured to assess the cleanness of a substrate prior to the polymer film deposition. A water droplet (2 μL) was deposited onto a substrate surface, and the angles at the two opposite water–substrate interfaces were measured within 30 s after depositing the drop.[149] The thickness of an annealed PS-*b*-PMMA thin film (t) was measured using a J. A. Woollam alpha-SE spectroscopic ellipsometer. AFM images of sample surfaces were measured by Tapping-mode imaging in air, using a Digital Instruments Multimode AFM with Nanoscope IIIa electronics. Tapping mode AFM probes from Applied Nanostructures (cantilever length: 125 μm; force constant: 40 N/m; resonance frequency: 300 kHz) were used. The values and errors reported here are the averages and 90% confidence limits, respectively, obtained from multiple measurements on multiple samples.

4.1.2 Results and Discussion

4.1.2.1. Surface roughness and cleanness of planar substrates

In this study, four types of planar substrates were employed as supports for PS-*b*-PMMA films (Figure 4.1): Au substrates prepared on Si wafer via sputtering (Au/Si; Figure 4.1(a)), Au substrates prepared on aluminosilicate glass via electron-beam deposition (Au/glass; Figure 4.1(b)), smooth oxide-coated Si substrates (s-SiO_2/Si; Figure 4.1(c)) and roughened oxide-coated Si substrates (r-SiO_2/Si; Figure 4.1(d)). Table 4.1 summarizes the root-mean-square (RMS) vertical displacement (R), average grain diameter (d_g) and water contact angle (θ^{water}) of these substrates. s-SiO_2/Si was very smooth, whereas the other substrates showed nanoscale grains on their surfaces. In addition, the grain size and the roughness amplitude were largely different between Au/Si and Au/glass. The gold and Si substrates with different roughness allowed us to study the influences of substrate surface roughness on domain orientation in PS-*b*-PMMA films. The θ^{water} values of the gold surfaces were similar to those reported previously,[150] and the very low θ^{water} values (≈ 10°) of the SiO_2/Si surfaces indicated the presence of thick oxide layers.[151]

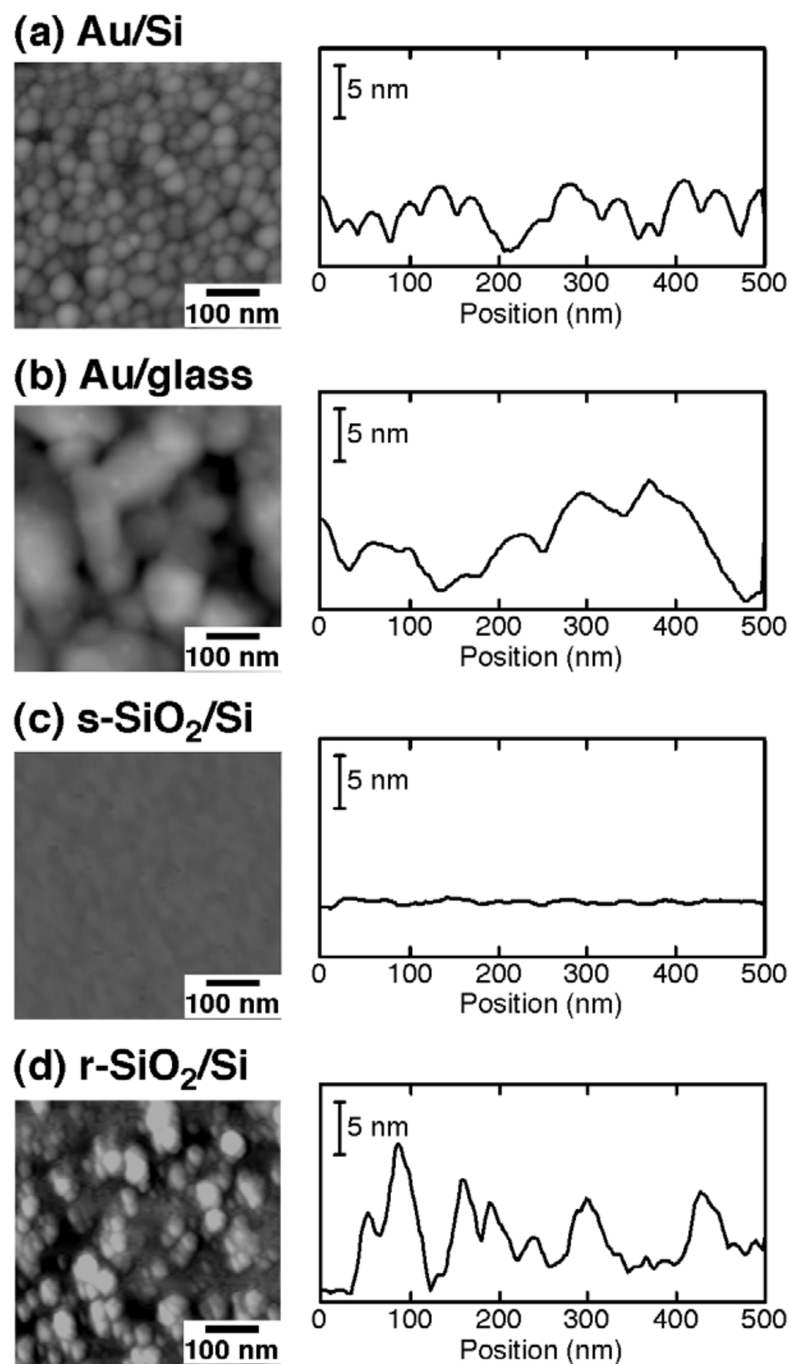

Figure 4.1 AFM images (500 x 500 nm^2) of the cleaned surfaces of (a) Au/Si, (b) Au/glass, (c) s-SiO_2/Si and (d) r-SiO_2/Si. A typical cross-sectional profile of each sample surface is also given. Copyright 2009 Elsevier.

Table 4.1 Surface Root-Mean-Square Roughness (*R*), Grain Diameter on the Surface (d_g) and Water Contact Angle (θ^{water}) of the Substrate Surfaces Used in this Study.

Substrate	*R* (nm)[a)]	d_g (nm)[b)]	θ^{water} (°)[c)]
s-SiO_2/Si	0.2 ± 0.0	–[d)]	9 ± 2
r-SiO_2/Si	1.8 ± 0.5	40 ± 5[)]	9 ± 1
Au/Si	1.4 ± 0.2	36 ± 5	43 ± 1
Au/glass	3.1 ± 0.4	132 ± 13	33 ± 2

[a)] Average and 90% confidence limit of the root-mean-square (RMS) vertical displacement of at least three separate samples. [b)] The average and 90% confidence limit of the diameters of surface grains obtained from line profiles of AFM images. [c)] Average and 90% confidence limit, determined from at least three separate samples. [d)] The surfaces were too smooth to recognize the grains in the line profiles of AFM images. **Copyright 2009 Elsevier**.

4.1.2.2. Effects of PS-b-PMMA film thickness on PMMA domain orientation

Since the PMMA volume fraction of the PS-*b*-PMMA employed here was 0.3, annealed PS-*b*-PMMA films contain self-assembled cylindrical domains of the minor PMMA fragments. Figure 4.2 shows Tapping-mode AFM images of PS-*b*-PMMA thin films having different thicknesses on (a) Au/Si, (b) Au/glass, (c) s-SiO_2/Si and (d) r-SiO_2/Si that were annealed at 170 °C for 60 hours in vacuum. The domain periodicity (L_0)[73] of the PS-*b*-PMMA employed was ca. 35 nm. Samples were classified based on the ellipsometric thickness of the PS-*b*-PMMA films (t): (1) t is slightly smaller than the domain periodicity (t = 17 ~ 24 nm; left), (2) similar to L_0 (t = 32 ~ 42 nm; center), and (3) much larger than L_0 (t = 120 ~ 177 nm; right). These images clearly show that the surface features of PS-*b*-PMMA films were strongly affected by film thickness and underlying substrate.

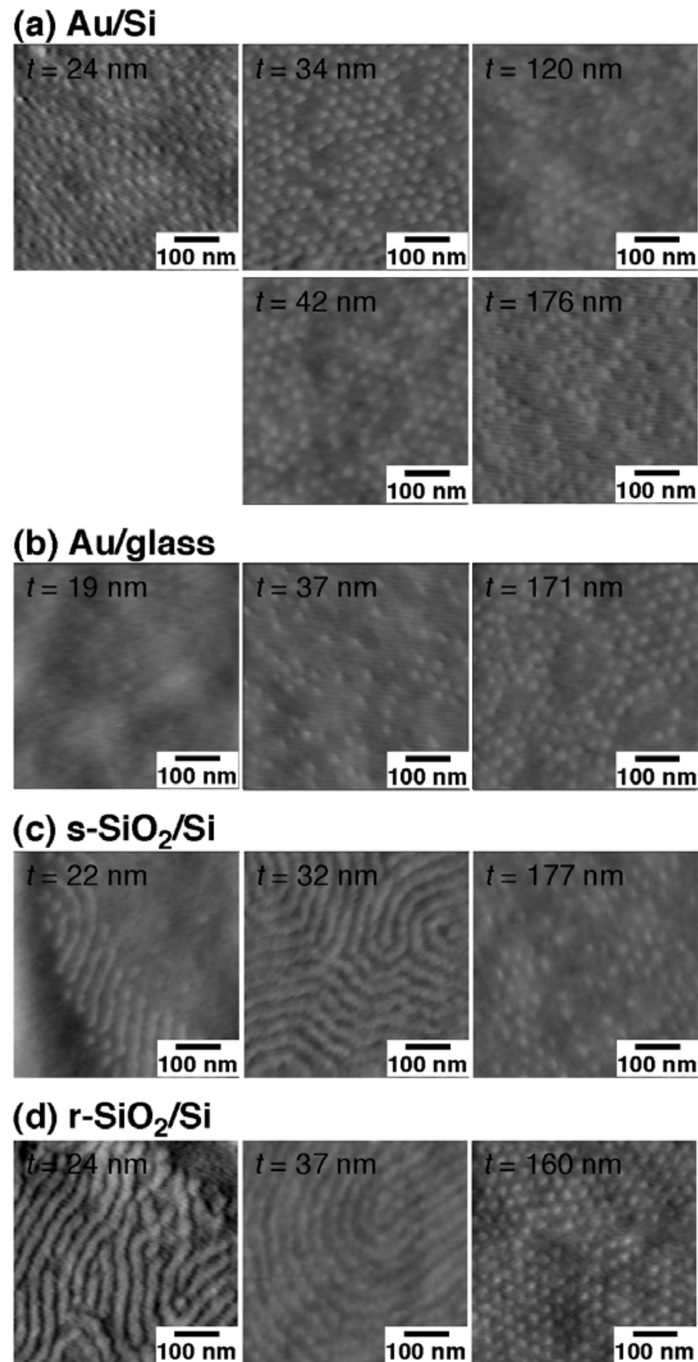

Figure 4.2 AFM images (500 x 500 nm^2; $\Delta z = 20$ nm)) of PS-*b*-PMMA film surfaces having different thicknesses (*t*) on (a) Au/Si, (b) Au/glass, (c) s-SiO_2/Si and (d) r-SiO_2/Si. The ellipsometric thickness of each film is included in each image. Left: $t < L_0$; center: $t \approx L_0$; right: $t >> L_0$. All the PS-*b*-PMMA films were annealed at 160 °C for 60 hours in vacuum. Copyright 2009 Elsevier

When t was much larger than L_0 (Figure 4.2, right row), circular dots indicating cylindrical PMMA domains oriented vertically to the film surface were observed on the four types of substrates. The vertical domain orientation at the free surface probably reflected the nearly balanced affinity of the two polymer fragments at the polymer–vacuum interface, as suggested by the similar surface tension values of PS and PMMA at 150 °C (31.4 and 31.2 mN/m, respectively).[152] The density of the vertical domains exposed to the surface was similar on the four substrates, but was slightly smaller than the maximum density of the hexagonal domains calculated from L_0 (ca. 900 domains/μm^2). The smaller domain density may reflect the slightly higher affinity of PS to vacuum.[153] These results indicate that the PS-*b*-PMMA films of $t >> L_0$ are not suitable for demonstrating the influence of substrate properties on the orientation of cylindrical PMMA domains.

In contrast, AFM images of PS-*b*-PMMA films at $t < L_0$ and $t \approx L_0$ were different according to the substrates, suggesting that the domain orientation at the free surface of these thin films mainly reflected interactions at the polymer-substrate interface.

On Au/Si, vertical domains without any island structures were observed at $t < L_0$ and $t \approx L_0$ (Figure 4.2(a), left and center), suggesting that the cylindrical PMMA domains on Au/Si were oriented vertically to the polymer–vacuum interface. Circular dots corresponding to vertical PMMA domains were observed at $t \approx L_0$ on Au/glass (Figure 4.2(b), center). However, these circular dots distributed non-uniformly and at a density lower than half of that on Au/Si (Figure 4.2(a), center). These observations suggest that the roughness of these gold substrates inhibit the horizontal orientation of the cylindrical domains and thus give vertically oriented domains under the annealing conditions examined. Although it has been reported that gold surface is preferentially wetted by PS fragments,[154, 155] the difference in the affinity of PS and PMMA to the gold surface may not be so large.[90] An AFM image at $t < L_0$ on Au/glass (Figure 4.2(b), left) did not show the domain morphology of PS-*b*-PMMA and instead showed the contour reflecting the surface structure of the substrate (Figure 4.1(b)). The different domain morphologies on Au/Si and Au/glass probably reflected the kinetics of domain formation and orientation influenced by the substrate roughness (see 4.1.2.3).[143]

On the other hand, PMMA domains were horizontally oriented at $t \leq L_0$ on s-SiO_2/Si (Figure 4.2(c)) and r-SiO_2/Si (Figure 4.2(d)). The horizontal domains formed island structures in

PS-*b*-PMMA films at $t < L_0$ (Figure 4.2(c) and (d), left) and covered the whole surface at $t \approx L_0$ (Figure 4.2(c) and (d), center).[73, 82, 156] These observations are consistent with the commensurability effects.[73, 139] These results indicate that the roughness did not significantly affect the domain orientation on SiO_2/Si substrates. The negligible effect of the surface roughness on oxide-coated Si surface is probably due to the much higher affinity of the PMMA fragments to the underlying oxidized Si surface.[73] This is probably because of the hydrogen bond interactions between surface Si-OH groups and the ester moieties of PMMA.[156, 157]

In summary, under the annealing conditions employed here, the domain orientation at the free surface of a PS-*b*-PMMA film at $t \leq L_0$ reflected interactions between the polymer fragments and substrate surface, whereas that at $t >> L_0$ resulted from the balanced affinity of the polymer fragments at the polymer–vacuum interface. These results mean that the domain orientations, observed with AFM, were competitively determined by interfacial interactions at the polymer-vacuum and polymer-substrate interfaces, giving the thickness-dependent domain orientation. These conclusions could be obtained by systematically investigating domain orientation at the free film surface by varying film thickness on the same substrate and by using films of similar thickness on different substrates.

4.1.2.3. Effects of the annealing conditions on PMMA domain orientation in thin PS-b-PMMA films

As shown in Figure 4.2(a) and (b), the substrate roughness induced the vertical orientation of cylindrical PMMA domains on gold. However, the roughness amplitudes of these substrates (Figure 4.1(a) and (b)) were similar to those of substrates that showed metastable perpendicular orientation of lamellar microdomains in films of symmetric PS-*b*-PMMA.[143] On such moderately rough substrates, the perpendicular lamellae obtained after initial annealing changed to parallel lamellae after extended annealing.[143, 158] The domain morphologies of cylinder-forming PS-*b*-PMMA films of $t \approx L_0$ (= 32 ~ 37 nm) on Au/Si and Au/glass were thus investigated upon their annealing at higher temperature (190 °C) for a longer time (100 h, 150 h, 210 h).

Figure 4.3 summarizes AFM images of PS-*b*-PMMA thin films on (a) Au/Si and (b) Au/glass that were annealed under different conditions. PMMA domains at the free surface of a PS-*b*-PMMA film on Au/Si were oriented horizontally after annealing at 190 °C for 150 hours, in contrast to those oriented vertically after annealing at 170 °C for 60 hours (Figure 4.3(a)). The horizontal orientation of PMMA domains was similarly observed after annealing at 190 °C for 100 hours. These observations indicated that the vertical orientation obtained upon annealing at 170 °C would be metastable. The PMMA domains were oriented horizontally to the underlying gold substrate at equilibrium due to the preferential affinity of PS fragments on gold surface.[154, 155]

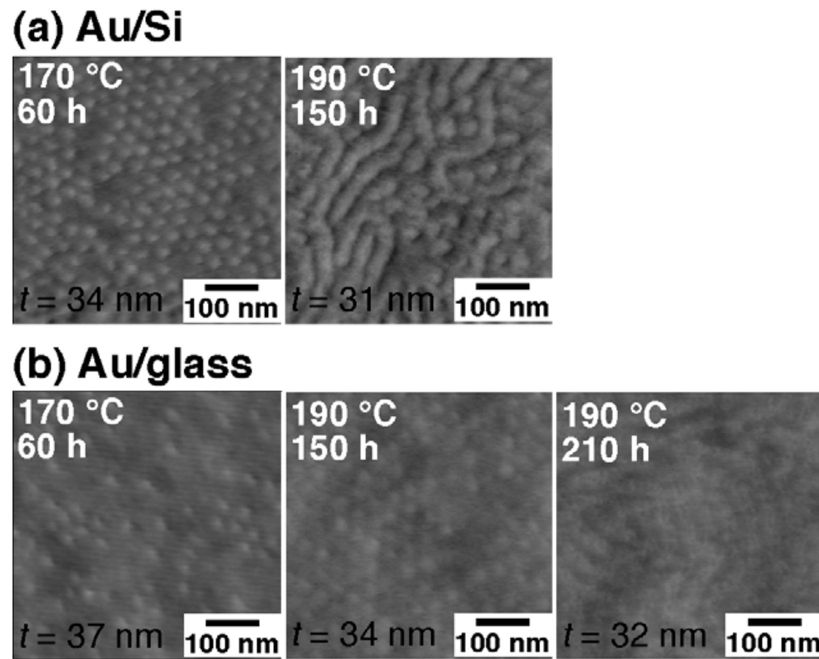

Figure 4.3 AFM images (500 x 500 nm^2; Δz = 20 nm)) of the surface of PS-*b*-PMMA films on (a) Au/Si and (b) Au/glass annealed under different conditions. The ellipsometric thickness of each film, which was close to L_0, is included in each image. The PS-*b*-PMMA films were annealed in vacuum at 160 °C for 60 hours (left; the same images as those shown in Figure 4.2(a) and (b)), at 190 °C for 150 hours (center) and at 190 °C for 210 hours (right). Copyright 2009 Elsevier

On Au/glass, PS-b-PMMA films annealed at 190 °C for 150 hours contained vertical domains at higher density than those at 170 °C for 60 hours (Figure 4.3(b)). However, PMMA domains were oriented horizontally in films annealed at 190 °C for 210 hours (Figure 4.3(b); right), indicating that the vertical orientation was obtained at the metastable state. The slower transition of the domain orientation on Au/glass would be due to its larger roughness amplitude as compared to Au/Si, which was consistent with the trend reported previously on the kinetics of roughness-induced domain orientation of lamella-forming PS-*b*-PMMA films.[143]

4.1.3 Summary and Conclusions

This section described the effects of substrate properties and film thickness on the orientation of cylindrical PMMA domains in thin films of PS-*b*-PMMA. The nanoscale roughness of gold substrates induced the metastable vertical orientation of PMMA domains at the polymer-substrate interface without neutralizing the block affinity of the substrate. The metastable vertical domain orientation was previously reported for lamella-forming, symmetric PS-*b*-PMMA films on indium tin oxide and polyimide substrates.[90, 143, 146, 147] In contrast, regardless of their roughness, vertically oriented microdomains were not observed on oxide-coated Si substrates under the annealing conditions examined, probably because of the high affinity of PMMA fragments to the surface. However, more systematic investigations on the effects of substrate roughness, substrate block affinity and annealing conditions on the domain orientation would be necessary to fully understand the microdomain orientation in cylinder-forming PS-*b*-PMMA films on rough surfaces.

4.2 Surface Chemical Properties of Nanoscale Domains on UV-Treated Polystyrene-Poly (methylmethacrylate) Diblock Copolymer Thin Films

Shaida Ibrahim and Takashi Ito

Reproduced with permission from *Langmuir*, **2010**, *26*, 2119-2123. Copyright 2009 American Chemical Society

Introduction

This section describes the surface chemical properties of ca. 20-nm wide domains on a UV-treated thin film of a polystyrene-poly (methylmethacrylate) diblock copolymer (PS-*b*-PMMA). Horizontally-oriented PMMA domains were formed on a thin film of PS-*b*-PMMA (71,000 as the molecular weight; 0.3 as the PMMA volume fraction) on a SiO_2-coated Si substrate, and etched by UV irradiation and subsequent acetic acid (AcOH) treatment. The surface charge and hydrophilicity of the resulting nanoscale trenches (etched PMMA domains) and ridges (PS domains) were investigated via three different approaches based on scanning force microscopy (SFM): chemical force pH titration, friction force imaging with chemically modified tips, and observation of ferritin adsorption with tapping-mode atomic force microscopy (TM-AFM).

Microdomains of minor components in a BCP are selectively etched to obtain nanoscale structures that can be used as masks for nanolithography,[69] as templates for nanomaterial synthesis,[97] as substrates for controlled deposition of nanomaterials,[81-83, 98] and as chemical separation membranes.[78-80, 99, 159] For templating and separation applications, it is important to understand and control the surface chemical properties of BCP-derived microstructures that determine chemical interactions with nanomaterials and biomolecules of interest. Previously, BCPs that offered known surface functionalities upon the formation of nanoporous structures were designed and synthesized.[92-94, 160] Chemical functionalization of the nanopore surface was monitored by NMR measurements of the dissolved polymer solution.[93, 94] Cyclic voltammetry (CV) was previously employed to investigate the surface chemistry of cylindrical nanopores in thin films derived from PS-*b*-PMMA.[76, 79, 108] However, CV cannot be used to assess the surface

chemistry of the unetched PS matrix, though the surface properties of both the domains may need to be controlled for efficient templating and chemical separation applications.

A PS-*b*-PMMA film, with horizontally-oriented cylindrical PMMA domains on its surface, was employed in this experiment. The use of horizontally oriented domains permitted the direct comparison of the surface chemical properties of the two nanoscale domains using SFM-based techniques. Here, three different SFM-based approaches were examined to investigate the surface charge and hydrophilicity of these domains. First, chemical force pH titration,[161, 162]which has been employed to assess the surface functionality of polymers,[122, 163-165] was examined to obtain information on surface functional groups on the domains. Next, friction force images of the film surface with chemically modified tips[107, 122, 125, 162, 166-168] were measured in *n*-dodecane to compare the chemical properties of the domains that reflected the tip-surface hydrogen bonding and dispersion forces. Finally, ferritin adsorption from an aqueous buffered solution onto the two distinct domains, which would be determined by electrostatic and hydrophobic interactions with the domains, was investigated with TM-AFM. An in-depth knowledge of the surface properties of the two distinct domains will make it possible to control chemical interactions at these surfaces, and thus to improve the efficiency in templating applications and chemical separations.

4.2.1 Experimental

4.2.1.1 Chemicals and Materials

PS-*b*-PMMA (71K PS-*b*-PMMA: Mn = 50,000 g/mol for PS and 21,000 g/mol for PMMA, M_w/M_n = 1.08) and polystyrene (PS; M_w = 119,600 g/mol) were purchased from Polymer Source and used as received. 11-mercaptoundecanoic acid (Aldrich), 11-mercapto-1-undecanol (Aldrich), 1-dodecanethiol (Acros Organics), n-dodecane (Alfa Aesar), potassium dihydrogen phosphate (Fisher Chemical), potassium hydrogen phosphate (Fisher Chemical), potassium hydroxide (Fisher Chemical), phosphoric acid (85%, Fisher Chemical), and ferritin (from equine spleen, Sigma) were used as received. All aqueous solutions were prepared with water having a resistivity of 18 MΩ or higher (Barnstead Nanopure Systems). Si (100) wafers (p-type) were purchased from University Wafer.

4.2.1.2 Preparation of UV/AcOH-Treated PS-b-PMMA Films

Si substrates (15 mm x 15 mm) were cleaned in a Novascan PSD-UVT UV-ozone system for 30 mins prior to use. A thin PS-*b*-PMMA film was prepared by spin-coating its toluene solution (0.75 % w/w) on a silicon substrate, and annealed at 170°C in vacuum for 60 h to form horizontally oriented PMMA domains on the film.[109] The PMMA domains were etched by UV irradiation for 40 min under an Ar atmosphere and subsequent rinsing with glacial acetic acid.[108, 110] The thickness of the films prior to the etching was in the range of 30 – 40 nm, which was measured using a J. A. Woollam alpha-SE spectroscopic ellipsometer. As control experiments, 35 nm thick PS homopolymer films were prepared to investigate the effects of the UV/AcOH treatment.

4.2.1.3 Contact Angle Measurements

Contact angles were measured by depositing 2 μL of a 1 mM phosphate solution (pH 3.0 – 10.3) onto a UV/AcOH-treated PS-*b*-PMMA film using a PG-1 pocket contact angle goniometer.[169] The angles formed at the two opposite liquid-substrate interfaces were measured within 30 sec of depositing the drop. Contact angles of water were also measured on a PS-*b*-PMMA film before and after UV/AcOH treatment. The contact angle data reported are the averages and standard deviations of more than four measurements at different positions on a sample.

4.2.1.4 Chemical Force Microscopy Measurements

Chemical force pH titration and friction force imaging with gold-coated tips modified with thiolate self-assembled monolayers (SAMs) were carried out using a Picoscan SPM (Molecular Imaging) within a liquid cell. Gold-coated tips (Budget Sensors; cantilever length, 450 μm; force constant, 0.2 N/m; resonant frequency, 13 kHz) were first rinsed with ethanol and then cleaned in a Novascan PSD-UVT UV-ozone system for 30 min. The cleaned tips were immersed in an ethanol solution of an organic mercaptan (1 – 2 mM) for at least 24 h, rinsed with ethanol, and dried in air. The spring constants of the chemically-modified gold tips were determined using software contained within the Digital Instruments multimode microscope (Nanoscope IIIa electronics) based upon the thermal oscillations of the cantilever.

Chemical force pH titration data were obtained using tips modified with COOH-terminated SAMs (COOH-terminated tips) in 1 mM phosphate solutions (pH 3.0 – 10.3). The tip and sample were equilibrated for 10 min at each pH before the measurement. The SPS mode was used to obtain 64 force-distance curves while simultaneously acquiring a topographic image (scan speed: 3.5 Hz) over a 1 x 1 μm^2 area of a sample. At least two different areas on a sample were measured using a single tip to generate a total of 128 force-distance curves. The adhesion force was measured as the deflection of the cantilever at pull-off, from force versus cantilever displacement curves. The spring constant and the slope of the retract region (deflection sensitivity) were used to convert the cantilever deflection, in volts, into an adhesion force. Tip approach-retract speed used for measuring a force-distance curve was 160 nm/s: Adhesion force on a UV/AcOH-treated PS-b-PMMA sample was similar over the speed range of 53 – 160 nm/s whereas faster speeds gave larger adhesion force. The data reported in this paper were obtained using one COOH-terminated tip, and similar trends were observed with two other COOH-terminated tips.

Friction force imaging was performed in the contact mode within a liquid cell using tips modified with CH_3- or OH-terminated SAMs (CH_3- and OH-terminated tips, respectively). Topography and friction images (scan rate: 3.5 Hz; applied load: 10 nN) were simultaneously obtained in *n*-dodecane with the scan direction set perpendicular to the long axis of the cantilever. The friction signal (in the voltage scale) represented the torsional deflection of the cantilever, determined as the difference in laser intensity irradiated between left and right halves of the detector. The friction signal was not converted to friction force because the torsional spring constant of the cantilever was not measured.

4.2.1.5. Observation of Ferritin Adsorbed on UV/AcOH-Treated PS-b-PMMA Films

A UV/AcOH-treated PS-*b*-PMMA surface was covered with 100 μL of a ferritin solution (1 mg/ml in a 1mM phosphate buffer at pH 6.5) for 30 sec. The surface was then rinsed with phosphate buffer followed by water, and dried prior to imaging. TM-AFM images of the sample were obtained in air using a Digital Instruments Multimode AFM with Nanoscope IIIa electronics. TM-AFM probes from Applied Nanostructures (cantilever length, 125 μm; force constant, 40 N/m; resonant frequency, 300 kHz) were used.

4.2.2 Results and Discussion

4.2.2.1. Contact Angle Measurements

Prior to SPM studies, contact angles of PS-*b*-PMMA films were measured to investigate the influence of the UV/AcOH treatment. The water contact angle (θ^{water}) on a PS-*b*-PMMA film before UV/AcOH treatment was (81 ± 2)°. This θ^{water} value was between those of PS (ca. 90°) and PMMA (ca. 70°)[139] homopolymer surfaces reported previously, suggesting the presence of PS and PMMA domains exposed to the film surface. After the UV/AcOH treatment, the θ^{water} value decreased to (42 ± 2)°, suggesting the presence of hydrophilic functional groups on the film.

To investigate the nature of these hydrophilic functional groups on UV/AcOH-treated PS-*b*-PMMA films, contact angles of aqueous solutions were measured at different pH (Figure 4.4, filled circles). The measured contact angle gradually decreased from pH 4 to 10, which can be explained by the deprotonation of acidic functional groups on the surface at higher pH.[170] The decrease in contact angle over pH 4 – 7 was probably due to the deprotonation of the surface -COOH groups that were previously shown on the etched PMMA domains using CV.[108] The gradual decrease in contact angle at the higher pH (e.g., pH 7 – 10) may reflect the presence of other acidic functional groups such as phenolic -OH groups (pKa ~ 10)[171] on the surface. Indeed, the presence of oxygen-containing functional groups on PS-*b*-PMMA surface irradiated by vacuum ultraviolet light (VUV) was suggested by X-ray photoelectron spectroscopy.[172] On the other hand, the θ^{water} value on PS homopolymer surface decreased from 86° to ca. 50° upon UV/AcOH treatment, indicating the formation of hydrophilic functional groups. However, the contact angle values were similar regardless of solution pH (Figure 4.4, open circles), suggesting that the -COOH groups on the UV/AcOH-treated PS-*b*-PMMA films were mainly present on the etched PMMA domains rather than the PS domains.

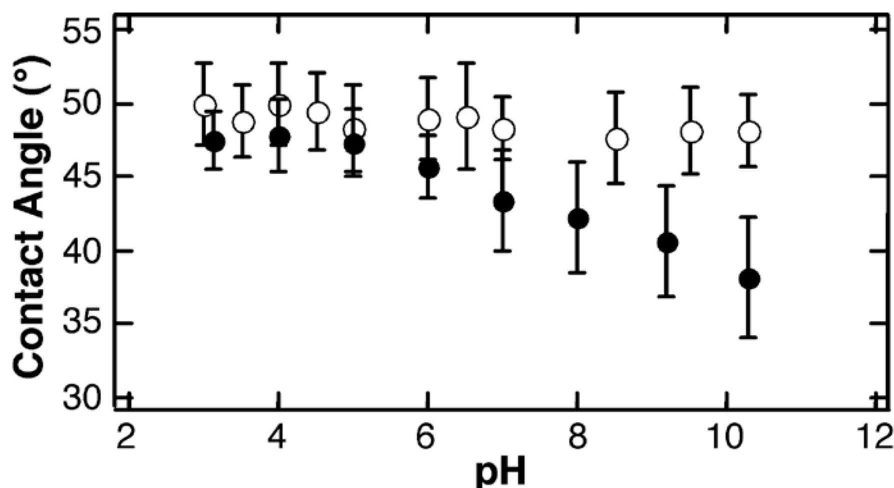

Figure 4.4 Contact angle measured as a function of pH on UV/AcOH-treated PS-*b*-PMMA (filled circles) and PS homopolymer (open circles) films on an oxide-coated Si substrate (30 – 35 nm thick film before UV/AcOH treatment). The measurements were made in aqueous solutions containing 1.0 mM phosphate at room temperature. The plots and error bars indicate the average and standard deviation, respectively, measured on three separate substrates.

4.2.2.2 Chemical Force pH Titration

The contact angle measurements indicated the presence of acidic functional groups on the polymer surface, but could not provide chemical information on the individual nanoscale domains. Two types of nanoscale domains were present on the surface of a UV/AcOH-treated PS-*b*-PMMA film.[82, 83] The left column of Figure 4.5 shows topographic contact-mode AFM images measured using a COOH-terminated tip in aqueous solutions of (a) pH 3.0, (b) pH 4.5 and (c) pH 10.3. These images show horizontally-oriented, ca. 20-nm wide trenches and ca. 25-nm wide ridges, which correspond to the etched PMMA and unetched PS domains, respectively. Importantly, there was no noticeable change in topographic images during the course of the experiment, indicating high stability of the sample and AFM tip.

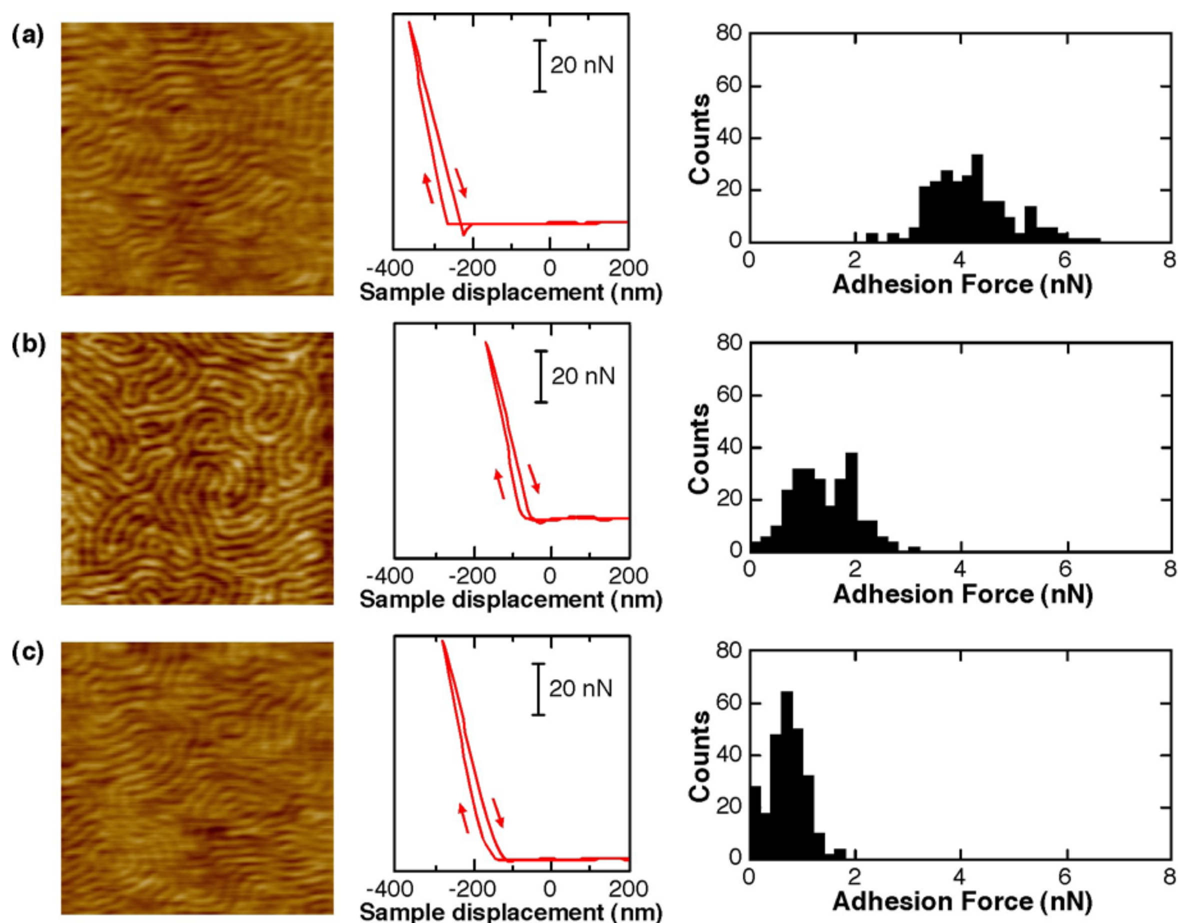

Figure 4.5 Typical AFM images (image size: 1 x 1 μm^2; total gray scale range: 5 nm; scan rate: 3.5 Hz), force-displacement curves and force histograms of adhesion forces obtained with a COOH-terminated gold tip on a UV/AcOH-treated PS-*b*-PMMA film at (a) pH 3.0, (b) 4.5, and (c) 10.3. Measured in aqueous solutions containing 1.0 mM phosphate at room temperature.

The center column of Figure 4.5 shows typical force-distance curves measured between a UV/AcOH-treated PS-*b*-PMMA film and a COOH-terminated tip in aqueous solutions of (a) pH 3.0, (b) pH 4.5 and (c) pH 10.3. At the higher pH, a smaller adhesion force in the retracting trace was observed in addition to a larger repulsive force in an approaching trace. This trend could be clearly seen in the force histograms, the frequency distribution of adhesion forces between the COOH-terminated tip and UV/AcOH-treated PS-*b*-PMMA film, at each pH (Figure 4.5, right column). Figure 4.6 shows the chemical force titration curve summarizing the average and

standard deviation of the adhesion forces measured between a COOH-terminated tip and a UV/AcOH-treated PS-*b*-PMMA film at different pH. Adhesion force decreased from pH 3 to 4.5, and then was similar at higher pH. The smaller adhesion force at higher pH was probably due to electrostatic repulsion between deprotonated -COOH groups on the tip and acidic functional groups (e.g., -COOH groups)[161, 162] on the polymer surface. However, the pH range that showed the decrease in adhesion force was narrower than that shown in the contact angle titration (Figure 4.4). The small change in adhesion force at pH $\geq$ 4.5 may be due to the relatively small ionic screening of the surface negative charge on the tip and substrate at relatively low supporting electrolyte concentration.[123] On the other hand, no clear difference was found in adhesion force on the etched PMMA trenches, PS ridges and the boundaries of the two domains (Figure 4.7). These results indicate that chemical force pH titration could be used to show the presence of acidic functional groups on a UV/AcOH-treated PS-*b*-PMMA surface, but did not permit the comparison of the surface chemical properties of the nanoscale domains.

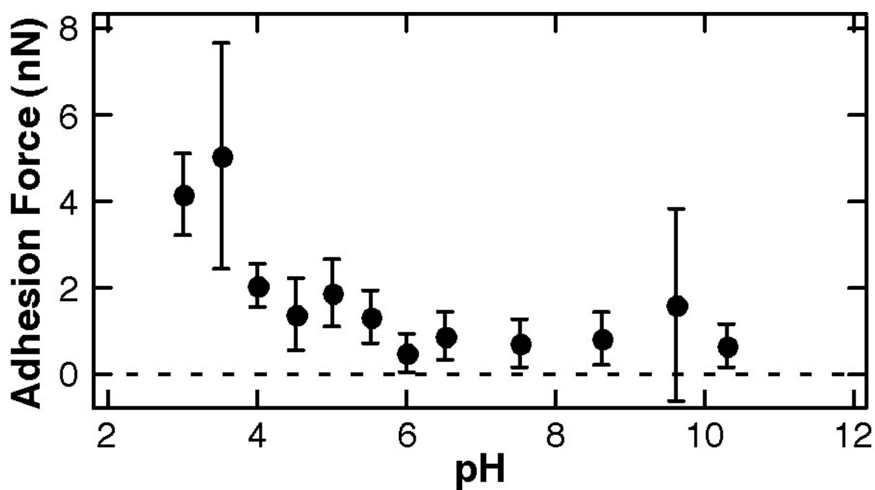

Figure 4.6 Typical pH dependence of adhesion force between a COOH-terminated gold tip and a UV/AcOH-treated PS-*b*-PMMA film. Measured in solutions containing 1 mM phosphate at room temperature. The plots and error bars indicate the average and standard deviation, respectively, of adhesion force from 128 force curves.

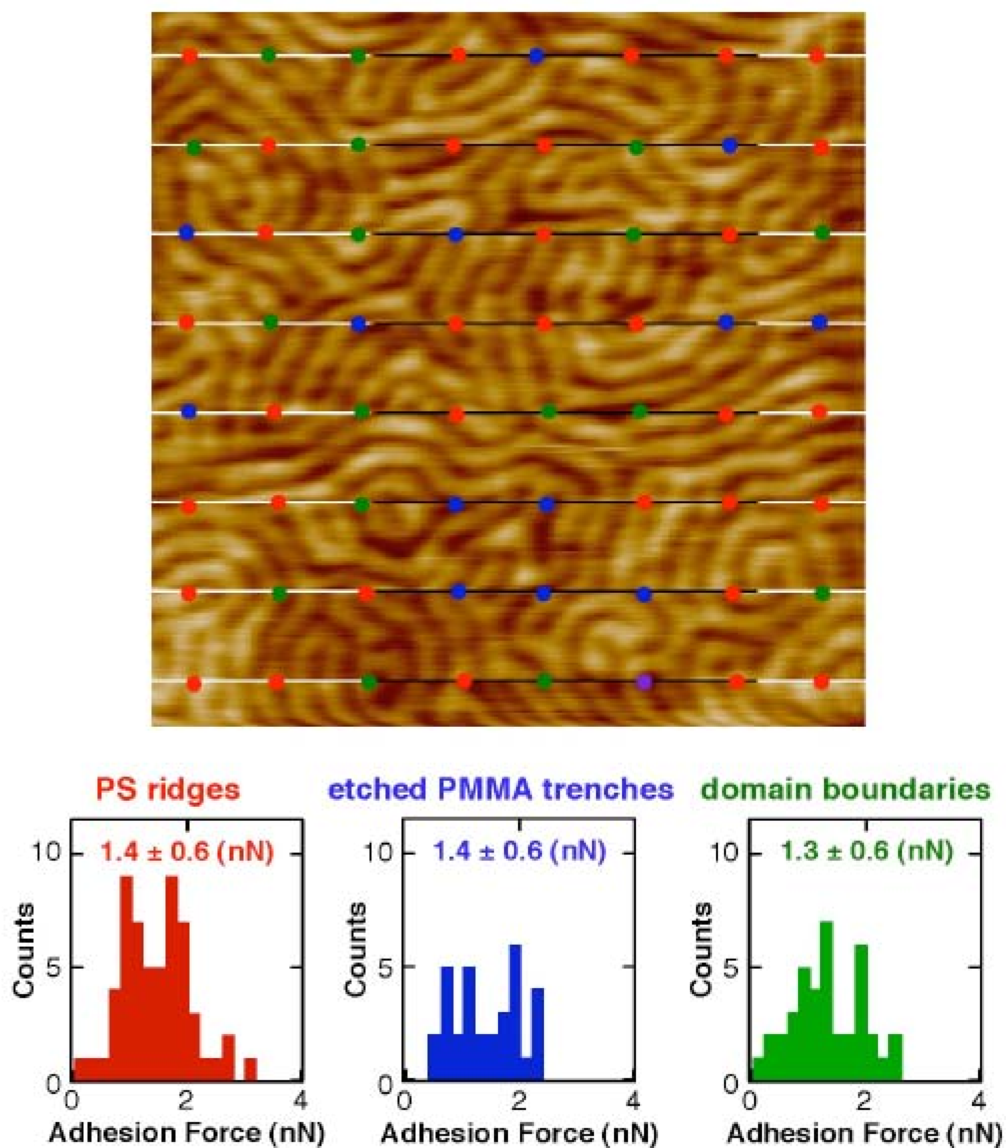

Figure 4.7 AFM image (image size: 1 x 1 μm^2 ; total grey scale range: 5 nm; scan rate: 3.5 Hz) and force histograms of adhesion forces obtained with a COOH-terminated gold tip on a UV/AcOH-treated PS-*b*-PMMA film at pH 4.5. The histograms were obtained based on adhesion forces obtained on the positions indicated by the dots in the AFM image: PS ridges (red), etched PMMA trenches (blue) and domain boundaries (green). Measured in aqueous solutions containing 1.0 mM phosphate at room temperature.

4.2.2.3 Friction Force Imaging of UV/AcOH-Treated PS-b-PMMA Surface Using Chemically Modified AFM Tips

To verify the difference in the hydrophilicity of the two domains, topography and friction force images of a UV/AcOH-treated PS-*b*-PMMA film were simultaneously measured using CH_3- and OH-terminated tips in *n*-dodecane. The use of the nonpolar solvent would enhance hydrogen bonding interactions between polar functional groups on the tip and the surface, facilitating comparison of the hydrophilic nature of the domains.[125, 173] The comparison of the images obtained using the two different tips may make it possible to discuss the difference in chemical properties of the domain surfaces without the influence of the topographical features. Figure 4.8 shows topography and friction images of a UV/AcOH-treated PS-*b*-PMMA film measured using (a) a CH_3- and (b) OH-terminated tips in *n*-dodecane. As with the topography images measured in aqueous solutions (Figure 4.5, left), the topography images in *n*-dodecane showed trenches (etched PMMA domains) and ridges (unetched PS domains) of 20 – 25 nm in width regardless of the tips employed. In contrast, the different tips gave different contrast in the friction images (Figure 4.8, right): CH_3- and OH-terminated tips offered higher friction on the ridges (PS domains) and trenches (etched PMMA domains), respectively. The higher friction signal between the OH-terminated tip and the etched PMMA domains probably reflected the strength of hydrogen bond interactions, suggesting that the density of -COOH groups was higher on the etched PMMA domains than on the PS domains. The CH_3-terminated tips offered a higher friction signal on the PS domains even in the nonpolar environment, which can perhaps be explained by the hydrophobic interactions originating from a water layer on the relatively hydrophilic polymer surface (θ^{water} ~ 42°). Indeed, higher friction signal on a more hydrophobic surface with a CH_3-terminated tip in *n*-hexadecane was reported previously.[173] Hence, the reversal of contrast in friction force images obtained using the OH- and CH_3-terminated tips indicates the higher hydrophilicity of the etched PMMA domains due to the presence of acidic surface functional groups at higher density.

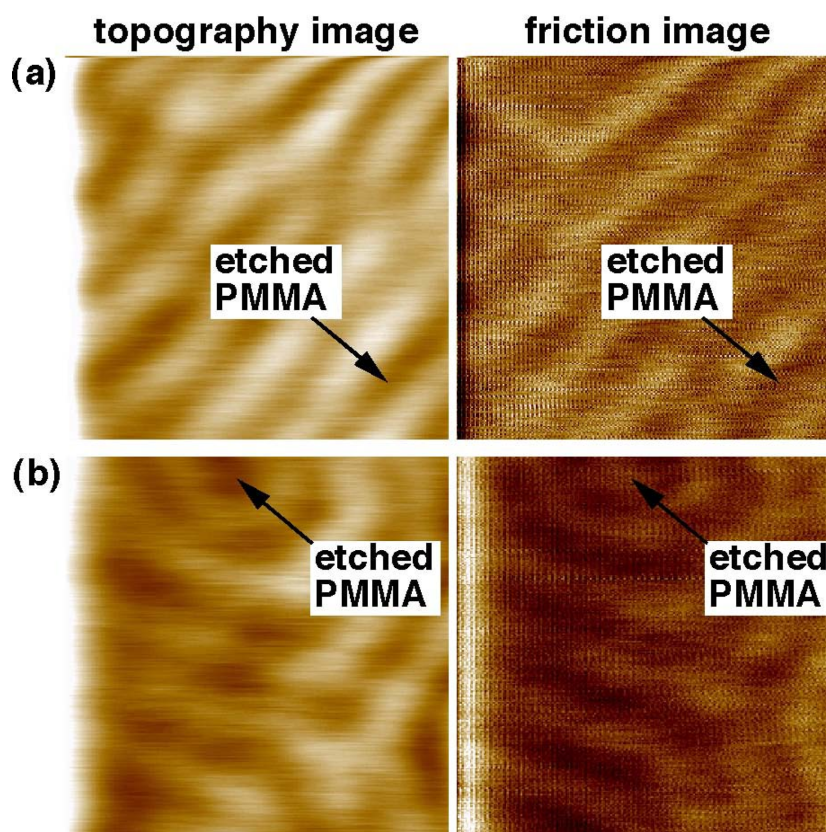

Figure 4.8 Contact mode AFM topography and friction images (250 x 250 nm^2; scan rate: 3.5 Hz) of a UV/AcOH-treated PS-*b*-PMMA film obtained in *n*-dodecane (a) with a CH_3-terminated gold tip and (b) an OH-terminated gold tip. The brighter contrast indicates the higher region in the topography images (total gray scale range: 3 nm) and higher friction in the friction images (total gray scale range: 0.1 V). The applied force was 10 nN, and scan rate was 3.5 Hz.

4.2.2.4 Ferritin Adsorption onto UV/AcOH-Treated PS-b-PMMA Films Using TM-AFM

Furthermore, the surface properties of the nanoscale trenches and ridges on a UV/AcOH-treated PS-*b*-PMMA film were investigated based on the adsorption behavior of ferritin, a globular protein with a diameter of 12 nm.[174] Figure 4.9 shows a typical TM-AFM image of a

UV/AcOH-treated PS-*b*-PMMA film upon deposition of ferritin from its buffer solution of pH 6.5. Ferritin molecules were observed as bright dots of 12 – 17 nm in diameter and 6 – 10 nm in height, in addition to their larger aggregates. Interestingly, the majority of ferritin (81 ± 5 %, determined from three separate samples) adsorbed onto the ridges (i.e., PS domains). The preferential adsorption of ferritin onto the PS domains could be explained on the basis of the larger electrostatic repulsion by the deprotonated acidic groups within the etched PMMA domains and also the more hydrophobic nature of the PS domains. The involvement of the electrostatic repulsion can be understood by considering that ferritin (pI = 4 ~ 5)[174] and etched PMMA domains[108] are negatively charged in an aqueous solution of pH 6.5. Because of its higher acidic functional group density, the etched PMMA domains repelled ferritin more efficiently than the PS domains. In addition, the hydrophobic properties of the PS domains facilitated the ferritin adsorption, as with the selective adsorption of immunoglobulin G and protein G onto PS domains of an untreated PS-b-PMMA film.[175, 176] The deposition selectivity of ferritin was opposite to those of oleic acid-capped FePt nanoparticles[82, 83] and poly(ethylene oxide)-coated CdSe nanorods[98] on VUV-treated PS-b-PMMA films. The nanoparticles and nanorods were confined within the trenches on the basis of the physical process involving solution flow that removed the excess nanomaterial solution from the PS ridges, rather than chemical interactions.[83]

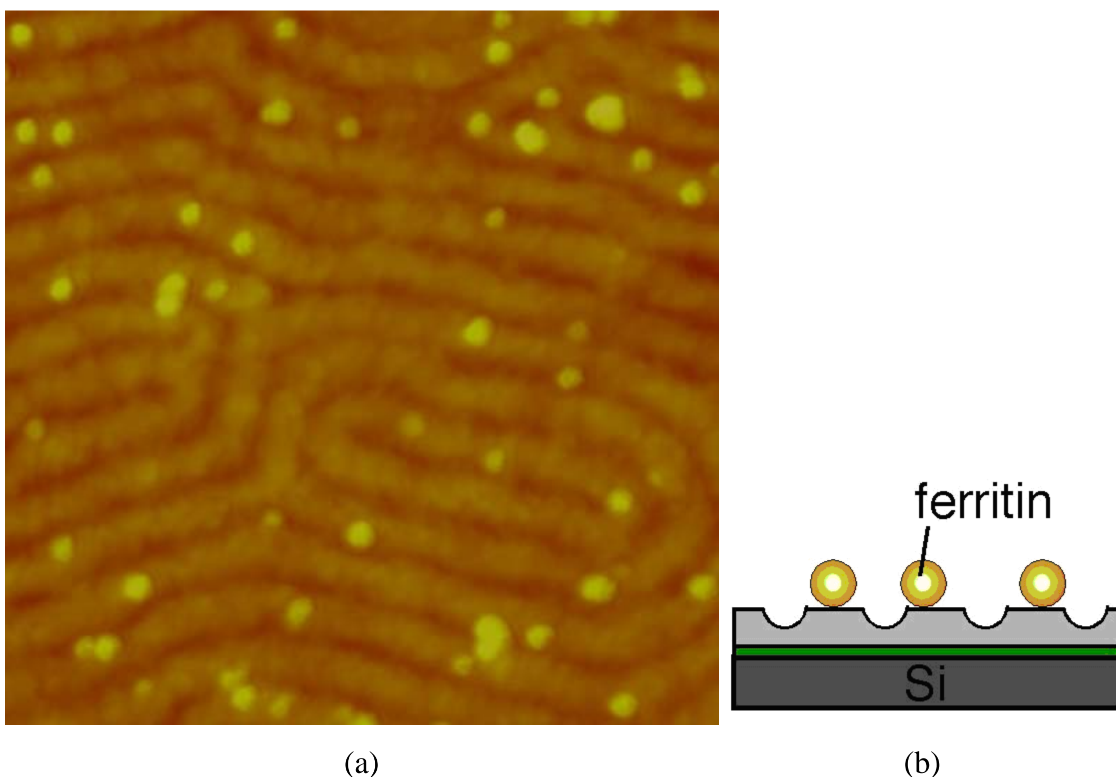

(a) (b)

Figure 4.9 (a) Typical TM-AFM topography image (500 x 500 nm^2, total gray scale range: 50 nm; scan rate: 2 Hz) of a UV/AcOH-treated PS-*b*-PMMA film upon deposition of ferritin molecules. A ferritin solution (1mg/ml) in a 1 mM phosphate buffer of pH 6.5 was cast on the film for 30 sec for the deposition of ferritin. After rinsing with water, the sample was dried and imaged using TM-AFM in air. (b) Schematic diagram of ferritin adsorption on the PS ridges.

4.2.3 Summary and Conclusions

This chapter described the difference in surface charge and hydrophilicity of the two distinct nanoscale domains of UV/AcOH-treated PS-*b*-PMMA films using three different SFM-based approaches. The PS ridges were more hydrophobic and less negatively-charged than the trenches formed by the etching of the cylindrical PMMA domains. The hydrophilic properties of the etched PMMA domains probably originated from the higher surface density of acidic functional groups such as -COOH groups, as suggested by the chemical force titration and friction force imaging using chemically modified tips. Furthermore, the difference in surface properties of these domains made it possible to preferentially deposit ferritin onto the nanoscale

PS ridges. Knowledge of the surface chemical properties of the two domains will provide a means for controlling the adsorption of nanomaterials and biomolecules on PS-*b*-PMMA-derived nanostructured films based on chemical interactions.

Chapter 5 - Bottom-up Fabrication and Characterization of a free-standing PS-*b*-PMMA monolith inside a quartz micropipette

Introduction

This chapter describes the novel fabrication and characterization of a free standing polystyrene-poly(methyl methacrylate) (PS-*b*-PMMA) diblock copolymer nanoporous monolith incorporated at the end of a quartz micropipette. The PMMA domain alignment at the free surface of the monolith was verified by tapping-mode atomic force microscopy (TM-AFM). Ion transport properties of the nanochannels were investigated from conductance measurements of electrolyte-filled UV/acetic acid treated PS-*b*-PMMA monoliths. Based on these results, ion transport inside the channels was modeled to take into account the surface conductivity at low KCl concentrations. Surface mobilities of K^+, Li^+, $(CH_3)_4N^+$ and $(C_4H_9)_4N^+$ cations were determined from the surface charge density over the low salt concentration regime ($<10^{-4}$ M) where the electrical double layer (EDL) induced by the surface negative charges is comparable to the channel radius and therefore excludes anions. Finally, flux of a negatively charged dye through the monolith was measured to assess the permselective properties of the nanochannels.

Free standing nanoporous monoliths have potential uses as stationary phases in separation columns for separation of trace analytes. For separation applications nanoporous membranes have already shown great potential by offering uniform pore sizes and minimal tortuosity compared to conventional separation media based on sol gels and entangled polymers.[177-180] The use of free standing nanoporous films derived from materials such as anodic alumina (AAO),[181, 182] track-etched polymer membrane (TEPM),[183, 184] and block copolymers[78, 80, 99, 159] has been demonstrated to have good separation selectivity for chemical and biological species. This is because these materials possess an array of cylindrical nanopores with high porosity, a narrow pore size distribution and surface functionality.[185, 186] Despite this, anodic alumina and track-etched membranes with their thin and flexible membrane-like structures cannot be adapted as a monolithic structure for stationary phases in separation columns. Completely free standing and thicker monolithic structures are required for separation columns to achieve high separation efficiency. Fabrication of free-standing membranes from block

copolymers[78, 159] and LbL assembly of polymer films[187, 188] has been previously reported but these were first cast on a substrate and then delaminated to produce a free standing membrane.[78, 99, 159] Membranes produced in this manner had nanoscale thicknesses which was ideal for achieving high fluxes. However, the fragility of such membranes prevented their use in a freely suspended state, hence required a secondary porous substrate to support them[78] which may defeat the purpose of a thinner film for high transport rates. Furthermore, additional steps for delaminating from the original substrate were required to transfer the membrane onto a secondary substrate. Free standing monolithic blocks derived from polystyrene-polylactide (PS-PLA) diblock copolymer [92, 189] and polystyrene-polydimethylacrylamide-polylactide (PS-PDMA-PLA) tri block copolymer[93] have been previously fabricated and characterized by Hillmyer *et al.* However, the hydrolysis method employed to degrade the minor PLA fragment does not cross link the nanoporous PS-framework as would if UV irradiation were used for degradation. Hence the PS-framework may not be mechanically stable unless cross-linked by UV irradiation post hydrolysis.

A simple route to a free-standing PS-*b*-PMMA monolith, by directly incorporating the block copolymer inside a quartz micropipette without the need for additional reinforcements to support the free standing membrane, is described. The direct incorporation of the free-standing monolith facilitates its use as in-situ chemical sensors and separation columns without any additional processing steps to integrate them into devices. Polystyrene-*b*-poly (methyl methacrylate) (PS-*b*-PMMA) diblock copolymer is ideal for this purpose because of its controllable domain size, tunability of domain orientation and well characterized surface chemical properties as described in chapter 4. UV irradiation degrades the PMMA domains leaving a cross-linked porous PS framework. This results in a mechanically stable monolith with COO^- groups lining the channel walls.[108] The optically transparent nature of the UV treated PS-*b*-PMMA monolith with their nanoscale cylindrical channels make them ideal for single molecule spectroscopic studies of molecular mass transport. Understanding molecular-level mass transport mechanisms is crucial for the design of separation columns based on block copolymer self-assembly.

5.1 Experimental

5.1.1 Chemicals and Materials

PS-*b*-PMMA (57K PS-b-PMMA: Mn = 39, 800 g/mol for PS and 17,000 g/mol for PMMA, Mw/Mn: 1.06) and polystyrene (PS: Mw = 119,600 g/mol) were purchased from Polymer Source and used as received. Potassium Chloride (Fisher Scientific), Lithium Chloride (Acros Organics), Tetramethyl ammonium Chloride and Tetrabutyl ammonium Chloride (Tokyo Chemical Industry) and Sulforhodamine B (Acros Organics) were used as received. Quartz capillaries (1.15mm I.D, 1.65 mm O.D, length 10cm) were purchased from Sutter Instrument. Solutions used for electrochemical measurements were prepared with water having an 18 MΩ cm or higher resistivity (Barnstead Nanopure System).

5.1.2 Fabrication of PS-b-PMMA Monolith inside a quartz capillary

Quartz capillaries were melted and pulled to produce micropipettes with sealed ends. The micropipettes were then manually polished on a 1500-b GatorGrit sand paper to obtain conically shaped open ended micropipettes of internal diameters between ~50 -100 μm. The micropipettes were then sonicated in soap water, 18 MΩ water and finally in ethanol before treating in a Harrick plasma cleaner for 5 mins. The narrow ends of the plasma treated micropipettes were immediately immersed in a 2% w/w polystyrene (PS) in toluene. The polystyrene-coated micropipettes were then annealed at 190°C for 12 hrs under vacuum. After annealing, the excess PS on the capillary was removed by sonication in toluene to obtain a PS brush layer of ca.7 nm on the inner walls of the capillary. The presence of the PS brush layer was verified by checking the wetting properties of the micropipette by drawing up water into the capillary and measuring the height of water drawn. The narrow end of the PS-coated micropipette was pressed down vertically over a PS-*b*-PMMA film (~50-80 μm thick, 8% w/w PS-*b*-PMMA) cast on a glass slide (1cm x 1cm) and held upright using a metal block (see figure 5.1(a)). This assembly was heated in a Isotemp Model 281A vacuum oven at 230°C for 6 hrs. The micropipettes with the PS-*b*-PMMA monolith were then detached from the PS-*b*-PMMA film and heated again, this time freely suspended, under vacuum at 190°C for 12 hrs. The capillary incorporated PS-*b*-PMMA monolith was exposed to UV irradiation for 3 hrs under an Ar atmosphere and

subsequently etched in glacial acetic acid and left overnight under reduced pressure. The UV/acetic acid etched PS-*b*-PMMA monolith was used for the characterization.

5.1.3 Characterization of capillary incorporated UV/acetic acid etched PS-b-PMMA monoliths

Formation of PS-*b*-PMMA monolith at the narrow end of the micropipette was verified using an inverted Nikon Eclipse TE2000-S optical microscope at 10x magnification. PMMA domain alignment inside the monolith was verified by first casting a PS-*b*-PMMA film over a 25 μm diameter pore drilled into a 1mm thick glass disc under the same conditions used for the fabrication of the monolith inside the quartz capillary. TM-AFM images of the surface of this PS-*b*-PMMA film were obtained in air using a Digital Instruments Multimode AFM with Nanoscope IIIa electronics. TM-AFM probes from Applied Nanostructures (cantilever length, 125 μm; force constant, 40 N/m; resonant frequency, 300 kHz) were used.

The conductance of KCl solution through the micropipette was measured at different KCl concentrations (10^{-1} – 10^{-5} M) before and after incorporating the UV/acetic acid etched PS-*b*-PMMA monolith. This was done in a two-electrode cell, using a CH Instruments model 600B electrochemical analyzer, by scanning the voltage from -0.2 to +0.2 V of the Ag/AgCl working electrode placed inside the micropipette against an Ag/AgCl reference electrode placed in the bulk KCl. The micropipette was filled with the same electrolyte as the bulk solution. The conductance (1/R) was determined from the *I-V* curves for each KCl concentration. The bulk conductivities (κ) of the KCl solutions were measured using a YSI Model 35 conductance meter. The conductance of lithium chloride, Tetramethyl ammonium chloride and Tetrabutyl ammonium chloride solutions, at different salt concentrations (10^{-1} – 10^{-5} M), through the UV/acetic acid etched PS-*b*-PMMA monolith was measured as described above for KCl solution.

Flux measurements were performed by filling the capillary incorporated monolith with an aqueous solution of sulphorhodamine B dye and measuring fluorescence in the receiving solution over a period of 3 days using a generic Fluoromax-2 (ISA instruments J.A Inc). A feed concentration of 100 μM of the dye dissolved in 18 MΩ water, 1mM, 10mM and 100mM KCl was used for the flux experiment.

5.2 Results and Discussion

5.2.1 Fabrication of PS-b-PMMA Monolith

Formation of the PS-*b*-PMMA monolith at the narrow end of a quartz micropipette was verified by optical imaging. Figure 5.1(b) shows a typical optical image of a 50 μm thick PS-*b*-PMMA monolith formed at the end of the micropipette. The monolith is defined by the optically transparent plug at the very end of the micropipette. Upon heating the assembly shown in figure 5.1(a) at 230°C the PS-*b*-PMMA film melts (glass transition temperatures of PMMA and PS are 129 and 106 ^{o}C respectively)[190] and capillary action causes this melt to wick up the micropipette. This generic method has been previously employed to fabricate polymeric nanorods and nanotubes via capillary action of polymer melts into nanoporous alumina templates.[190-192] The amount of PS-*b*-PMMA drawn into the micropipette depended upon the geometry of the micropipette tip. Narrower tips wicked up more PS-*b*-PMMA than did the wider ones. Furthermore, the method used for capillary pulling does not allow control over tip geometry. Therefore, fine control of monolith thickness was not possible and varied widely between ca. 30-120 μm.

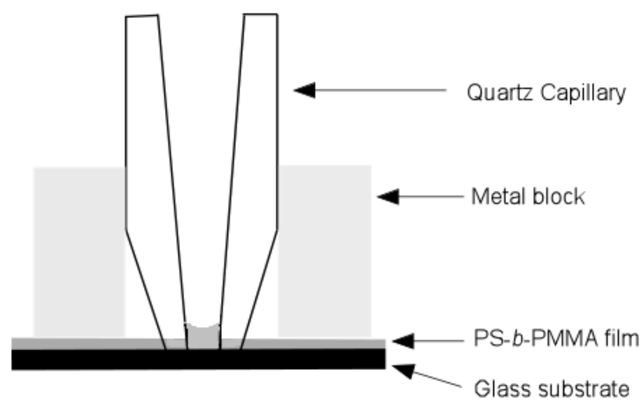

(a)

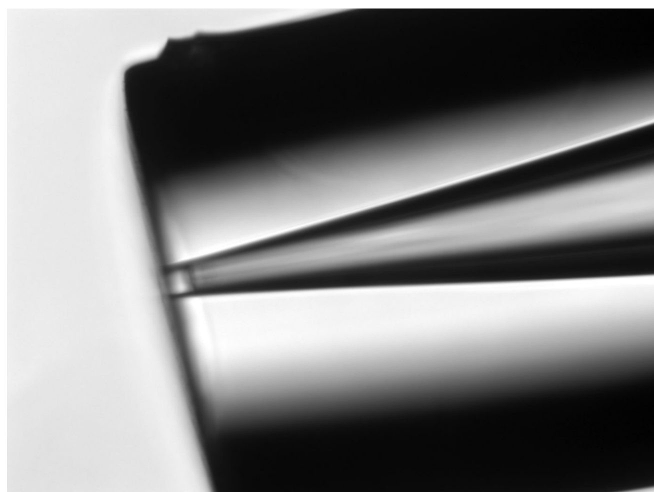

(b)

Figure 5.1 (a) Schematic diagram of a quartz capillary pressed down vertically over a PS-*b*-PMMA film on a glass substrate and heated under vacuum at 230°C. The molten PS-*b*-PMMA wicks up the capillary to form a monolith at the narrow end. (b) Optical image of a 50 μm thick PS-*b*-PMMA monolith formed at the end of a quartz capillary (magnification 10x).

In order to improve PMMA domain alignment, the PS-*b*-PMMA monolith was further heated under vacuum at 190°C for 12 hrs, freely suspended so that both ends of the monolith

were exposed to the vacuum. It is well known that PS-*b*-PMMA, upon annealing under vacuum at high temperature, forms organized arrays of cylindrical PMMA domains within a PS matrix when the volume fraction of PMMA and PS is 0.3 and 0.7 respectively.[110] Furthermore, due to the nearly balanced affinity of the PMMA and PS fragments at the polymer/vacuum interface, as suggested by their similar surface tension values (PS- 31.4 and PMMA 31.2 mN/m)[152] both domains are expected to be exposed at the free ends of the monolith (figure 5.2(a)). This should result in an array of horizontally aligned PMMA domains within the PS matrix. This was verified by AFM imaging of the surface as described in the next section. Incorporating a monolithic PS-*b*-PMMA inside a capillary, so that PMMA domains align horizontally *within* the PS matrix, requires modification of the wetting property of the hydrophilic quartz surface. The PMMA would preferentially wet an unmodified quartz surface since PMMA is more hydrophilic than PS. If this were the case the monolith would detach from the capillary during UV/acetic acid treatment in which the PMMA is degraded. To this end, the wetting property of the quartz surface was reversed by covalently linking a PS homopolymer brush layer to the inner walls of the plasma treated quartz capillary for preferential wetting of the walls by the PS fragment. In this case, PS has a higher affinity for the chemically identical PS-brush layer than would the hydrophilic PMMA fragment. Manipulating interfacial interactions for preferential segregation at the interface of one of the components in diblocks has been often used for controlling domain orientation in thin films.[193-195]The presence of the PS brush layer was verified by measuring the heights of a column of water drawn up by a plasma- treated unmodified cylindrical quartz capillary and a PS layer coated capillary. The results of these measurements are shown in table 5.1. The height of water (h) drawn up a cylindrical capillary is given by:[113]

$$h = \frac{2\gamma\, Cos\theta}{r\rho g} \qquad \text{Eq-1}$$

where γ is the surface tension of water, θ , contact angle between wall and meniscus, r, the radius of capillary, ρ, density of water and g gravity. The water contact angle θ for a plasma treated surface is almost zero because of the introduction of hydrophilic groups during plasma treatment; hence water completely wets such a surface. The water contact angle of a PS-coated capillary (θ_{PS}) was calculated using Eq-2 (derived from Eq-1 assuming the change in radius is negligible

after PS modification (PS layer ~7 nm as determined from ellipsometry of a PS brush layer on a glass substrate) from the heights of water measured for plasma-treated and PS-coated capillaries and θ_{water} for a plasma-treated capillary.

$$Cos\theta_{PS} = \frac{h_{PS\ capillary}}{h_{plasma\ capillary}} Cos\theta_{plasma} \qquad \text{Eq-2}$$

This yielded a value of 84° for the water contact angle between the PS-coated capillary wall and the meniscus. This was in good agreement with the water contact angle measured on a 30-nm PS homopolymer film cast on a silicon substrate, $\theta_{water} = 86^{o}$ (see chapter 4 section 4.2.2.1 Contact Angle Measurements). These results verified the presence of a PS brush layer on the capillary wall. The PS modification of the capillary used for this experiment was done using the same conditions as for the quartz micropipettes.

Table 5.1 Height of water column and calculated water contact angle (θ^{water}) for plasma-treated and PS-coated cylindrical quartz capillaries. Values reported for the height are the average and standard deviation of at least three trials.

	Plasma-treated capillary	PS-coated capillary
Height of water column (cm)	2.58 +/- 0.04	0.27 +/- 0.10
Contact angle (θ_{water})	~0°	(84 +/- 2)^{o}

(Data obtained by Dr. Takashi Ito)

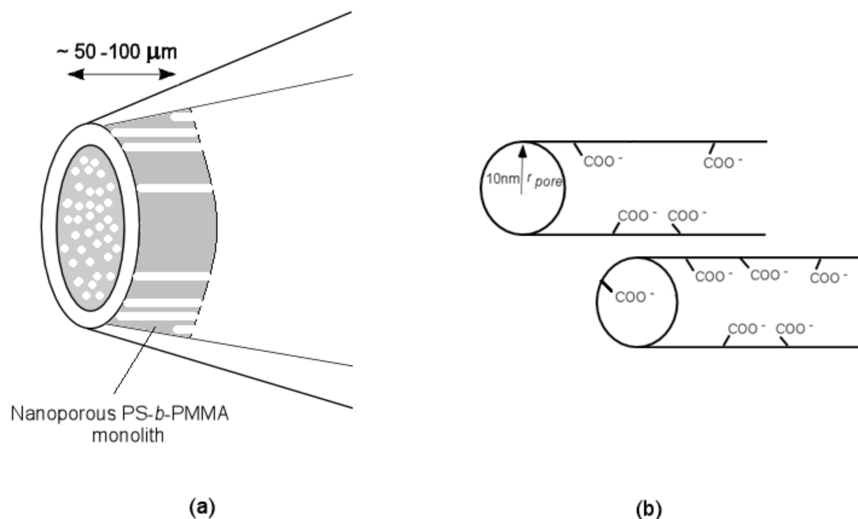

Figure 5.2 (a) Schematic diagram of a UV/acetic acid etched PS-*b*-PMMA nanoporous monolith at the end of a micropipette showing horizontally aligned channels (white regions) within a PS matrix (grey regions) (b) individual nanochannels showing –COO^- groups lining the inner channel wall.

5.2.2 Characterization of UV/acetic acid etched PS-b-PMMA monolith

5.2.2.1 TM-AFM imaging

PMMA domain alignment at the monolith surface was verified by surface imaging of a PS-*b*-PMMA monolith, cast at the end of a 1 mm thick glass disc, using tapping-mode atomic force microscopy (TM-AFM). Figures 5.3 (a) & (b) show typical TM-AFM topography images of the surface of an unetched PS-*b*-PMMA film imaged at two different regions on the monolith. The bright circular dots corresponded to PMMA domains, having an average diameter of ca.19nm, within a PS matrix. The circular dots distributed non-uniformly in both regions of the monolith showing large featureless areas interspersed with a few horizontally oriented domains. However, a uniform distribution of circular dots was seen on a different PS-*b*-PMMA film (cast in the same manner but on a different 1 mm thick glass disc) (see figure 5.3 (d) & (e)). There were a significant number of horizontally oriented PMMA domains as compared to the first film (figure 5.3 (e)). Furthermore, the images shown in figures (d) and (e) were taken closer to the

edge of the film in contact with the disc wall. The presence of the horizontally oriented domains at the surface is not well understood. Although the distribution of the PMMA domains varied between the two films cast in the same manner, these results indicate that the majority of the PMMA domains are aligned vertically at the free surface. Scanning a wider area of the film by SEM imaging will be needed to discuss the distribution of domains across the film surface.

The extent of PMMA domain alignment vertically down the monolith was verified by UV/acetic acid etching of the PMMA domains. Figure 5.3(c) shows the surface of the monolith imaged after the PMMA domains had been etched out. Dark circular dots corresponding to the regions that were occupied by PMMA domains were observed. Presence of the circular dots in the AFM image, even after etching out the PMMA domains, indicates that the domains had extended down to a few hundreds of nanometers from the surface. However, it cannot be concluded from AFM data alone that PMMA nanochannels align themselves in perfectly cylindrical straight channels that span the thickness of the monolith since AFM is confined to surface imaging. TEM imaging will be required to image a longitudinal section of the monolith to verify extent of PMMA domain alignment deep within the PS matrix.

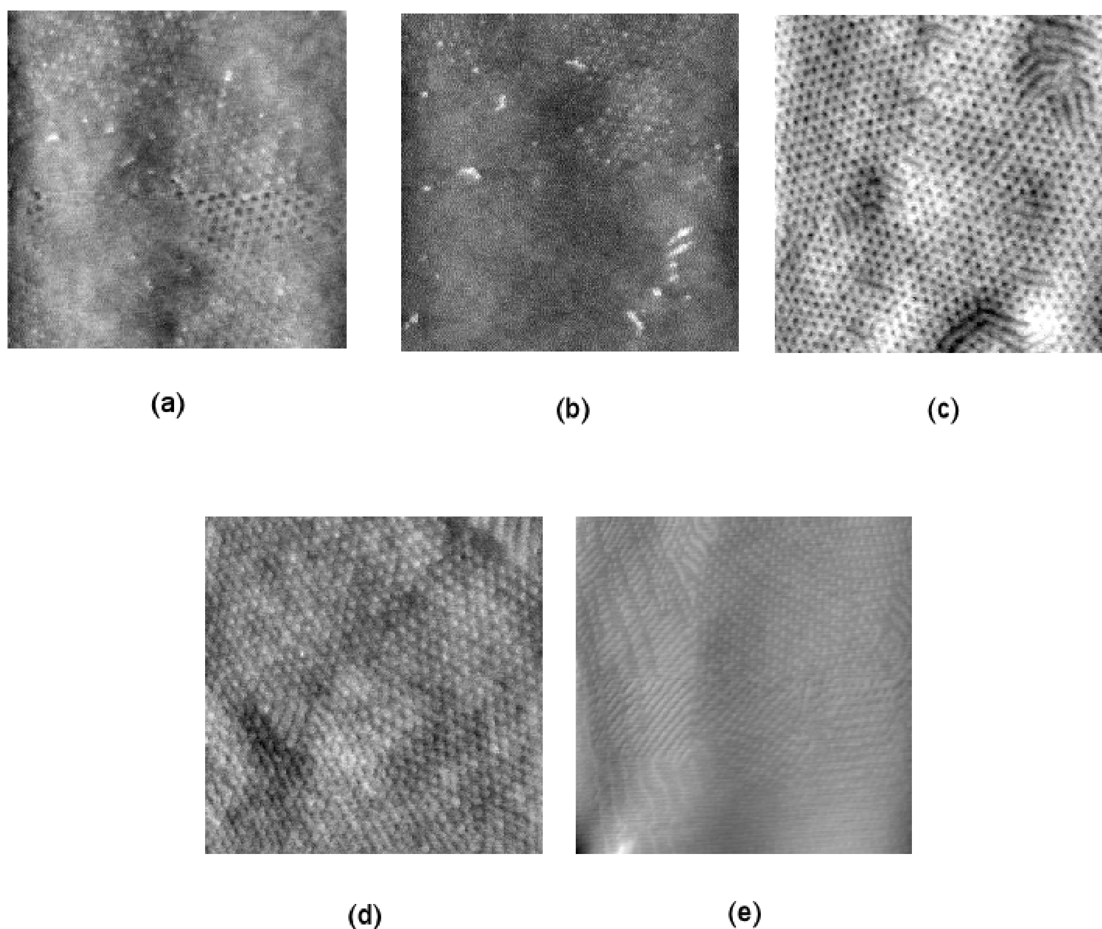

Figure 5.3 Typical TM-AFM topography images in air (1000 x 1000 nm^2, total gray scale range: 30 nm (a)-(d) and 70 nm (e); scan rate: 2 Hz) of the surface of an unetched PS-*b*-PMMA monolith formed at the end of a 25µm channel drilled into a 1mm glass disc, (a) and (b) two different regions on the film (c) after UV/AcOH-etching of the PMMA domains of the film shown in (a) & (b). Figures (d) and (e) represent images taken on an unetched PS-*b*-PMMA monolith cast on a different 1mm glass disc. The PMMA domains are seen as bright circular dots (a),(b),(d) & (e) (elevated) and as pitted regions after PMMA removal in (c).

AFM imaging showed the orientation of the PMMA domains at the surface but could not reveal any defects in the monolith such as micrometer sized holes or nanoscale gaps between the monolith and the capillary wall. Therefore, the UV/acetic acid etched PS-*b*-PMMA monoliths

were further characterized by measuring the conductance of KCl and the flux of sulphorhodamine B dye molecules through the monolith.

5.2.2.2 Conductance measurements

Ion conductance in nanochannels is largely affected by the surface charge on the channel walls. This is mainly because the surface charges induce the build up of a layer of counterions to form an electrical double layer (EDL) that screens the immobile surface charges.[196] The EDL has the greatest influence on ion transport when its thickness is comparable to the channel radius at low salt concentrations. The role of surface charge in governing ionic conductance at low salt concentrations has been previously demonstrated within nanofluidic channels.[197-200] Theoretical models also predicted the influence of surface charge density on nanochannel conductance at low salt concentrations.[199, 201] This was attributed to an excess of mobile counterions accumulating within the channels to neutralize the surface charges. As a result, in this regime, conductance becomes independent of bulk ionic concentration. A plot of conductance inside nanochannels vs. salt concentration in log-log scale showed a conductance plateau at low salt concentrations.[197] It was also shown that at high salt concentrations conductance scaled linearly with bulk ionic concentration and nanochannel geometry.[197-199]

The nanochannels formed after UV/acetic acid etching of the PS-*b*-PMMA monolith possess surface $-COO^-$ groups (figure 5.2(b)). Furthermore, AFM data showed that the nanodomains have uniform diameters of ca. 20 nm. In the absence of large micrometer sized defects, these channels would be expected to show surface-charge-governed ion transport in the low salt concentration regime. Figure 5.4 shows typical cyclic voltammograms (CVs) obtained for a KCl-filled, UV/acetic acid etched PS-*b*-PMMA monolith at bulk KCl concentrations ranging between 10^{-5}-10^{-1} M KCl. The overlapped CVs at the lower KCl concentrations (between 10^{-5}-10^{-4} M KCl) gave nearly similar conductance, as determined from the slopes of the respective CVs, regardless of bulk KCl concentration (figure 5.4 (b)). In contrast, the conductance at KCl concentrations above 10^{-3} M showed an increasing trend with bulk concentration as depicted by the overlapped CVs in figure 5.4 (c). These results are shown in figure 5.5 as a typical conductance plot ($1/R_{total}$ – obtained from the slopes of CVs such as shown in figure 5.4) at different KCl concentrations (in log-log scale) for conductance before and after incorporating the PS-*b*-PMMA nanoporous monolith at the end of a quartz capillary. The

conductance scales linearly with concentration, over all KCl concentrations, for the open capillary (i.e. before incorporating the monolith) whereas it is only linear over a concentration range of 10^{-1}-10^{-3} M KCl for the PS-*b*-PMMA incorporated monolith. At concentrations lower than 10^{-3} M KCl, the conductance within the monolith reached a plateau indicating a concentration independent region. Furthermore, the conductance at 10^{-1} M KCl for the monolith incorporated capillary was two orders of magnitude lower than that for the open capillary. The linear dependence of conductance above 10^{-3} M KCl before and after incorporation of the monolith reflects bulk flow of both K^+ and Cl^- ions. The difference in conductance between the open capillary and monolith is because of the larger resistance of the monolith to ion flow due to its nanoscale channels as compared to the micrometer sized open capillary. The conductance plateau observed at concentrations $<10^{-3}$ M KCl for the monolith is attributed to the surface conductivity of excess K^+ ions accumulating inside the nanochannels. In this regime conductance is largely governed by an interplay between the surface charge density (σ_s) and the nanoscale dimension of the PS-*b*-PMMA channels.

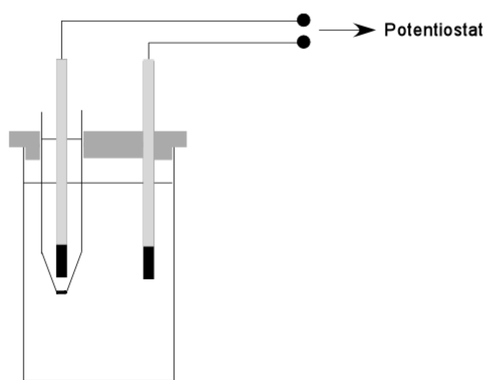

(a)

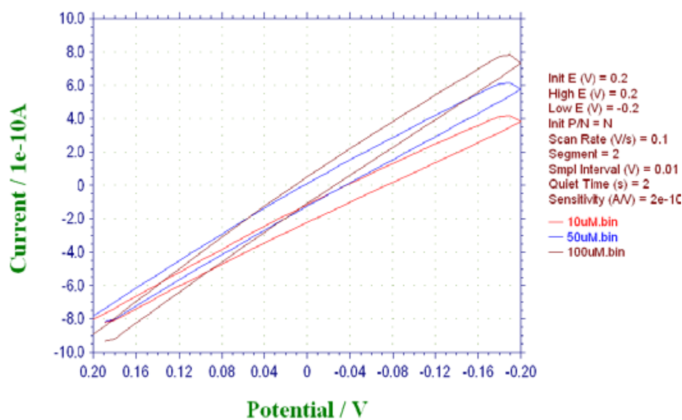

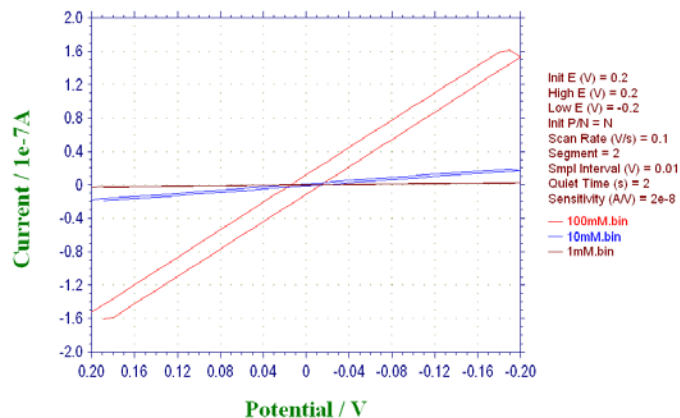

(b) (c)

Figure 5.4 (a) Schematic of the electrochemical cell used for the conductance measurements. (b) & (c) Typical cyclic voltammograms (scan rate 0.1 V/s) obtained for KCl-filled etched PS-*b*-PMMA monolith at different KCl concentrations (a) overlapped CVs for 10^{-5}, 5 x 10^{-5} and 10^{-4} M KCl (b) overlapped CVs for 10^{-3}, 10^{-2} and 10^{-1} M KCl measured against an Ag/AgCl reference electrode.

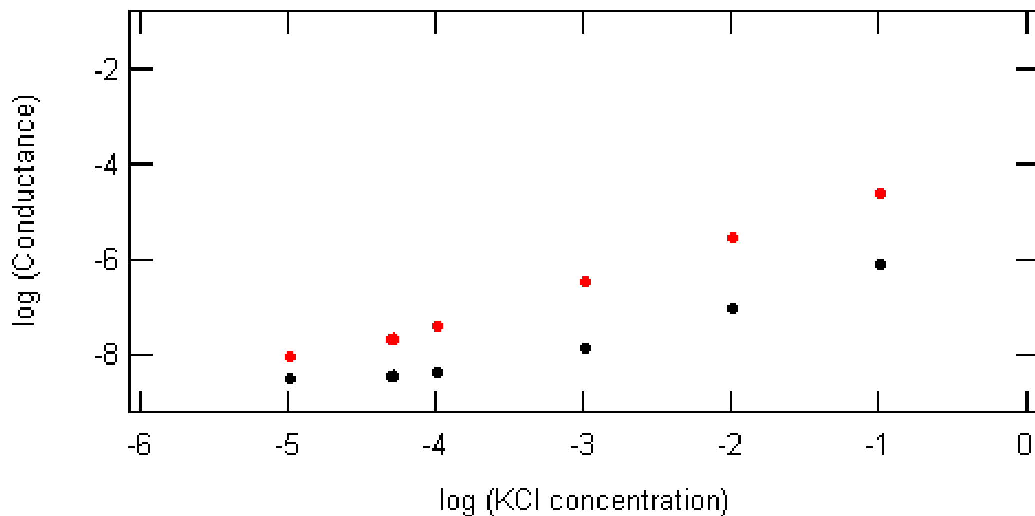

Figure 5.5 Typical log plot of conductance of a KCl filled quartz capillary (tip I.D- 75 µm) as a function of KCl concentration before (red circles) and after (black circles) incorporating the PS-*b*-PMMA monolith.

In the conductance plot shown in figure 5.5 the conductance plateau was reached at 10^{-4} M bulk KCl concentration indicating that conductance is largely governed by the surface charge below 10^{-4} M.[197] Furthermore, it also implies the absence of large *micrometer* sized holes/gaps in the monolith, since if these were present the conductance plateau would never be reached at the salt concentrations used in this work. The presence of the conductance plateau is important in that the surface mobility of cations within the channels can be determined from the surface charge density due to its influence on cation transport in the concentration independent regime. Furthermore, in this regime anions are occluded from the channel since the EDL is comparable to the pore radius, hence current is largely carried by the flow of cations. Drawing on previous work on nanofluidic transport, an ion transport model was used to take into account the surface conductivity at low salt concentrations.

Ion transport model. The total current (I) flowing through a KCl-filled nanoporous PS-*b*-PMMA nanochannel when a voltage is applied across it, is given by:[202]

$$I = \pi r_{pore}^{2} \kappa_{bulk} E + 2\pi r_{pore} \kappa_{s} E \qquad \text{Eq-3}$$

Where r_{pore} is the radius of the nanochannel, κ_{bulk} the bulk KCl conductivity and E electric field (V/cm). The first term on the right hand side is related to the bulk flow of ions and the second term is due to the contribution of the ions in the diffuse layer to the total current. Furthermore, the surface conductivity within the double layer can be expressed as:[202]

$$\kappa_{s} = \frac{\sigma_{s} \lambda^{2} F^{3}}{\varepsilon RT} \sum z_{i}^{3} u_{i} c_{i} \qquad \text{Eq-4}$$

Substitution of Eq-4 into Eq-3 for κ_s and simplification using ($\lambda^2 = \varepsilon RT / z^2 F^2 c$) for a 1:1 (z =1) electrolyte yields for the total current:

$$I = E r_{pore} \left(\pi r_{pore} \kappa_{bulk} + 2\pi \sigma_{s} u_{+} \right) \qquad \text{Eq-5}$$

where σ_s and u_+ are the surface charge density (C/cm^2) and surface mobility of cations (cm^2/Vs) respectively. Since $I/E = 1/R$ and for a single channel with length (l) the total resistance of a single channel is given by:

$$\frac{1}{R_{channel}} = \frac{r_{pore}}{l} \left(\pi r_{pore} \kappa_{bulk} + 2\pi \sigma_{s} u_{+} \right) \qquad \text{Eq-6}$$

The total resistance of the PS-*b*-PMMA monolith with N number of channels, *parallel* to each other (see figure 5.2(a)), is given by:

$$\frac{1}{R_{monolith}} = \frac{N\, r_{pore}}{l}\left(\pi\, r_{pore}\, \kappa_{bulk} + 2\pi\, \sigma_s\, u_+\right) \qquad \text{Eq-7}$$

However, the total measured resistance (R) from the I-V plot is the sum of the resistance ($R_{monolith}$) due to the PS-*b*-PMMA monolith and the resistance ($R_{capillary}$) due to the capillary in *series* with the monolith:

$$R_{Total} = R_{capillary} + R_{monolith} \qquad \text{Eq-8}$$

Substituting Eq-7 into Eq-8 for $R_{monolith}$ yields:

$$R_{Total} - R_{capillary} = \frac{l}{N\left(\pi\, r_{pore}^2\, \kappa_{bulk} + 2\pi\, r_{pore}\, \sigma_s\, u_+\right)} \qquad \text{Eq-9}$$

where σ_s is the surface charge density of COO^- groups. The first term in the denominator corresponds to the bulk conductance and the second term to the surface conductance. For a given KCl concentration Eq-9 assumes the value of the bulk conductivity, κ , to be the same within the nanochannels and in bulk solution. The total conductance through the monolith for all KCl concentrations is therefore the sum of the bulk conductance and the surface conductance [Eq-9]. At high KCl concentrations ($>10^{-3}$ M – for the system under study) surface conductance is negligible, hence total conductance is dominated by the bulk flow of ions, so Eq-9 simplifies to:

$$R_{Total} - R_{capillary} = \frac{l}{\kappa_{bulk}\, \pi\, r_{pore}^2 N} \qquad \text{Eq-10}$$

Equation 10 allows the determination of N, number of channels in the PS-*b*-PMMA monolith, from conductance of the open capillary ($1/R_{capillary}$) and that with the PS-*b*-PMMA monolith ($1/R_{Total}$) at KCl concentrations $>10^{-3}$ M (figure 5.5). The surface mobility of the cation (K^+) can be calculated from the conductance at the plateau region, where surface conductivity dominates ion flow, using Eq-9. The thickness (l) of the channels was estimated from optical images of the

monolith assuming the channels span the monolith thickness. The radius of the channel, r_{pore}, was determined from AFM images in the work reported in chapter 4 section 4.1. The surface charge density (σ_s) of UV/acetic acid etched PS-*b*-PMMA nanopores has been determined from cation exchange experiments done by the Ito group and found to be 1.5 x 10^{-5} C/cm^2.

The transport behavior of various cations through a UV/acetic acid treated PS-*b*-PMMA monolith was investigated in order to probe interactions of different cations with the surface COO^- groups. Figure 5.6 shows a typical conductance plot obtained at different concentrations of KCl, LiCl, tetramethyl ammonium chloride [$(CH_3)_4N^+ Cl^-$)] and tetrabutyl ammonium chloride [$(C_4H_9)_4 N^+ Cl^-$)]. All of the cations showed similar conductance at higher concentrations (> 10^{-3} M) and also at the concentration independent region (between 10^{-4} and 10^{-5} M salt concentration). Typically the conductance over the plateau region decreased in the order $K^+ > Li^+ \sim (CH_3)_4N^+ > (C_4H_9)_4 N^+$. The surface mobilities of the cations were calculated from their conductance plots at the plateau region employing Eq-9. Table 5.2 summarizes the calculated surface mobilities of cations within PS-*b*-PMMA nanochannels. The absolute value of the surface mobility consistently decreased in the order $K^+ > Li^+ \sim (CH_3)_4N^+ > (C_4H_9)_4 N^+$ reflecting the same trend as their bulk mobilities(Table 5.3). However, the surface mobility ratios between K^+, Li^+, $(CH_3)_4N^+$ compared to $(C_4H_9)_4 N^+$ differed largely for different monoliths (Table 5.3). This variation was more pronounced for K^+ ions among the four PS-*b*-PMMA monoliths. Similar trends in surface and bulk mobilities of cations and the wide variation in surface mobility ratios among different monoliths make it difficult to conclude the presence of any interactions of these cations with $-COO^-$ groups on the channel walls.

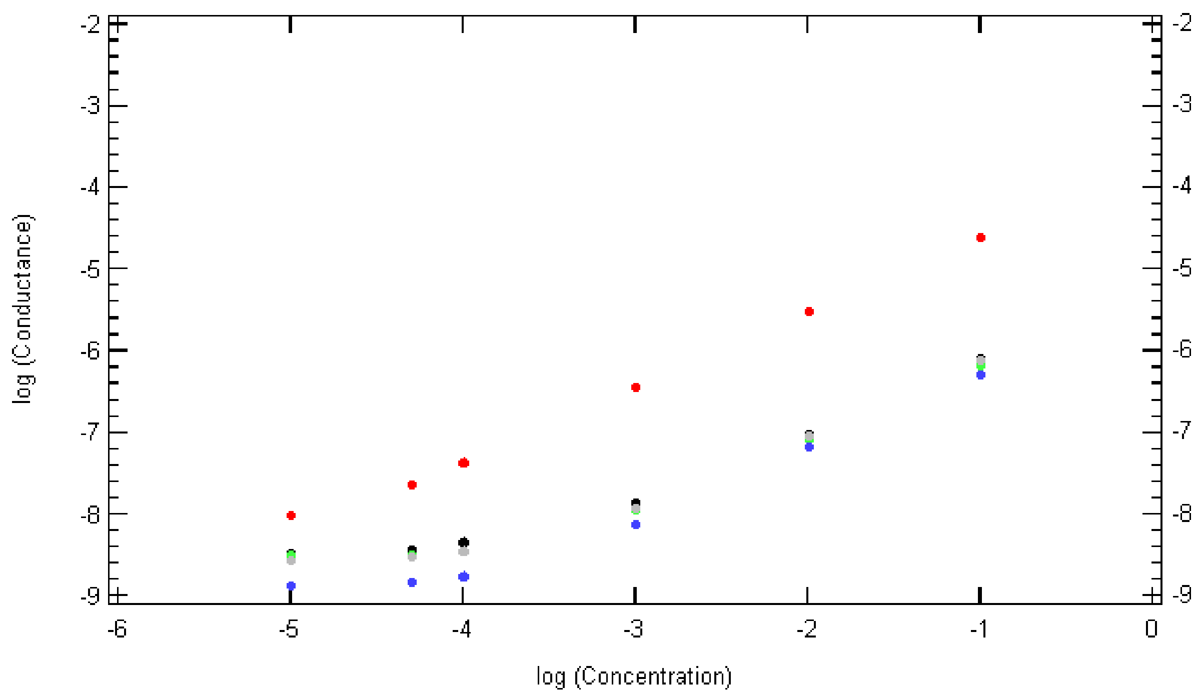

Figure 5.6 Typical log plot of conductance vs. electrolyte concentration of a quartz capillary with a PS-*b*-PMMA monolith. The electrolyte used was KCl (black), LiCl (grey), tetramethyl ammonium chloride (green) and tetrabutyl ammonium chloride (blue). Conductance plot of KCl filled quartz capillary (tip I.D- 75 µm) with no monolith (red).

Table 5.2 Summary of the surface mobilities of cations within different PS-*b*-PMMA monoliths. The surface mobility reported is the average and standard deviation of surface mobilities calculated from the respective conductance plots of the cations at 10^{-5}, 5 x 10^{-5} and 10^{-4} M electrolyte concentration.

	Surface Mobility 10^{-6}(cm^2/Vs)			
	Monolith 1	Monolith 2	Monolith 3	Monolith 4
K^+	2.20 +/- 0.25	0.53 +/- 0.10	3.70 +/- 0.38	2.50 +/- 0.75
Li^+	1.90 +/- 0.33	0.15	3.50 +/- 0.34	0.23 +/- 0.06
$(CH_3)_4N^+$	1.60 +/- 0.17	0.20 +/- 0.07	3.80 +/- 0.13	0.28 +/- 0.08
$(C_4H_9)_4N^+$	0.64 +/- 0.04	0.07 +/- 0.08	1.90 +/- 1.30	0.15 +/- 0.06

Table 5.3 Ratios of surface mobility of a cation to the surface mobility of tetrabutyl ammonium cation for different PS-*b*-PMMA monoliths.

	Surface mobility of cation / Surface mobility of $(C_4H_9)_4N^+$			
	K^+	Li^+	$(CH_3)_4N^+$	$(C_4H_9)_4N^+$
Monolith 1	3.4	3.0	2.5	1.0
Monolith 2	7.6	2.1	2.8	1.0
Monolith 3	1.9	1.8	2.0	1.0
Monolith 4	16.7	1.5	1.9	1.0
	Bulk mobility of cation 10^{-4} (cm^2/Vs)			
	K^+	Li^+	$(CH_3)_4N^+$	$(C_4H_9)_4N^+$
	7.62[a]	4.01[a]	3.79[b]	2.02[c]

Bulk mobilities.[126, 203] a- data obtained from ref [126], b and c – data obtained from ref [203].

5.2.2.3 Flux Measurement

The permselective nature of the UV/acetic acid-treated PS-*b*-PMMA nanochannels was investigated by a more direct method involving the measurement of flux of sulphorhodamine B through the monolith. Flux was measured as increases in the fluorescence intensity of the dye in the receiving cell. Figures 5.7 (a) and (b) show typical transport plots of sulphorhodamine B through a PS-*b*-PMMA monolith measured at different time intervals. The rate of transport of the dye increased very gradually for the dye dissolved in water and 1mM KCl compared to that observed for the dye in 10mM and 100 mM KCl solutions which was significantly higher. This trend was observed for both PS-*b*-PMMA monoliths (figure 5.7 (a) & (b)). Despite the higher rate of transport, typically the final concentration of the dye in the receiving cell after 3 days

reached only ca. 2 nM. These observations can be explained by considering the permselectivity of the nanochannels to the negatively charged dye molecule in pure water and in different salt concentrations. Permselective transport is a phenomenon based on the electrostatic repulsion between a charged molecule and a charged pore wall when the thickness of the electrical double layer (EDL) is comparable to the radius of the pore.[204] This phenomenon has been previously demonstrated for nanoporous systems.[76, 108, 185, 205] The thickness of the EDL (δ) at 25°C for a 1:1 electrolyte such as KCl is given by:[126]

$$\delta = 1/\kappa = \frac{3.0\times10^{-8}}{\sqrt{C}} \qquad \text{Eq-11}$$

where C is the bulk concentration of KCl in mol/L. The characteristic thickness of the EDL is about 10, 3, and 1 nm for a 10^{-3}, 10^{-2} and 0.1 M KCl solution respectively. Thus for PS-*b*-PMMA channels with a 20-nm diameter opening the EDL thickness is comparable to the radius in a 10^{-3} M KCl solution and in water. Therefore, negatively charged sulphorhodamine dye molecules will be occluded from the channel due to electrostatic repulsion between the dye and $–COO^{-}$ groups on the channel wall. At higher KCl concentrations, the negative charges on the wall are effectively screened by K^{+} ions, decreasing the EDL thickness and leaving a largely neutral core. This explains the higher flux observed for the dye in 10mM and 100mM KCl solutions (EDL 3 and 1 nm respectively). A perfectly permselective PS-*b*-PMMA channel, in the absence of any nanoscale holes or gaps, would be expected to completely occlude the dye molecules in water and 1mM KCl solution. However, a considerable flux through the monolith was observed for the dye in water and 1mM KCl for all of the PS-*b*-PMMA monoliths investigated. This indicates the diffusion of dye molecules through pores larger than the standard pore size of 20 nm, probably through nanoscale gaps between the monolith and the capillary. Indeed, shrinking of the nanoporous PS framework due to cross-linking during UV/Ar irradiation has been demonstrated previously.[206]. In a 100-nm gap, filled with 1 mM KCl, the EDL thickness is about 10 nm which effectively shrinks the gap by only 20 nm leaving a considerably neutral cross section. The negative surface charge has no effect on the dye molecules in the neutral region, thus permitting them to enter the channels even in water and 1mM KCl. These observations are consistent with the conductance measurements which showed transition to the conductance plateau at a much

lower bulk KCl concentration indicating the presence of gaps >20 nm in size. Despite this, the transport rates of the dye in water and 1mM KCl were still significantly lower than those in 10mM and 100 mM KCl solutions (see figures 5.7 (a) & (b)). These results imply that only *nanoscale* gaps were present between the capillary wall and the monolith. The presence of micrometer-sized defects/gaps would result in high fluxes of the dye in water and 1mM KCl, comparable to that observed in 10 and 100mM KCl.

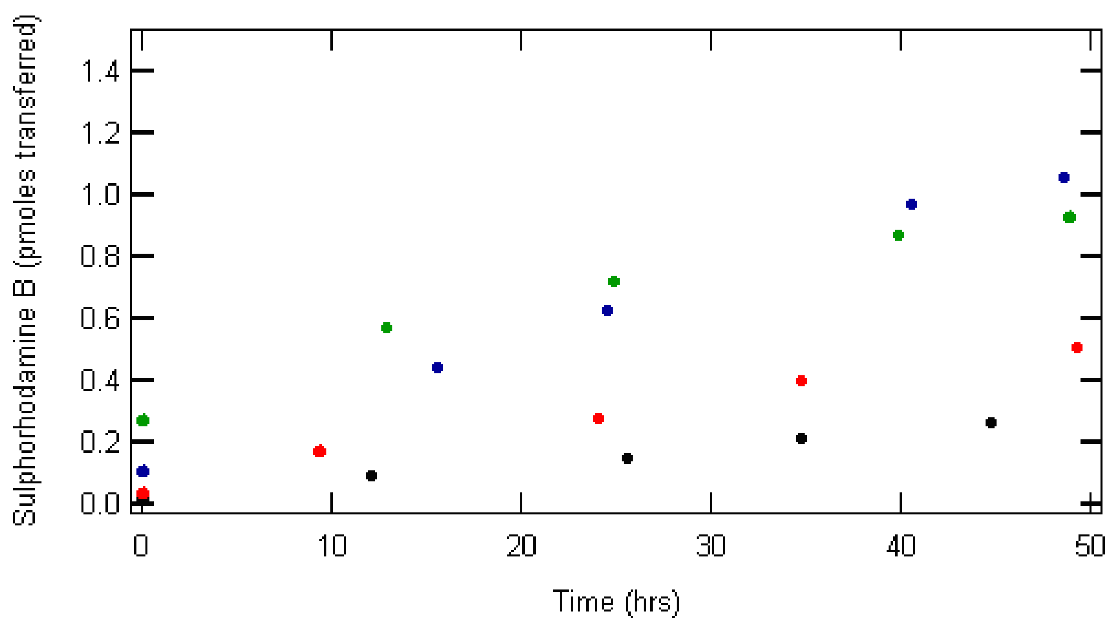

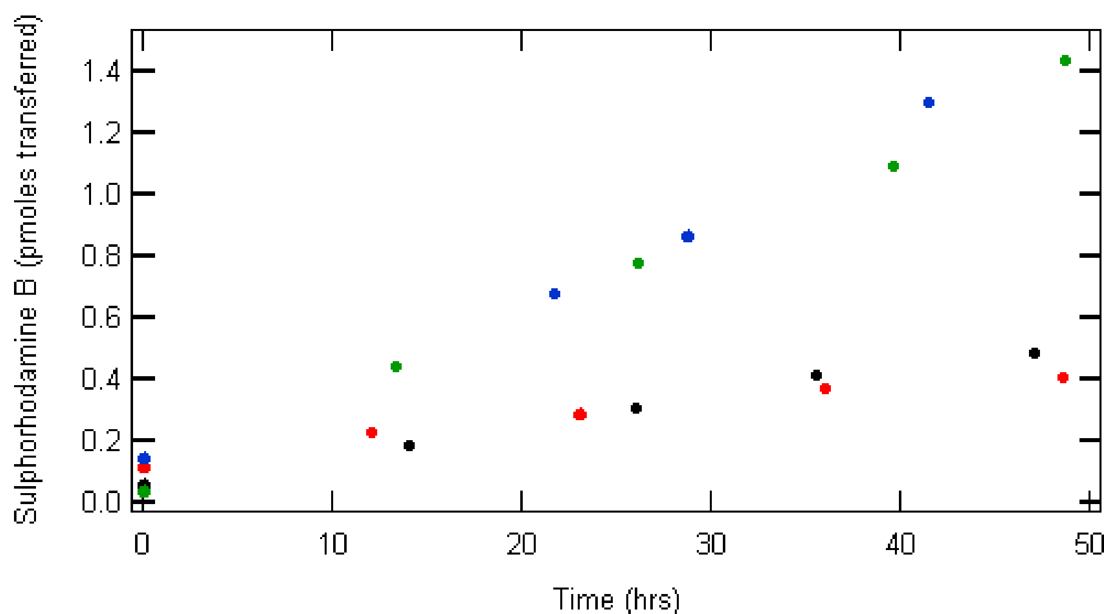

Figure 5.7 Typical transport plots for sulphorhodamine B through a UV/acetic acid etched nanoporous PS-*b*-PMMA monolith as a function of time. The feed solution concentration of the dye was 100 µM dissolved in water (black) 1mM KCl (red) 10mM KCl (blue) and 100mM KCl (green), (a) & (b) represent transport data obtained from two different PS-*b*-PMMA monoliths.

The diffusion coefficient of the sulphorhodamine dye in 10 and 100mM KCl solution was calculated using Fick's first law which states that for a linear diffusion, the flux (J) mol/cm^{2}s of a molecule is proportional to the concentration gradient $\partial C/\partial x$ and diffusion coefficient D given by:[126]

$$-J(x,t) = D\,\frac{\partial C(x,t)}{\partial x} \qquad \text{Eq-12}$$

The flux (J) through the UV/acetic acid etched PS-*b*-PMMA monolith was calculated from the moles of dye transferred (transport plots shown in figure 5.7) to the receiving cell per second per unit active area ($\pi r^2_{pore} \times N$). The number of pores, N, was calculated using Eq-10. The concentration gradient across the monolith was calculated using a feed concentration of 10^{-4} M of the dye, assuming straight channels that spanned the thickness of the monolith (l). Effects due to tortuosity were not considered for the calculation of the diffusion coefficient. The calculated values of the diffusion coefficient (D) of sulphorhodamine B in PS-*b*-PMMA monoliths are summarized in table 5.4. This was found to be within the range reported in the literature (2.0-4.0 x 10^{-6} cm^2/Vs)[207] for the bulk diffusion coefficient of sulphorhodamine B. Typically D was found to be in the range between 2.0 - 6.0 x 10^{-6} cm^2/Vs for the PS-*b*-PMMA monoliths investigated indicating that the surface charge had no influence on the diffusion of dye molecules at high KCl concentrations (i.e 10^{-2} and 10^{-1} M KCl).

Table 5.4 Diffusion Coefficient of sulphorhodamine B dye calculated using Eq-13 and the transport plots shown in figure 5.6 (a) –Monolith 1 and 5.6 (b)-Monolith 2.

	Diffusion Coefficient cm^2/s	
	Monolith 1	**Monolith 2**
Dye in 10 mM KCl	$4.0 \times 10^{-6} \pm 7.6 \times 10^{-7}$	$3.9 \times 10^{-6} \pm 1.0 \times 10^{-6}$
Dye in 100 mM KCl	$3.2 \times 10^{-6} \pm 6.0 \times 10^{-7}$	$4.2 \times 10^{-6} \pm 1.1 \times 10^{-6}$

5.3 Summary and Conclusions

This chapter described the fabrication of a polystyrene- poly (methyl methacrylate) (PS-*b*-PMMA) diblock copolymer monolith at the open end of a quartz micropipette and its characterization using tapping-mode atomic force microscopy (TM-AFM), ionic conductance and flux measurements. The capillary incorporated monolith was shown to have its PMMA domains align vertically at the free surface as revealed by TM-AFM imaging. This implies the horizontal orientation of the PMMA domains parallel to the long axis of the capillary (see figure 5.2 (a)). The presence of circular dots after UV/Ar etching of the PMMA domains suggested that the domain alignment may have extended a few hundred nanometers into the monolith. Measurement of ionic conductance through the nanochannels showed two distinct regions in the conductance plot. At low KCl concentrations, conductance was mainly governed by the surface charge on the nanochannel walls and at high concentration bulk flow of K^+ and Cl^- dominated ion transport. The occurrence of the conductance plateau for the UV/acetic acid etched PS-*b*-PMMA monoliths enabled the determination of surface mobilities of cations from the surface charge density using the ion transport model. Surface mobilities of cations showed a decreasing trend in the order $K^+ > Li^+ \sim (CH_3)_4N^+ > (C_4H_9)_4 N^+$ which was consistent with the trend in their bulk mobilities ($K^+ > Li^+ \sim (CH_3)_4N^+ > (C_4H_9)_4 N^+$). Flux measurements in water and different KCl concentrations reflected the EDL thicknesses and hence the permselective nature of the nanochannels for a negatively charged dye. However, flux measurements indicated the presence of gaps/holes that were probably within nanoscale dimensions and may have occurred during UV irradiation.[206]

Chapter 6 - General Conclusions and Future Direction

The work reported in this dissertation described the fabrication and characterization of submicron scale and nanoscale structures in commercial polymers via the top-down and bottom-up methods, respectively. It was also shown that bottom up self-assembly of polystyrene-poly (methylmethacrylate) (PS-*b*-PMMA) diblock copolymer could be fabricated as thin films on substrates and in a free-standing conformation. To the best of our knowledge, the free standing conformation of (PS-*b*-PMMA) at the end of a quartz capillary has been undertaken for the first time.

In the top-down fabrication, the nonlinear nature of the etching process, for various commercial polymers, was demonstrated. It was also shown that for UV absorbing polymers strong thresholding of the etching process produced structures with high resolution. This technique is well suited for fabrication of arbitrary submicron-scale features in thin commercial polymer films as it does not involve any wet chemical development or photomasks which can compromise the resolution of features. Furthermore, it was concluded that 15 K PMMA, the lowest molecular weight examined, is best suited for use by the multiphoton ablative method. The main limitation of this method however is the throughput since etching involves raster scanning the substrate over the laser beam, hence limited by the speed of the piezo stage.

The orientation of cylindrical PMMA domains in thin films of polystyrene-poly (methylmethacrylate) (PS-*b*-PMMA) diblock co-polymer was manipulated via a combination of film thickness and substrate roughness to align them either vertically or horizontally to the underlying substrate. It was shown that when the thickness of the block copolymer film was higher than the domain periodicity (ca.35 nm) regardless of the type of underlying substrate the PMMA domains showed vertical orientation at the free surface as revealed by AFM imaging. In PS-*b*-PMMA films having thickness close to the domain periodicity, the nanoscale roughness of the substrate induced vertical domain orientation on gold substrates but not on the rough silicon substrates. The PMMA domains oriented parallel to the underlying rough and smooth silicon substrates. The ability to tune the domain orientation via rough substrates and film thickness without the need to chemically neutralize the surface was important for investigating the surface chemical properties of both the PS and PMMA domains in UV/acetic acid treated PS-*b*-PMMA films described in chapter 4 (4.2). Each orientation had its merits for the characterization of the

nanoporous films after UV/acetic acid etching to degrade the minor PMMA component. As demonstrated by the chemical force microscopy experiments which enabled simultaneous characterization of the surface chemical properties of the trenches formed by etched PMMA domains and the PS ridges. This was possible because both domains were exposed to the surface in the horizontal orientation exposing the functional groups in the trenches. The trenches are ca. 1nm deep and accessible by the AFM tip. The use of chemical force microscopy would not have been possible with the vertical orientation of PMMA domains. The chemical characterization of the vertically oriented PMMA domains after UV/AcOH etching was reported in a previous study, by the Ito group, via cyclic voltammetry.[108] The results presented in chapter 4(4.2) indicated that the etched PMMA domains were more hydrophilic than the unetched PS matrix due to the presence of acidic functional groups (-COOH) at a higher density. However, the results could not clarify any distinct difference in chemical properties between the two nanoscale domains. The importance of studying the surface chemical properties of the PS matrix lies in the use of these nanoporous films as templates for nanolithography and as separation membranes. Knowledge of the functional groups present on the PS matrix will prove useful to tailor its surface so that non-specific adsorption or other surface related phenomena can be enhanced or suppressed. The control of surface charge inside the cylindrical pores, via functionalization, has already been shown previously by our group.[76, 79]The work done in chapter 4 (4.1 and 4.2) set the stage for the fabrication of nanoporous PS-*b*-PMMA monolith at the end of a quartz micropipette. The surface-charge governed transport within the nanochannels, as indicated by the conductance plateau, allowed the determination of surface mobilities of cations at low bulk KCl concentration. Fluxes of the sulphorhodamine dye in 10 and 100 mM KCl solutions were shown to be higher than that in 1mM KCl and water. These results suggested partial permselectivity, since a considerable flux of the dye was observed in water-filled monoliths indicating presence of gaps between the monolith and nanochannel wall. However, these gaps could not have been on the micro-scale, since if this were the case the flux in water would have been comparable to that in a KCl filled monolith. Studies on the permselectivity of PS-*b*-PMMA nanochannels will prove important for separation of charged molecules based on electrostatic repulsion.

The free standing nanoporous PS-*b*-PMMA monolith has potential uses as separation columns for affinity based separations of biological and chemical species. The presence of –COO^- functionality lining the inner walls of the cylindrical channels renders it chemically

versatile in that any desired molecular recognition agent such as molecular beacons or antibodies can be linked to the walls. The direct incorporation of the monolith at the end of the capillary makes it possible to employ them as in-situ sensor probes to detect very minute amounts of analytes in clinical samples. However, studies directed towards elucidating the mass transport behavior of charged and neutral species within the nanochannels need to undertaken prior to their use in applications. Elucidation of molecular mass transport, on a single molecule resolution, is crucial for comprehending molecular interactions with the pore walls. Therefore, future work on the free standing PS-*b*-PMMA monoliths can be directed towards employing them as platforms to elucidate molecular mass transport mechanisms via single molecule tracking and fluorescence correlation spectroscopy experiments. These single molecule techniques can resolve diffusional motions inside nanochannels which are usually masked in ensemble averaging techniques. Resolving macroscopic diffusion into distinct diffusion components will enable the design of efficient separation columns based on PS-*b*-PMMA block copolymer self assembly. Free standing PS-*b*-PMMA nanochannels will be ideal for this work because they possess a narrow distribution of pore sizes and well defined channels. However, TEM imaging of a longitudinal section of the monolith will be required to verify the alignment of the channels within the PS matrix. AFM imaging done in this work is limited to surface imaging which only gives an indication of the vertical alignment of PMMA cylinders on the surface. To ensure that channels formed are perfectly straight and span the entire thickness of the monolith, TEM imaging is crucial. Furthermore, SEM imaging will also be required to scan a wider area of the monolith surface which may reveal any defects in the monolith. The gaps/holes in the monoliths reported in this dissertation were shown to be on the nanoscale dimension, which is more promising than if large micron-scale defects were present. Nevertheless, these monoliths still possess important features like tunable pore diameters and render themselves to chemical functionalization. Future studies can focus on native nanochannels (with –COOH groups) to investigate the single molecule behavior of charged and neutral molecules within the nanochannels. Building on this framework, the charge on the channel can be controlled via functionalization or pH to investigate the molecular transport behavior of various chemical and biological species. More elaborate functionalization with DNA hairpin probes or antibodies may also be possible for separation based experiments with the PS-*b*-PMMA nanochannels.

References

(1) Hamley, I. W. In *Developments in Block Copolymer Science and Technology;* Hamley, I. W., Ed.; Developments in Block Copolymer Science and Technology; John Wiley & Sons, Ltd.: England, **2004**; pp 1-361.

(2) Li, M.; Coenjarts, C. A.; Ober, C. K. *Adv. Polym. Sci.* **2005***, 190*, 183.

(3) Wallraff, G. M.; Hinsberg, W. D. *Chem. Rev.* **1999***, 99*, 1801.

(4) Lippert, T.; Dickinson, J. T. *Chem. Rev.* **2003***, 103*, 453.

(5) Wallraff, G. M.; Hinsberg, W. D. *Chem. Rev.* **1999***, 99*, 1801-1822.

(6) Smith, H. I.; Craighead, H. G. *Phys Today* **1990***, 43*, 24-30.

(7) Gibson, J. M. *Phys. Today* **1997***, 50*, 56-61.

(8) Timp, G.; Behringer, R. E.; Tennant, D. M.; Cunningham, J. E.; Prentiss, M.; Berggren, K. K. *Phys. Rev. Lett.* **1992***, 69*, 1636-1639.

(9) Johnson, K. S.; Berggren, K. K.; Black, A.; Black, C. T.; Chu, A. P.; Dekker, N. H.; Ralph, D. C.; Thywissen, J. H.; Younkin, R.; Tinkham, M.; Prentiss, M.; Whitesides, G. M. *Appl. Phys. Lett.* **1996***, 69*, 2773-2775.

(10) Xia, Y.; Rogers, J. A.; Paul, K. E.; Whitesides, G. M. *Chem. Rev.* **1999***, 99*, 1823-1848.

(11) Kim, Y.; Lieber, C. M. *Science* **1992***, 257*, 375-377.

(12) Sohn, L. L.; Willett, R. L. *Appl. Phys. Lett.* **1995***, 67*, 1552-1554.

(13) Xia, Y.; Whitesides, G. M. *Angew. Chem. , Int. Ed.* **1998***, 37*, 550-575.

(14) Chou, S. Y.; Krauss, P. R.; Renstrom, P. J. *Appl. Phys. Lett.* **1995***, 67*, 3114-3116.

(15) Chou, S. Y.; Krauss, P. R.; Renstrom, P. J. *Science* **1996***, 272*, 85-87.

(16) Chou, S. Y.; Krauss, P. R.; Renstrom, P. J. In *In Nanoimprint lithography;* AVS: Atlanta, Georgia (USA), 1996; Vol. 14, pp 4129-4133.

(17) Gates, B. D.; Xu, Q.; Stewart, M.; Ryan, D.; Willson, C. G.; Whitesides, G. M. *Chem. Rev.* **2005***, 105*, 1171-1196.

(18) Pease, R. F. W. In *In Nanolithography and its prospects as a manufacturing technology;* AVS: 1992; Vol. 10, pp 278-285.

(19) Early, K.; Schattenburg, M. L.; Smith, H. I. *Microelectronic Engineering* **1990***, 11*, 317-321.

(20) Simon, G.; Haghiri-Gosnet, A.; Bourneix, J.; Decanini, D.; Chen, Y.; Rousseaux, F.; Launois, H.; Vidal, B. In *In Sub-20 nm x-ray nanolithography using conventional mask technologies on monochromatized synchrotron radiation;* AVS: Dana Point, California (USA), 1997; Vol. 15, pp 2489-2494.

(21) Baldacchini, T.; LaFratta, C. N.; Farrer, R. A.; Teich, M. C.; Saleh, B. E. A.; Naughton, M. J.; Fourkas, J. T. *J. Appl. Phys.* **2004***, 95*, 6072-6076.

(22) Kawata, S.; Sun, H. -.; Tanaka, T.; Takada, K. *Nature* **2001***, 412*, 697.

(23) Li, L.; Fourkas, J. T. *Mater. Today* **2007***, 10*, 30.

(24) Wu, E. S.; Strickler, J. H.; Harrell, W. R.; Webb, W. W. *Proc. SPIE-Int. Soc. Opt. Eng.* **1992***, 1674*, 776.

(25) Zhou, W.; Kuebler, S. M.; Braun, K. L.; Yu, T.; Cammack, J. K.; Ober, C. K.; Perry, J. W.; Marder, S. R. *Science* **2002***, 296*, 1106.

(26) Cumpston, B. H.; Ananthavel, S. P.; Barlow, S.; Dyer, D. L.; Ehrlich, J. E.; Erskine, L. L.; Heikal, A. A.; Kuebler, S. M.; Lee, I. -. S.; McCord-Maughon, D.; Qin, J.; Rockel, H.; Rumi, M.; Wu, X. -.; Marder, S. R.; Perry, J. W. *Nature* **1999**, *398*, 51.
(27) Sun, H.; Matsuo, S.; Misawa, H. *Appl. Phys. Lett.* **1999**, *74*, 786-788.
(28) Maruo, S.; Kawata, S. *Microelectromechanical Systems, Journal of* **1998**, *7*, 411-415.
(29) Sun, H.; Kawakami, T.; Xu, Y.; Ye, J.; Matuso, S.; Misawa, H.; Miwa, M.; Kaneko, R. *Opt. Lett.* **2000**, *25*, 1110-1112.
(30) Aoki, K.; Osteryoung, J. *J. Electroanal. Chem. Interfacial Electrochem.* **1981**, *125*, 315.
(31) Kim, E.; Xia, Y.; Whitesides, G. M. *Nature* **1995**, *376*, 581-584.
(32) Wolfe, D. B.; Ashcom, J. B.; Hwang, J. C.; Schaffer, C. B.; Mazur, E.; Whitesides, G. M. *Adv Mater* **2003**, *15*, 62.
(33) Higgins, D. A.; Everett, T. A.; Xie, A.; Forman, S. M.; Ito, T. *Appl. Phys. Lett.* **2006**, *88*, 184101.
(34) Grzybowski, B. A.; Haag, R.; Bowden, N.; Whitesides, G. M. *Anal. Chem.* **1998**, *70*, 4645.
(35) Kawamura, Y.; Toyoda, K.; Namba, S. *Appl. Phys. Lett.* **1982**, *40*, 374.
(36) Srinivasan, R.; Mayne-Banton, S. *Appl. Phys. Lett.* **1982**, *41*, 576.
(37) Lippert, T.; Dickinson, J. T. *Chem. Rev.* **2003**, *103*, 453-486.
(38) Srinivasan, R.; Braren, B.; Seeger, D. E.; Dreyfus, R. W. *Macromolecules* **1986**, *19*, 916.
(39) Srinivasan, R.; Sutcliffe, E.; Braren, B. *Appl. Phys. Lett.* **1987**, *51*, 1285.
(40) Lippert, T.; Webb, R. L.; Langford, S. C.; Dickinson, S. C. *J. Appl. Phys.* **1999**, *85*, 1838.
(41) Lee, I. -. S.; Wen, X.; Tolbert, W. A.; Dlott, D. D.; Doxtader, M.; Arnold, D. R. *J. Appl. Phys.* **1992**, *72*, 2440.
(42) Kumagai, H.; Midorikawa, K.; Toyoda, K.; Nakamura, S.; Okamoto, T.; Obara, M. *Appl. Phys. Lett.* **1994**, *65*, 1850.
(43) Xie, A.; Ito, T.; Higgins, D. A. *Adv. Funct. Mater.* **2007**, *17*, 1515.
(44) Cheng, J.; Wei, C.; Hsu, K.; Young, T. *Sens. Actuators B* **2004**, *99*, 186-196.
(45) Martynova, L.; Locascio, L. E.; Gaitan, M.; Kramer, G. W.; Christensen, R. G.; MacCrehan, W. A. *Anal. Chem.* **1997**, *69*, 4783.
(46) Whitesides, G.; Mathias, J.; Seto, C. *Science* **1991**, *254*, 1312-1319.
(47) Dubois, L. H.; Nuzzo, R. G. *Annu. Rev. Phys. Chem.* **1992**, *43*, 437-463.
(48) Manne, S.; Gaub, H. E. *Science* **1995**, *270*, 1480-1482.
(49) Yang, H.; Kuperman, A.; Coombs, N.; Mamiche-Afara, S.; Ozin, G. A. *Nature* **1996**, *379*, 703-705.
(50) Kresge, C. T.; Leonowicz, M. E.; Roth, W. J.; Vartuli, J. C.; Beck, J. S. *Nature* **1992**, *359*, 710-712.
(51) Bates, F. S. *Science* **1991**, *251*, 898-905.
(52) Jenekhe, S. A.; Chen, X. L. *Science* **1999**, *283*, 372-375.
(53) Hillmyer, M. In *Nanoporous Materials from Block Copolymer Precursors;* Abetz, V., Ed.; Block Copolymers II; Springer Berlin / Heidelberg: 2005; Vol. 190, pp 137-181.
(54) Li, W. Z.; Xie, S. S.; Qian, L. X.; Chang, B. H.; Zou, B. S.; Zhou, W. Y.; Zhao, R. A.; Wang, G. *Science* **1996**, *274*, 1701-1703.
(55) Aksay, I. A.; Trau, M.; Manne, S.; Honma, I.; Yao, N.; Zhou, L.; Fenter, P.; Eisenberger, P. M.; Gruner, S. M. *Science* **1996**, *273*, 892-898.
(56) You, N.; Kim, M. J.; Jeong, K.; Jeong, S.; Park, Y.; Jeon, J. *J. Nanoscience & Nanotechnology* **2010**, *10*, 3663-3666.
(57) Yokoi, T.; Sato, S.; Ara, Y.; Lu, D.; Kubota, Y.; Tatsumi, T. *Adsorption* **2010**, *16*, 577-586.

(58) Tan, J.; Wang, H.; Yan, X. *Anal. Chem.* **2009**, *81*, 5273-5280.
(59) Zhang, Z.; Dai, S.; Blom, D. A.; Shen, J. *Chem. Mater.* **2002**, *14*, 965-968.
(60) Peng, H.; Lu, Y. *Adv Mater* **2008**, *20*, 797-800.
(61) Lee, J.; Hirao, A.; Nakahama, S. *Macromolecules* **1988**, *21*, 274.
(62) Lee, J.; Hirao, A.; Nakahama, S. *Macromolecules* **1989**, *22*, 2602.
(63) Hedrick, J. L.; Labadie, J.; Russell, T.; Hofer, D.; Wakharker, V. *Polymer* **1993**, *34*, 4717-4726.
(64) Mansky, P.; Chaikin, P. M.; Thomas, E. L. *J. Mater. Sci* **1995**, *30*, 1987.
(65) Mansky, P.; Harrison, C. K.; Chaikin, P. M.; Register, R. A.; Yao, N. *Appl. Phys. Lett.* **1996**, *68*, 2586-2588.
(66) Liu, G.; Ding, J.; Guo, A.; Herfort, M.; Bazett-Jones, D. *Macromolecules* **1997**, *30*, 1851-1853.
(67) Hashimoto, T.; Tsutsumi, K.; Funaki, Y. *Langmuir* **1997**, *13*, 6869-6872.
(68) Hedrick, J. L.; Labadie, J. W.; Volksen, W.; Hilborn, J. G. *Adv. Polym. Sci.* **1999**, *147*, 61-111.
(69) Park, M.; Harrison, C.; Chaikin, P. M.; Register, R. A.; Adamson, D. H. *Science* **1997**, *276*, 1401.
(70) Harrison, C.; Park, M.; Chaikin, P. M.; Register, R. A.; Adamson, D. H. *J. Vac. Sci. Technol. B* **1998**, *16*, 544-552.
(71) Thurn-Albrecht, T.; Steiner, R.; DeRouchey, J.; Stafford, C. M.; Huang, E.; Bal, M.; Tuominen, M.; Hawker, C. J.; Russell, T. P. *Adv Mater* **2000**, *12*, 787-791.
(72) Park, M.; Chaikin, P. M.; Register, R. A.; Adamson, D. H. *Appl. Phys. Lett.* **2001**, *79*, 257-259.
(73) Fasolka, M. J.; Mayes, A. M. *Annu. Rev. Mater. Res* **2001**, *31*, 323-355.
(74) Hillmyer, M. A. *Adv. Polym. Sci.* **2005**, *190*, 137.
(75) Olson, D. A.; Chen, L.; Hillmyer, M. A. *Chem. Mater.* **2008**, *20*, 869.
(76) Li, Y.; Ito, T. *Langmuir* **2008**, *24*, 8959.
(77) Mercier, L.; Pinnavaia, T. J. *Adv Mater* **1997**, *9*, 500-503.
(78) Yang, S. Y.; Ryu, I.; Kim, H. Y.; Kim, J. K.; Jang, S. K.; Russell, T. P. *Adv Mater* **2006**, *18*, 709.
(79) Li, Y.; Ito, T. *Anal. Chem.* **2009**, *81*, 851.
(80) Nuxoll, E. E.; Hillmyer, M. A.; Wang, R.; Leighton, C.; Siegel, R. A. *ACS Appl. Mater. Interfaces* **2009**, *1*, 888.
(81) Zhang, Q.; Xu, T.; Butterfield, D.; Misner, M. J.; Ryu, D. Y.; Emrick, T.; Russell, T. P. *Nano Lett.* **2005**, *5*, 357.
(82) Darling, S. B.; Yufa, N. A.; Cisse, A. L.; Bader, S. D.; Sibener, S. J. *Adv Mater* **2005**, *17*, 2446.
(83) Darling, S. B. *Surf. Sci.* **2007**, *601*, 2555.
(84) Mansky, P.; Russell, T. P.; Hawker, C. J.; Pitsikalis, M.; Mays, J. *Macromolecules* **1997**, *30*, 6810-6813.
(85) Niemz, A.; Bandyopadhyay, K.; Tan, E.; Cha, K.; Baker, S. *Langmuir* **2006**, *22*, 11092-11096.
(86) Mansky, P.; Liu, Y.; Huang, E.; Russell, T. P.; Hawker, C. *Science* **1997**, *275*, 1458-1460.
(87) Guarini, K. W.; Black, C. T.; Milkove, K. R.; Sandstrom, R. L. *J. Vac. Sci. Technol. B* **2001**, *19*, 2784-2788.

(88) Xuan, Y.; Peng, J.; Cui, L.; Wang, H.; Li, B.; Han, Y. *Macromolecules* **2004***, 37*, 7301-7307.
(89) Jeong, U.; Ryu, D. Y.; Kho, D. H.; Kim, J. K.; Goldbach, J. T.; Kim, D. H. e. a. *Adv Mater* **2004***, 16*, 533-536.
(90) Sivaniah, E.; Hayashi, Y.; Lino, M.; Hashimoto, T.; Fukunaga, K. *Macromolecules* **2003***, 36*, 5894-5896.
(91) Thurn-Albrecht, T.; DeRouchey, J.; Russell, T. P.; Jaeger, H. M. *Macromolecules* **2000***, 33*, 3250-3253.
(92) Zalusky, A. S.; Olayo-Valles, R.; Wolf, J. H.; Hillmyer, M. A. *J. Am. Chem. Soc.* **2002***, 124*, 12761.
(93) Rzayev, J.; Hillmyer, M. A. *J. Am. Chem. Soc.* **2005***, 127*, 13373.
(94) Bailey, T. S.; Rzayev, J.; Hillmyer, M. A. *Macromolecules* **2006***, 39*, 8772.
(95) Mao, H.; Hillmyer, M. A. *Macromolecules* **2005***, 38*, 4038-4039.
(96) Uehara, H.; Yoshida, T.; Kakiage, M.; Yamanobe, T.; Komoto, T.; Nomura, K.; Nakajima, K.; Matsuda, M. *Macromolecules* **2006***, 39*, 3971-3974.
(97) Thurn-Albrecht, T.; Schotter, J.; Kastle, G. A.; Emley, N.; Shibauchi, T.; Krusin-Elbaum, L.; Guarini, K.; Black, C. T.; Tuominen, M. T.; Russell, T. P. *Science* **2000***, 290*, 2126.
(98) Zhang, Q.; Gupta, S.; Emrick, T.; Russell, T. P. *J. Am. Chem. Soc.* **2006***, 128*, 3898.
(99) Yang, S. Y.; Park, J.; Yoon, J.; Ree, M.; Jang, S. K.; Kim, J. K. *Adv. Funct. Mater.* **2008***, 18*, 1371.
(100) Jeong, U.; Ryu, D. Y.; Kim, J. K.; Kim, D. H.; Wu, X.; Russell, T. P. *Macromolecules* **2003***, 36*, 10126-10129.
(101) Kim, H. -.; Jia, X.; Stafford, C. M.; Kim, D. H.; McCarthy, T. J.; Tuominen, M. e. a. *Adv Mater* **2001***, 13*, 795-797.
(102) Xu, T.; Kim, H. -.; DeRouchey, J.; Seney, C.; Levesque, C.; Martin, P.; Stafford, C. M.; Russell, T. P. *Polymer* **2001***, 42*, 9091-9095.
(103) Guarini, K. W.; Black, C. T.; Yeung, S. H. I. *Adv Mater* **2002***, 14*, 1290-1294.
(104) Jeong, U.; Kim, H. -.; Rodriguez, R. L.; Tsai, I. Y.; Stafford, C. M.; Kim, J. K.; Hawker, C. J.; Russell, T. P. *Adv Mater* **2002***, 14*, 274-276.
(105) Xu, T.; Stevens, J.; Villa, J. A.; Goldbach, J. T.; Guarini, K. W.; Black, C. T.; Hawker, C. J.; Russell, T. P. *Adv. Funct. Mater.* **2003***, 13*, 698-702.
(106) Asakawa, K.; Hiraoka, T. *Jpn. J. Appl. Phys* **2002***, 41*, 6112.
(107) Ton-That, C.; Teare, D. O. H.; Bradley, R. H. *Chem. Mater.* **2000***, 12*, 2106.
(108) Li, Y.; Maire, H. C.; Ito, T. *Langmuir* **2007***, 23*, 12771.
(109) Maire, H. C.; Ibrahim, S.; Li, Y.; Ito, T. *Polymer* **2009***, 50*, 2273.
(110) Thurn-Albrecht, T.; Steiner, R.; DeRouchey, J.; Stafford, C. M.; Huang, E.; Bal, M.; Tuominen, M.; Hawker, C. J.; Russell, T. P. *Adv Mater* **2000***, 12*, 787.
(111) Bard, A. J.; Faulkner, L. R. In *Electrochemical Methods, Fundamentals and Applications;* 2001; Vol. null, pp null.
(112) Jeoung, E.; Galow, T. H.; Schotter, J.; Bal, M.; Ursache, A.; Tuominen, M. T.; Stafford, C. M.; Russell, T. P.; Rotello, V. M. *Langmuir* **2001***, 17*, 6396.
(113) Hunter, R. J., Ed.; In *Foundations of Colloid Science;* Oxford University Press: New York, 2002; , pp 1-787.
(114) Ferguson, G. S.; Whitesides, G. M. In *Modern Approaches to Wettability: Theory and Applications;* Shoder,M.;Loeb,G.;Eds.; Plenum: New York, 1991; , pp 143-176.
(115) De Gennes, P. G. *Rev. Mod. Phys.* **1985***, 57*, 827-863.

(116) Heinz, W. F.; Hoh, J. H. *trends in biotechnology* **1999**, *17*, 143-150.
(117) Martin, Y.; Williams, C. C.; Wicramasinghe, H. K. *J. Appl. Phys.* **1987**, *61*, 4723-4729.
(118) Burnham, N. A.; Colton, R. J. *J. Vac. Sci. Technol. A. Vac. Surf. Films* **1989**.
(119) Moiseev, Y. N. e. a. *Zh. Tekh. Fiz* **1990**, *60*, 141-148.
(120) Ito, T.; Grabowska, I.; Ibrahim, S. *Trends Anal. Chem* **2010**, *29*, 225-233.
(121) Hartmann, U. In *An Elementary Introduction to Atomic Force Microscopy and Related Methods;* Saarbrucken, Germany, 1997; , pp 1-57.
(122) Vancso, G. J.; Hillborg, H.; Schonherr, H. *Adv. Polym. Sci.* **2005**, *182*, 55.
(123) Israelachvili, J. In *Intermolecular and Surface Forces;* 1992; Vol. null, pp null.
(124) van, d. V.; Hadziioannou, G. *Langmuir* **1997**, *13*, 4357-4368.
(125) Sinniah, S. K.; Steel, A. B.; Miller, C. J.; Reutt-Robey, J. *J. Am. Chem. Soc.* **1996**, *118*, 8925.
(126) Bard, A. J.; Faulkner, L. R. In *Electrochemical Methods - Fundamentals and Applications;* Bard, A. J., Faulkner, L. R., Eds.; Electrochemical Methods - Fundamentals and Applications; Wiley Interscience: New Jersey, 2001; , pp 814.
(127) Sassolas, A.; Leca-Bouvier, B. D.; Blum, L. J. *Chem. Rev.* **2008**, *108*, 109-139.
(128) Higgins, D. A. **2009**.
(129) McDonald, J. C.; Whitesides, G. M. *Acc. Chem. Res.* **2002**, *35*, 491.
(130) Haske, W.; Chen, V. W.; Hales, J. M.; Dong, W.; Barlow, S.; Marder, S.; Perry, J. W. *Opt. Express* **2007**, *15*, 3426.
(131) Takada, K.; Sun, H. -.; Kawata, S. *Appl. Phys. Lett.* **2005**, *86*, 1.
(132) Juodkazis, S.; Mizeikis, V.; Seet, K. K.; Miwa, M.; Misawa, H. *Nanotechnology* **2005**, *16*, 846.
(133) Luther, B. J.; Springer, G. H.; Higgins, D. A. *Chem. Mater.* **2001**, *13*, 2281.
(134) Bohn, P. W.; Taylor, J. W.; Guckel, H. *Anal. Chem.* **1981**, *53*, 1082.
(135) Thurn-Albrecht, T.; Steiner, R.; DeRouchey, J.; Stafford, C. M.; Huang, E.; Bal, M.; Tuominen, M.; Hawker, C. J.; Russell, T. P. *Adv Mater* **2000**, *12*, 787.
(136) Kumar, A.; Abbott, N. L.; Kim, E.; Biebuyck, H. A.; Whitesides, G. M. *Acc. Chem. Res.* **1995**, *28*, 219.
(137) Love, J. C.; Estroff, L. A.; Kriebel, J. K.; Nuzzo, R. G.; Whitesides, G. M. *Chem. Rev.* **2005**, *105*, 1103.
(138) Han, J.; Craighead, H. G. *Science* **2000**, *288*, 1026.
(139) Mansky, P.; Russell, T. P.; Hawker, C. J.; Pitsikalis, M.; Mays, J. *Macromolecules* **1997**, *30*, 6810.
(140) Huang, E.; Russell, T. P.; Harrison, C.; Chaikin, P. M.; Register, R. A.; Hawker, C. J. e. a. *Macromolecules* **1998**, *31*, 7641-7650.
(141) Xu, T.; Kim, H. -.; DeRouchey, J.; Seney, C.; Levesque, C.; Martin, P. e. a. *Polymer* **2001**, *42*, 9091-9095.
(142) Fasolka, M. J.; Banerjee, P.; Mayes, A. M.; Pickett, G.; Balazs, A. C. *Macromolecules* **2000**, *33*, 5702-5712.
(143) Sivaniah, E.; Hayashi, Y.; Matsubara, S.; Kiyono, S.; Hashimoto, T.; Fukunaga, K. e. a. *Macromolecules* **2005**, *38*, 1837-1849.
(144) Sivaniah, E.; Matsubara, S.; Zhao, Y.; Hashimoto, T.; Fukunaga, K. K.,E.J. et al *Macromolecules* **2008**, *41*, 2584-2592.
(145) Podariu, I.; Chakrabarti, A. *J. Chem. Phys* **2000**, *113*, 6423-6428.
(146) Tsori, Y.; Andelman, D. *Macromolecules* **2003**, *36*, 8560-8566.

(147) Tsori, Y.; Sivaniah, E.; Andelman, D.; Hashimoto, T. *Macromolecules* **2005**, *38*, 7193-7196.
(148) Tomita, N.; Adachi, S. *J. Electrochem. Soc* **2002**, *149*, G245-G250.
(149) Ito, T.; Forman, S. M.; Cao, C.; Li, F.; Eddy, J. C. R.; Mastro, M. A. e. a. *Langmuir* **2008**, *24*, 6630-6635.
(150) Ron, H.; Matlis, S.; Rubinstein, I. *Langmuir* **1998**, *14*, 1116-1121.
(151) Williams, R.; Goodman, A. M. *Appl. Phys. Lett.* **1974**, *25*, 531-532.
(152) Wu, S. I., Ed.; In *Polymer Handbook;* Brandrup, J., Immergut, E. H., Grulke, E. A., Abe, A. and Bloch, D. R., Eds.; John Wiley & Sons: New York, 1999; Vol. 4th ed., pp 521-541.
(153) Gong, Y.; Joo, W.; Kim, Y.; Kim, J. K. *Chem. Mater.* **2008**, *20*, 1203-1205.
(154) Feldman, K.; Tervoort, T.,PS.; Spencer, N. D. *Langmuir* **1998**, *14*, 372-378.
(155) Lopes, W. A. *Phys. Rev. E* **2002**, *65*, 031606.
(156) Kim, H. -.; Russell, T. P. *J. Polym. Sci. B* **2001**, *39*, 663.
(157) Ulman, A. *Chem. Rev.* **1996**, *96*, 1533-1554.
(158) Welander, A. M.; Kang, H.; Stuen, K.,O.; Solak, H. H.,; Muller, M.; de Pablo, J. J. e. a. *Macromolecules* **2008**, *41*, 2759-2761.
(159) Uehara, H.; Kakiage, M.; Sekiya, M.; Sakuma, D.; Yamanobe, T.; Takano, N.; Barraud, A.; Meurville, E.; Ryser, P. *ACS Nano* **2009**, *3*, 924.
(160) Ryu, J. -.; Park, S.; Kim, B.; Klalkherd, A.; Russell, T. P.; Thayumanavan, S. *J. Am. Chem. Soc.* **2009**, *131*, 9870.
(161) Vezenov, D. V.; Noy, A.; Rozsnyai, L. F.; Lieber, C. M. *J. Am. Chem. Soc.* **1997**, *119*, 2006.
(162) Vezenov, D. V.; Noy, A.; Lieber, C. M.; Noy, A. In *Handbook of Molecular Force Spectroscopy;* 2007; Vol. null, pp 123.
(163) Schonherr, H.; van Os, M. T.; Hruska, Z.; Kurdi, J.; Forch, R.; Arefi-Khonsari, F.; Knoll, W.; Vancso, G. J. *Chem. Commun.* **2000**, *null*, 1303.
(164) Schonherr, H.; Hruska, Z.; Vancso, G. J. *Macromolecules* **2000**, *33*, 4532.
(165) Wang, B.; Chen, L.; Abdulali-Kanji, Z.; Horton, J. H.; Oleschuk, R. D. *Langmuir* **2003**, *19*, 9792.
(166) Frisbie, C. D.; Rozsnyai, L. F.; Noy, A.; Wrighton, M. S.; Lieber, C. M. *Science* **1994**, *265*, 2071.
(167) Werts, M. P. L.; van, d. V.; Grayer, V.; Esselink, E.; Tsitsilianis, C.; Hadziioannou, G. *Adv Mater* **1998**, *10*, 452.
(168) Ton-That, C.; Campbell, P. A.; Bradley, R. H. *Langmuir* **2000**, *16*, 5054.
(169) Ito, T.; Forman, S. M.; Cao, C.; Li, F.; Eddy, C. R.; Mastro, M. A.; Holm, R. T.; Henry, R. L.; Hohn, K.; Edgar, J. H. *Langmuir* **2008**, *24*, 6630.
(170) Holmes-Farley, S.; Bain, C. D.; Whitesides, G. M. *Langmuir* **1988**, *4*, 921.
(171) Speight, J. G. In *Lange's Handbook of Chemistry;* 2005; Vol. null, pp null.
(172) Asakura, S.; Hozumi, A.; Fuwa, A. *J. Vac. Sci. Technol. A* **2005**, *23*, 1137.
(173) Clear, S. C.; Nealey, P. F. *J. Colloid Interface Sci.* **1999**, *213*, 238.
(174) Thiel, E. C. *Annu. Rev. Biochem.* **1987**, *56*, 289.
(175) Kumar, N.; Hahm, J. -. *Langmuir* **2005**, *21*, 6652.
(176) Kumar, N.; Parajuli, O.; Gupta, A.; Hahm, J. -. *Langmuir* **2008**, *24*, 2688.
(177) Irvine, G. B. *Anal. Chim. Acta* **1997**, *352*, 387-397.
(178) Kleparnik, K.; Bocek, P. *Chem. Rev.* **2007**, *107*, 5279-5317.
(179) Righetti, P. G.; Verzola, B. *Electrophoresis* **2001**, *22*, 2359-2374.

(180) Walcarius, A.; Mandler, D.; Cox, J. A.; Collinson, M.; Lev, O. *J. Mater. Chem.* **2005**, *15*, 3663-3689.
(181) Lee, S. B.; Mitchell, D. T.; Trofin, L.; Nevanen, T. K.; Soderlund, H.; Martin, C. R. *Science* **2002**, *296*, 2198-2200.
(182) Iguchi, N.; Iida, K.; Sakamoto, T.; Baba, M.; Kawaura, H. *Appl. Phys. Lett.* **2003**, *83*, 4438-4440.
(183) Jirage, K. B.; Hulteen, J. C.; Martin, C. R. *Science* **1997**, *278*, 655-658.
(184) Kohli, P.; Harrell, C. C.; Cao, Z.; Gasparac; Tan, W.; Martin, C. R. *science* **2004**, *305*, 984-986.
(185) Baker, L. A.; Jin, P.; Martin, C. R. *Critical Reviews in Solid State and Materials Sciences* **2005**, *30*, 183-205.
(186) Ulbricht, M. *Polymer* **2006**, *47*, 2217-2262.
(187) Zimnitsky, D.; Shevchenko, V. V.; Tsukruk, V. V. *Langmuir* **2008**, *24*, 5996-6006.
(188) Buck, M. E.; Lynn, D. M. *Langmuir* **2010**, null-null.
(189) Zalusky, A. S.; Olayo-Valles, R.; Taylor, C. J.; Hillmyer, M. A. *J. Am. Chem. Soc.* **2001**, *123*, 1519-1520.
(190) Kriha, O.; Zhao, L.; Pippel, E.; Gösele, U.; Wehrspohn, R.; Wendorff, J.; Steinhart, M.; Greiner, A. *Advanced Functional Materials* **2007**, *17*, 1327-1332.
(191) Xiang, H.; Shin, K.; Kim, T.; Moon, S. I.; McCarthy, T. J.; Russell, T. P. *Macromolecules* **2004**, *37*, 5660-5664.
(192) Zhang, M.; Dobriyal, P.; Chen, J.; Russell, T. P.; Olmo, J.; Merry, A. *Nano Letters* **2006**, *6*, 1075-1079.
(193) Jeong, U.; Ryu, D.; Kho, D.; Kim, J.; Goldbach, J.; Kim, D.; Russell, T. *Adv Mater* **2004**, *16*, 533-536.
(194) Huang, E.; Russell, T. P.; Harrison, C.; Chaikin, P. M.; Register, R. A.; Hawker, C. J.; Mays, J. *Macromolecules* **1998**, *31*, 7641-7650.
(195) Mansky, P.; Russell, T. P.; Hawker, C. J.; Pitsikalis, M.; Mays, J. *Macromolecules* **1997**, *30*, 6810-6813.
(196) Israelachvili, J., Ed.; In *Intermolecular and surface forces;* Academic Press: London, 2003; .
(197) Stein, D.; Kruithof, M.; Dekker, C. *Phys. Rev. Lett.* **2004**, *93*, 035901-1-035901-4.
(198) Karnik, R.; Castelino, K.; Fan, R.; Yang, P.; Majumdar, A. *Nano Letters* **2005**, *5*, 1638-1642.
(199) Schoch, R. B.; Renaud, P. *Appl. Phys. Lett.* **2005**, *86*, 253111-1-253111-3.
(200) Daiguji, H.; Yang, P.; Majumdar, A. *Nano Letters* **2004**, *4*, 137-142.
(201) Schoch, R. B.; Han, J.; Renaud, P. *Rev. Mod. Phys.* **2008**, *80*, 839-883.
(202) Newman, J.; Thomas-Alyea, K. E. In *Electrochemical Systems;* Jonh Newman, Karen E. Thomas-Alyea, Eds.; Electrochemical Systems; Wiley Interscience: New Jersey, 2004; Vol. 3, pp 635.
(203) Fu, S.; Lucy, C. A. *Anal. Chem.* **1998**, *70*, 173-181.
(204) Wei, C.; Bard, A. J. *Anal. Chem.* **1997**, *69*, 4627-4633.
(205) Martin, C. R.; Nishizawa, M.; Jirage, K.; Kang, M. *The Journal of Physical Chemistry B* **2001**, *105*, 1925-1934.
(206) Jeong, U.; Ryu, D.; Kim, J.; Kim, D.; Russell, T.; Hawker, C. *Adv Mater* **2003**, *15*, 1247-1250.
(207) Fang, X.; Xuan, Y.; Li, Q. *Appl. Phys. Lett* **2009**, *95*, 203108-3.